

POLITECNICO DI MILANO

FACOLTÀ DI INGEGNERIA DEI SISTEMI

Tesi di Laurea Magistrale in Ingegneria Biomedica



**Measurement and time-frequency analysis of
intra-operative head restraint stress in awake
neurosurgical procedures**

Relatore:

Ing. Elena DE MOMI

Correlatori:

Ing. Danilo DE LORENZO

Prof. Lorenzo BELLO

Tesi di Laurea di:

Lorenzo CONTI

Matricola 751279

Alla mia famiglia...

...a Maria Giovanna

“If the facts don't fit the theory, change the facts”

Albert Einstein

Acknowledgments

Vorrei ringraziare il *Prof. Giancarlo Ferrigno* e l'*Ing. Elena De Momi* per avermi dato l'opportunità di svolgere questo lavoro e per la costante opera di supervisione.

Ringrazio l'*Ing. Danilo De Lorenzo* per il tempo dedicatomi e per i preziosi suggerimenti durante lo svolgimento dell'attività.

Grazie a tutto lo *staff del NearLab* e a *Marta* per l'accoglienza, il supporto e la compagnia durante questo anno e mezzo di permanenza. Un ringraziamento particolare a *Danilo* ed *Elisa* per l'aiuto durante la fase sperimentale.

Grazie di cuore alla *mia famiglia* per avermi sostenuto e incoraggiato durante il tutto il periodo universitario.

Grazie infine a *Maria Giovanna* per l'infinita pazienza e la straordinaria capacità di comprensione.

Index

Acknowledgments	1
Index	2
Abstract.....	5
Sommario	8
List of figures	12
List of tables	19
List of acronyms	21
Chapter 1	22
1. Introduction and state of art.....	22
1.1. Introduction	22
1.1.1. Awake neurosurgery and intra-operative electrical stimulation	22
1.1.2. The Active project (FP7-ICT 270460).....	25
1.2. State of art	28
1.2.1. Force's measurements in operating room	28
1.2.2. Measures of forces and moments exerted by the human's head.....	29
1.2.3. Six-components force sensors based on strain gauges	32
1.3. Aim of the work and description of contents	35
Chapter 2	37
2. Materials and methods.....	37
2.1. Mayfield® skull clamp.....	37
2.2. Forces and moments measurements.....	40
2.2.1. Force/stress analytical model.....	40

2.2.2.	Simulation analyses	45
2.2.3.	Experimental setup	50
2.2.4.	Experimental calibration procedure	56
2.2.5.	Signal processing	62
2.2.6.	Moment and forces measurements	66
2.2.7.	Frequency domain analyses	67
2.3.	Head's velocity and accelerations measurements	68
2.3.1.	Experimental setup	68
2.3.2.	Tool's definition	70
2.3.3.	Signal processing	71
Chapter 3	73
3.	Results	73
3.1.	Forces and moments measurements	73
3.1.1.	Simulation results	73
3.1.2.	Experimental results	77
3.1.3.	Signal processing	82
3.1.4.	Intra-operatory measurements of forces and moments	85
3.1.5.	Measurement analyses for events of different classes	87
3.1.6.	Frequency domain results	98
3.2.	Head's displacements, velocity and acceleration measurements	105
Chapter 4	117
4.	Conclusions and discussions	117
4.1.	Simulation analyses	117
4.2.	On-field measurements	119

4.3. Future developments	122
Appendix I	124
References	131

Abstract

This work is part of the European funded project ‘**Active Constraints Technologies for Ill-defined or Volatile Environments**’ (ACTIVE, FP7-ICT 270460). The aim of this project is the design and development of an integrated redundant robotic platform for open skull awake neurosurgery. This a technique that involves some periods during the intervention in which the patient is awake. Awake craniotomies are increasingly used for neuro-oncological operations for tumors involving eloquent regions, since it allows overcoming limitations of classical brain mapping techniques. In fact, for patients who are conscious during the procedure, somatosensory function and cognitive functions, such as language (spontaneous speech, object naming, comprehension, etc), calculation, memory, reading, or writing, can be investigated. The idea is to generate transient disturbances by applying direct electrical stimulation to the cerebral tissue at the level of a functional epicenter; a speech therapist must be present in order to accurately interpret the kind of disorders induced by the cortical and subcortical stimulations.

In this kind of interventions, if we want to use a robot for assistance, one of the major issues is the motion compensation since the target is not fixed because of possible epileptic seizures or patient’s movements during the awake phase; moreover the target of the intervention is a soft tissue undergoing deformations due to many possible causes (tool interaction, orientation with respect to gravity, presence of gas and liquid around it, hydration, pulsing flows, breathing etc.).

To address this problem, one of the main parts that will compose the ACTIVE’s hardware platform is the **Active Headframe (AH)**. This will be a parallel kinematic machine in charge of actively controlling the skull movements and directly attached to the patient’s cranium trough an headring, like the one used today for most of neurosurgical operations. Thanks to the AH, the force/displacements exerted by the head will be variably limited, filtered and compensated, thus increasing the safety of the surgical procedure.

The main goal of this master thesis work was the estimation through on-field measurements of forces and moments applied on a pinion head-holder (the Mayfield® skull clamp) by the patient's head during an awake intracranial operation. In particular we aimed to provide quantitative requirements for the AH design and implementation.

The strains on the Mayfield® positioning system were estimated attaching six double strain gauges (SG) and loads applied on the structure were calculated through a calibration procedure. In order to identify SG's positions we realized a CAD model of the positioning system and performed simulation analyses based on **Finite Elements Method (FEM)**. We identified six SG's positions on the structure that are sufficient to determine forces' and moments' components.

The experimental calibration procedure was carried out using a system of weights and pulleys and applying known loads directly on the positioning system (the configuration of its arms was the same used during the intervention).

On field measurements of forces and moments were acquired during surgical removal of a left frontal lobe ganglioglioma (type III) intervention that lasted about 6 hours; the patient was a 41 years old and his weight was 84 kg. The static components of forces given by the head's and the c-clamp's weight were measured and evaluated in relation to the patient's position with respect to the headring.

The SG's output signals were processed through low-pass filters and detrending procedures.

All the events occurred during the intervention were divided in four different types. This classification was done in order to understand if forces' and moments' values depend on who is exerting loads (patient or surgeon) or on the type of patient's movement (unexpected or induced by stimulation). The obtained results shows that maximum forces and moments are exerted by the medical staff; they shows also that forces and moments due to unexpected movements of the patient are higher with respect to those due to movements induced by stimulation or requested by the surgeon.

Maximum values of forces and moments during the intervention (105 N for force along x direction and 42 Nm for moment around y axis) were found during the phase of the

surgical operation in which the surgeon uses the surgical drill in order to open the skull and in the last phase of the intervention during suturing. Observing maximum values of moments and forces exerted by the patient, we found that they are lower than those found in literature for studies that aimed to measure maximum force and torques exerted by neck muscles (155.4N for isometric force and 69.42Nm for torque).

Results of analyses in frequencies domain showed that for all the types of events the frequency content of all the force's and moment's components is in the range 0-5 Hz with a great prevalence of components between 0 and 0.5 Hz.

We measured also head displacements using an optical tracking system and head's velocities and accelerations were calculated. The results obtained confirmed what we found in forces' and moments' analyses since the maximum values were found during surgeon's actions (9 mm for displacements, 0.06 m/s for velocity and 0.8 m/s² for acceleration). These data represent a starting point for AH sizing and design.

Future developments of this work could be other on-field measurements in order to find possible relationships between values of forces and moments and patients' characteristics such as age, sex or weight.

An improvement in data interpretation could be expected by integrating the evaluation of the load's signals with analysis of vital parameters monitoring signals (ECG, EEG or blood pressure), EMG or electrical stimulation signals (e.g. MEP). Finally, in order to have more useful data for AH design, other intra-operative measurements are desirable in order to collect data during other accidental events, such as epileptic seizures.

Sommaro

Il lavoro qui presentato si inserisce nel progetto finanziato dall' Unione europea 'Active Constraints Technologies for Ill-defined or Volatile Environments' (ACTIVE, FP7-ICT 270460).

Lo scopo di questo progetto è lo sviluppo di una piattaforma robotica integrata e ridondante per la neurochirurgia a cranio aperto con paziente sveglio. Questa tecnica prevede periodi durante l'intervento chirurgico in cui il paziente è in stato di veglia. Le craniotomie a paziente sveglio sono sempre più utilizzate per interventi neuro-oncologici in aree eloquenti della corteccia, poiché permettono di superare i limiti che contraddistinguono tecniche classiche di brain mapping. Infatti, con pazienti coscienti durante la procedura chirurgica, è possibile testare funzioni somatosensoriali e cognitive come linguaggio (linguaggio spontaneo, associazione di nomi e oggetti, comprensione,..) calcolo, memoria, lettura o scrittura. L'idea è di generare disturbi transitori tramite stimolazione elettrica diretta sul tessuto cerebrale a livello degli epicentri funzionali; in sala è presente un logopedista che ha il compito di interpretare correttamente il tipo di disturbi indotti dalla stimolazione corticale e subcorticale.

In questo tipo di interventi, se si ricorre all'assistenza da parte di un robot, uno dei maggiori problemi è la compensazione del movimento poiché l'organo target non ha una posizione fissa a causa della possibile insorgenza di crisi epilettiche o di movimenti del paziente durante la fase di veglia; inoltre l'organo su cui si interviene è un tessuto molle che può deformarsi per molteplici cause (interazione con lo strumento chirurgico, orientamento rispetto alla direzione d'azione della forza di gravità, presenza di gas o liquidi intorno ad esso, flussi pulsatili, respiro, etc...).

Per affrontare questo problema, una delle parti più rilevanti che comporranno la piattaforma HW del sistema realizzato in ACTIVE è l'Active Headframe (AH). Esso sarà costituito da una macchina a cinematica parallela con il compito di controllare i movimenti

della testa e direttamente connessa al cranio del paziente attraverso un *headring*, simile a quello utilizzato oggi per la maggior parte delle operazioni neurochirurgiche. Grazie all'AH, le forze esercitate dalla testa ed i suoi spostamenti saranno limitati, filtrati e compensati, aumentando così la sicurezza della procedura chirurgica.

L'obiettivo principale di questo lavoro era la stima tramite misure in sala operatoria di forze e momenti esercitati dalla testa del paziente su una testiera (Mayfield® skull clamp) durante un'operazione intracranica a paziente sveglio. In particolare lo scopo era quello di fornire dati quantitativi utili alla definizione delle specifiche di progettazione e implementazione dell'AH.

Le deformazioni locali del dispositivo di posizionamento Mayfield sono state misurate utilizzando un sistema di sei estensimetri doppi, mentre i carichi esercitati sulla struttura sono stati calcolati attraverso una procedura di calibrazione. Con lo scopo di identificare le posizioni in cui incollare gli estensimetri abbiamo realizzato un modello CAD del dispositivo di posizionamento ed effettuato simulazioni basate su metodo a elementi finiti. Abbiamo identificato sei posizioni sulla struttura, sufficienti per determinare le tre componenti di forza e momento, in cui collocare gli estensimetri.

La procedura di calibrazione sperimentale è stata effettuata utilizzando un sistema di pesi e pulegge e applicando carichi noti direttamente sul dispositivo di posizionamento (la configurazione dei bracci che lo compongono è rimasta invariata rispetto a quella utilizzata nel corso dell'intervento).

Le misure in sala di forze e momenti sono state acquisite durante un intervento di rimozione chirurgica di un ganglioglioma di tipo III situato nel lobo frontale sinistro della durata di circa 6 ore; il paziente aveva 41 anni e il suo peso era di 84 kg. E' stata misurata la componente di forza statica dovuta al peso della testa e del Mayfield® skull clamp e i risultati sono stati analizzati in relazione alla posizione della testa del paziente rispetto alla testiera. Il segnale di output degli estensimetri è stato processato utilizzando un filtro passa basso e una procedura di detrending.

Tutti gli eventi accaduti durante l'intervento sono stati suddivisi in 4 tipi differenti. Questa classificazione è stata fatta con lo scopo di capire se i valori di forze e momenti dipendono

da chi esercita i carichi (il paziente o il chirurgo) e dal tipo di movimento del paziente (inatteso o indotto tramite stimolazione). I risultati ottenuti mostrano che i massimi valori di forza e momenti sono esercitati dallo staff medico; si evince anche che forze e momenti dovuti a movimenti inattesi del paziente sono maggiori rispetto a quelli dovuti a movimenti indotti da stimolazione o richiesti dal chirurgo.

I valori massimi di forze e momenti durante l'intervento (105 N per la forza in direzione x e 42Nm per il momento intorno all'asse y) sono stati misurati durante la fase dell'operazione in cui il chirurgo utilizza il trapano chirurgico per l'apertura del cranio e nell'ultima fase dell'intervento durante l'operazione di sutura. Osservando i valori massimi di forze e momenti esercitati dal paziente, abbiamo rilevato che essi sono minori rispetto a quelli trovati in letteratura proposti da studi che si ponevano l'obiettivo di misurare le forze e i momenti massimi esercitati dai muscoli del collo (155.4N per la forza isometrica and 69.42Nm per il momento).

I risultati dell'analisi nel dominio delle frequenze hanno mostrato che per tutti i tipi di eventi il contenuto in frequenza di tutte le componenti di forza e momento è racchiuso nel range 0-5Hz, con una netta prevalenza delle componenti tra 0 e 0.5Hz.

Abbiamo anche misurato gli spostamenti del cranio utilizzando un sistema di localizzazione ottico ed abbiamo calcolato velocità ed accelerazione della testa.

Il risultato ottenuto ha confermato ciò che avevamo dedotto dall'analisi di forze e momenti poiché i massimi valori sono stati trovati in corrispondenza delle azioni del chirurgo (9 mm per gli spostamenti, velocità massima di 0.06 m/s e accelerazioni massime di 0.8 m/s²). Tali dati sono da considerare come un punto di partenza per la progettazione e il dimensionamento dell'AH.

Sviluppi futuri di questo lavoro potrebbero essere ulteriori misurazioni in sala operatoria con l'obiettivo di trovare possibili relazioni tra valori di forze e momenti e caratteristiche del paziente quali l'età, il sesso o il peso. Si può ipotizzare un miglioramento nell'interpretazione dei dati integrando l'interpretazione dei segnali dei carichi agenti sulla testiera con lo studio dei segnali di monitoraggio dei parametri vitali (ECG, EEG o pressione sanguigna), EMG o segnali relativi alla stimolazione elettrica (e.g MEP).

Infine, con lo scopo di ottenere ulteriori dati utili per la progettazione dell'AH, altre misurazioni potrebbero consentire di avere a disposizione dati relativi ad altri tipi di eventi accidentali, come ad esempio l'insorgenza di crisi epilettiche.

List of figures

Fig. 1: intra-operative photograph of a craniotomy with grid placement. [5].....	23
Fig. 2: Schematic of HW platform, where LWR and EE are the 7DoF robotic arm and the end-effector, respectively, of each station. The skull is rigidly attached to the AH through an headframe.[7].....	27
Fig. 3: Experimental setup for moments' measure. [11].....	30
Fig. 4: Shoe-shape structure with two force sensors of Maltese cross shape.....	33
Fig. 5: representation of the novel force-sensing member [18].....	34
Fig. 6: positioning of a pinion head-holder for a craniotomy [20]. Three pins penetrate the scalp and are firmly fixed to the outer table of the cranium. A, position of the headholder for a unilateral or bilateral frontal approach. B, position for a pterional or frontotemporal craniotomy. C, position for a retrosigmoid approach to the cerebellopontine angle. D, position for a midline suboccipital approach. E, position for a midline suboccipital approach with the patient in the semi-sitting position.....	38
Fig. 7: Mayfield® Ultra 360 Patient Positioning System.	39
Fig. 8: A. Mayfield® Triad™ Skull Clamp. Skull pins and connection point with the positioning system are highlighted. B. Example of Mayfield Clamp and Mayfield® patient positioning system locked together.	40

Fig. 9: representation of force's measurements starting from SG's output, through the calibration procedure. On the left the case of simulation analyses and on the right the procedure for on- field measurements. 43

Fig. 10: Mayfield CAD model. Joints which allow one degree of freedom of rotation are highlighted in red. The skull clamp can be attached to the bolt (black circle). 45

Fig. 11: Constrains and point of application of forces and moments on the pinion of the positioning system (in orange the parts where mesh was realized using tetragonal elements). 47

Fig. 12: color map that represents strains along y direction of faces whose normal is along x direction in the case of application of a force along z direction (blue arrow). 48

Fig. 13: SG positions on the Mayfield® patient positioning system. 49

Fig. 14: two element 90° tee rosettes for flexion (on the left) and torque (on the right) measurements. 51

Fig. 15: Wheatstone bridge configuration: R_3 and R_4 are the resistances composing our double SGs. R_1 and R_2 are not sensible to the strains. 51

Fig. 16: NI 9237 Bridge Module (on the left) and NI Compact DAQ (on the right). 53

Fig. 17: representation of experimental setup for signal acquisition (strain gauges (A), Bridge Modules (B), battery (C) and notebook (D)). 54

Fig. 18: On the left Mayfield clamp, SG (red circle) and wires that connect SG and DAQ (yellow circle). On the right an image of the user interface during the signal acquisition.. 55

Fig. 19: patient's head attached to the skull clamp immediately before the intervention. ..	55
Fig. 20: reference frame representation.....	57
Fig. 21: application of force along x direction.	58
Fig. 22: example of application of a force along z direction. The red circle highlights a bubble level, the yellow one the pulley, while the green circle highlights the weight applied.	59
Fig. 23: Application of the moment around y direction: we can see the blue arm attached to the terminal pin of the clamp.....	60
Fig. 24: representation of vectors \vec{F} , \vec{b} and angle α	61
Fig. 25: magnitude and phase response of the equiripple filter that we used.....	63
Fig. 26: Forces and moments signals during the entire intervention (results obtained without the detrending procedure).....	64
Fig. 27: schematization of the detrending procedure	65
Fig. 28: Polaris Vicra [®] measurement volume.	69
Fig. 29: Representation of the experimental setup: the red arrow indicates the Polaris Vicra [®] , while the blue circle highlights the tool attached to the C-clamp.	70
Fig. 30: Relationship between voltage output [V/V] of SG5 and force's and moment's components obtained in simulated calibration.	74

Fig. 31: relationship between voltage output [V/V] of SG5 and force's and moment's components obtained in experimental calibration. 78

Fig. 32: SG 5 output during the entire intervention before the detrending procedure 82

Fig. 33 SG 5 output during the entire intervention (smoothed signal) 83

Fig. 34: SG 5 output during the entire intervention (detrended signal)..... 83

Fig. 35: SG 5 output during the entire intervention (final result after the signal processing) 84

Fig. 36: forces and moments acting on the Mayfield[®] clamp positioning system during the example of surgeon action..... 88

Fig. 37: histograms that represent the number of occurrences of load's values for the surgeon action..... 89

Fig. 38: forces and moments acting on the Mayfield[®] clamp positioning system during the example of stimulation induced movement..... 90

Fig. 39: histograms that represent the number of occurrences of load's values for stimulation induced movement..... 91

Fig. 40: forces and moments acting on the Mayfield[®] clamp positioning system during the example of patient movement..... 92

Fig. 41: histograms that represent the number of occurrences of load's values for patient movements..... 93

Fig. 42: forces and moments acting on the Mayfield [®] clamp positioning system during the example of accidental movement.	94
Fig. 43: histograms that represent the number of occurrences of load's values for accidental movements.....	95
Fig. 44: summary of results obtained for force's measurements. The highness of the colored bars indicates the median value, while the black bars indicate the 1 st and 3 rd quartiles. Blue brackets shows the statistical differences.....	96
Fig. 45: summary of results obtained for moment's measurements. The highness of the colored bars indicates the median value, while the black bars indicate the 1 st and 3 rd quartiles. Blue brackets shows the statistical differences.....	97
Fig. 46: single-sided amplitude spectrum for the three components of force and moment (example of surgeon actions). Zoom around low frequencies.....	98
Fig. 47: single-sided amplitude spectrum for the three components of force and moment (example of stimulation induced movements).....	99
Fig. 48: single-sided amplitude spectrum for the three components of force and moment (example of patient movements).	100
Fig. 49: single-sided amplitude spectrum for the three components of force and moment (example of accidental movements).....	101
Fig. 50: force along x direction during the offset acquisition	102

Fig. 51: single-sided amplitude spectrum of force along x direction during the offset acquisition (zoom)..... 102

Fig. 52: force along z direction signal during the segment 6 acquisition (temporal window of about 30s)..... 103

Fig. 53: single-sided amplitude spectrum of force along z direction during the segment 6 acquisition (zoom)..... 103

Fig. 54: 3-D graphs representing the spectrograms of the F_x signal are shown: along the three axis, the frequency, the time and PSD are reported. A colour map helps to visualize the values obtained in PSD axis. Each graphs refers to a different type example..... 104

Fig. 55: histograms representing the distributions of displacements, velocities and accelerations values for surgeon actions. 107

Fig. 56: displacements', velocities' and accelerations' values during the example of surgeon action (skull opening). 108

Fig. 57: histograms representing the distributions of displacement, velocity and acceleration values for patient movements..... 110

Fig. 58: displacements', velocities' and accelerations' values during the example of patient movement. 111

Fig. 59: histograms representing the distributions of displacement's, velocities' and accelerations' values for accidental movements. 113

Fig. 60: displacements', velocities' and accelerations' values during the example of accidental movement..... 114

Fig. 61: summary of results obtained for displacement measurements. The highness of the blue bars indicates the median value, while the red bars indicate the 1st and 3rd quartiles. Blue brackets shows the statistical differences between the groups. 115

Fig. 62: summary of results obtained for velocity measurements..... 116

Fig. 63: summary of results obtained for velocity measurements..... 116

List of tables

Tab. 1: technical specifications of SGs.	52
Tab. 2: technical specifications of NI Compact DAQ and NI 9237 Bridge Module.	52
Tab. 3: loads applied during experimental calibration	57
Tab. 4: calibration residual error for simulation analyses. From left to right we find respectively the load applied, the percentage error and the absolute error.....	76
Tab. 5: results obtained in simulation test. From left to right we find respectively the applied load, the percentage error and the absolute error. In black the results of the first simulation test and in red those of the second test.	77
Tab. 6: coefficients of determination of the linear model that correlates SG outputs and load applied. The critical cases with $R^2 < 0.7$ are highlighted in red.	79
Tab. 7: residual error for experimental calibration. From left to right we find respectively the load applied, the percentage error and the absolute error.....	81
Tab. 8: maximum values of forces [N] and moments [Nm] during the entire intervention.	86
Tab. 9: contribution of static forces and moments given by the head's and c-clamp's weight.	86

Tab. 10: results of statistical analyses of forces' and moments' values in each temporal instant for the surgeon actions; we report the maximum value, the median and the values of the 1 st and 3 rd quartile.....	89
Tab. 11: results of statistical analyses of forces' and moments' values for stimulation induced movements.....	91
Tab. 12: results of statistical analyses of forces' and moments' values for patient movements.....	93
Tab. 13: results of statistical analyses of forces' and moments' values in each temporal instant for accidental movements.....	95
Tab. 14: results of statistical analyses of displacements', velocities' and accelerations' values in each temporal instant for surgeon actions.....	106
Tab. 15: results of statistical analyses of displacements', velocities and accelerations' values in each temporal instant for patient movements.....	109
Tab. 16: results of statistical analyses of displacements', velocities' and accelerations' values in each temporal instant for accidental movements.....	112
Tab. 17: results summary of the intervention. In the third column there are the main events occurred during the intervention. In the following columns mean (first row) and maximum (second row) value for forces [N] and moment [Nm] during each temporal segment of the intervention are reported.....	125

List of acronyms

ACTIVE = Active Constraints Technologies for Ill-defined or Volatile Environments

FP7 = Seventh Framework Programme

HW = Hardware

SW = Software

LWR = Light Weight Robots

AH = Active Headframe

LGG = Low Grade Glioma

FEM = Finite Elements Method

SG = Strain Gauges

DFT = Discrete Fourier Transform

STFT = Short Time Fourier Transform

Chapter 1

1. Introduction and state of art

1.1. Introduction

This work is about on field measurements acquired during an awake neurosurgery intervention for brain tumor resection: in the following paragraph a brief description of this surgical scenario is presented.

1.1.1. Awake neurosurgery and intra-operative electrical stimulation

Recent advances in functional brain imaging in healthy volunteers have shown that there is a large inter-individual variability in the functional organization of the brain [1]. These advances have also proved the existence of great plasticity within the central nervous system. In particular, they shown short-term and long-term redistributions of functional maps have been described for individual people (“natural plasticity”) and the capacity of the brain to reorganize itself in patients who present acute cerebral lesions (“postlesional plasticity”). Also more progressive lesions such as slow growing tumors - in particular low-grade gliomas (LGGs) - induce a large functional reshaping. As a consequence, a new approach to brain-tumor surgery should take into account dynamic interactions between the natural history of the tumor and the reactive process of cerebral adaptation. Such an approach, applied to each patient and each tumor, should allow specific selection of

surgical indications that maximize the quality of glioma resection while minimizing the risk of irreversible postoperative deficits. [2]

The most sophisticated preoperative imaging techniques allow making assumptions about the role of regional brain anatomy and its function, and these assumptions may not correctly predict integrated brain function during tumor resection. Even electrophysiological monitoring of both spontaneous and evoked responses is well known to suffer from both false-positive and false-negative errors.[3] Instead, an awake cooperative patient is capable to undergo neurocognitive and sensory-motor testing in order to minimize postoperative neurological dysfunction making a functional brain mapping.

The purpose of the mapping procedure is to reliably identify cortical areas and subcortical pathways involved in motor, sensory, language, and cognitive function. Although similar techniques are utilized, the application of mapping at different centers involves a diversity of approaches.[4]

Invasive electrophysiological investigations currently remain the “gold-standard” when operating on tumors in eloquent cortical or subcortical structures. In particular, somatosensory and motor evoked potentials are widely used for intra-operative identification of the sensorimotor region.

This method consists of surgically putting electrodes directly onto the brain surface, thus enabling invasive electrocorticographic recordings and direct cortical stimulation at the same time (*Fig. 1*) [2].

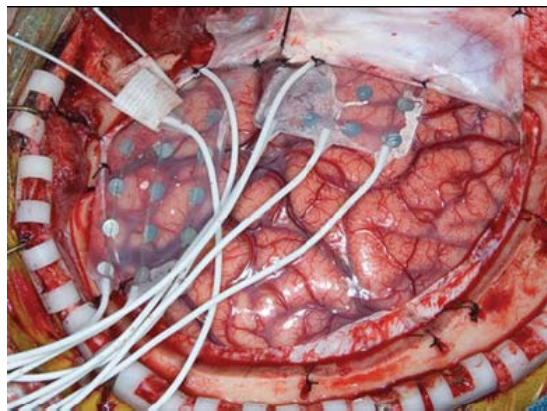


Fig. 1: intra-operative photograph of a craniotomy with grid placement. [5]

A limitation of this technique is that evoked potentials cannot be used to map language, memory, or other higher functions. In addition, two surgical procedures are needed, one to implant the grids and one to resect the tumor. Finally, there is a notable risk of infection resulting from the presence of the implanted grid during several days of assessments.[2]

The limitations of the different mapping techniques can be most effectively complemented by the awake craniotomy. This a neurosurgery technique that involves some periods during the intervention in which the patient is awake. Awake craniotomies are increasingly used for epilepsy surgery and neuro-oncological operations for tumors involving eloquent regions such as the motor/sensory strip, speech/language centers and thalamic regions.[6]

Direct electrical stimulation allows the mapping of motor function by inducing involuntary movement if a motor site is stimulated. For patients who are conscious during the procedure, somatosensory function (by eliciting dysaesthesia described by the patient) and cognitive functions, such as language (spontaneous speech, object naming, comprehension, etc), calculation, memory, reading, or writing, can be investigated. The idea is to generate transient disturbances by applying direct electrical stimulation to the cerebral tissue at the level of a functional “epicenter”.

A speech therapist must be present in order to accurately interpret the kind of disorders induced by the cortical and subcortical stimulations (e.g. speech arrest, anarthria, speech apraxia, honological disturbances, semantic paraphasia, perseveration, and anomia).[2]

1.1.2. The Active project (FP7-ICT 270460)

This work is part of the European funded project ‘Active Constraints Technologies for Ill-defined or Volatile Environments’ (ACTIVE). The aim of the project is the design and development of an integrated redundant robotic platform for open skull epilepsy surgery executed with the patient asleep or awake (cfr §1.1.1).

One of the major issues in robotic neurosurgery is the **motion compensation**, since the target of the intervention is a soft tissue undergoing deformations due to many possible causes (tool interaction, orientation with respect to gravity, presence of gas and liquid around it, hydration, pulsing flows, breathing etc.). Other target’s displacements can occur because of epileptic seizures or patient’s movements in the case of awake neurosurgery.

The question is relevant because this type of interventions requires an high accuracy and the displacements described above are almost unpredictable.

The Active system will have three working modes [7]:

- **Completely autonomous:** the robot could autonomously move inside or outside the surgical field.
- **Tele-operated:** the robots act as slaves of an haptic master station that compensates for most of the skull’s and brain’s movements autonomously.
- **Hands-on:** the surgeon acts as direct master for the slave arms (impedance control mode).

The robotic system will be composed of a Hardware (HW) Platform and a Software (SW) Platform that provide robot path planning and control, tissue modeling, generation of dynamic constraints, on field learning and decision making.

The main components of the HW platform are [7]:

- two cooperating 7 DoF **L**ight **W**eight **R**obots (LWR, KUKA[®] LWR4+) with a neurosurgical tool as end-effector.
- two masters stations that allow the surgeon to perform the operation guiding the haptic interfaces with visual and force feedback from the surgical scene.
- An **A**ctive **H**eadframe (AH) holding the patient head, which mounts a detachable headring fixed with pins to the skull of the patient (cfr§2.1) . The AH is actuated by a parallel kinematic machine in charge of actively controlling the skull movements. In particular, the AH controls the mechanical impedance of the head-ring according to the impedance behavior defined or required by the surgeons. In this way force/displacements exerted by the head are variably limited, filtered and compensated, thus increasing the safety of the surgical procedure. As shown in *Fig. 2* all the components of the HW platform share a common reference frame.

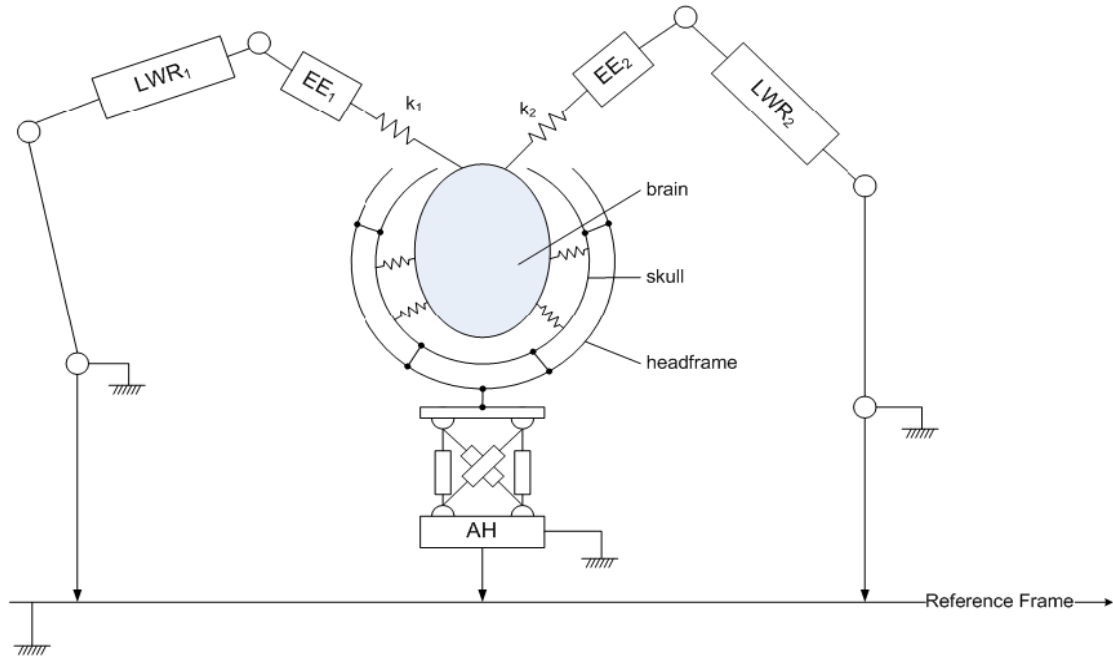


Fig. 2: Schematic of HW platform, where LWR and EE are the 7DoF robotic arm and the end-effector, respectively, of each station. The skull is rigidly attached to the AH through an headframe.[7]

One of the major progresses beyond the state of art is in the field of motion compensation. Solutions to the problem of involuntary quasi-static motions (tremors, respiratory motion, heartbeat) have been investigated in recent years. The ACTIVE system is designed to work also in awake neurosurgery surgical procedures with patients under local anesthesia condition: in this situation soft tissue motion and skull movements (due to patient's voluntary actions or epileptic seizures) are unpredictable and not modeling as disturbance.

1.2. State of art

1.2.1. Force's measurements in operating room

We did not find any reference in literature about measurements of forces and torques excited by the patient's head during awake neurosurgery interventions.

Much work has been done on vital signs (e.g. heart rate, respiratory rate, blood pressure, blood saturation) monitoring during surgical operations. In this paragraph we report studies about measures of forces and torques in operating room.

In [8] the results of a study of forces and torques applied at the tool/hand interface generated during laparoscopic surgery are shown. The experimental setup was composed by an instrumented laparoscopic grasper with interchangeable standard surgical tips equipped with a three-axis force/torque sensor located at the proximal end of the grasper tub. In addition, one axis force sensor located at the grasper's handle was used to measure the grasping force. Data were collected during ten cholecystectomies and Nissen funduplications in a porcine model.

The proposed technology and methodology was developed in order to help in training novice surgeons, designing simulators, and measuring technical proficiency during laparoscopic surgery.

An interesting study is described in [9]. Its aim was the introduction of a newly developed device equipped with a contact surface piezoresistive force sensor (FlexiForce); it was used for monitoring extra-ocular compression continuously in patients undergoing uncomplicated fronto-temporal or bifrontal craniotomy for surgical clipping of unruptured anterior circulation aneurysms. The aim of the work was to avoid painful ocular sensation. The authors found that the force increased immediately after retraction of the flap, increased during lower craniotomy close to the orbit ($144\pm 26\text{gf}$), was maintained at $1\pm 18\text{gf}$

during microsurgery, and returned close to baseline at 24 ± 14 gf after restoration of skin flap retraction.

In [10] another measurement of forces is illustrated. In this case handling forces of a mechanically counterbalanced neurosurgical microscope (Zeiss[®] NC4, Zeiss[®], Oberkochen, Germany) were compared with those of a sensor-servo-supported neurosurgical microscope (Moeller[®] HiR 20-1000, Moeller[®], Wedel, Germany). Handling forces were correlated with the surface electromyogram measurement of the forearm muscle activity of 4 neurosurgeons; this signal was acquired while handling the two different microscopes in standardized tests. The electrophysiologic measurement revealed that significantly less muscle activity was required to handle the sensor-servo-driven microscope in all directions.

1.2.2. Measures of forces and moments exerted by the human's head

Literature about measurements of neck muscles strength in various conditions is relevant.

In [11] three-dimensional moments measured during maximum voluntary contractions of neck muscles in humans are described. In *Fig. 3* the experimental setup is shown: an headholder with pads was attached to a 6-axis load cell located behind the subject's head, and thick straps restrained the shoulders and torso.



Fig. 3: Experimental setup for moments' measure. [11]

The magnitudes of extension, flexion, lateral bending, and axial rotation moments were calculated.

Maximum moments were measured in 11 men and 5 women with an average age of 31 years. Anatomic landmarks were digitized to resolve moments at different locations in the cervical spine.

They found that when moments were resolved about axes through the midpoint of the line between the C7 spinous process and the sternal notch, the maximum moments were as 52 ± 11 Nm in the case of extension, 30 ± 5 Nm for flexion and 36 ± 8 Nm for lateral bending. Moreover, the magnitudes of extension, flexion, and lateral bending moments decreased linearly with vertical distance from the lower cervical spine to the mastoid process.

The work presented in [12] aimed at determining the maximal isometric strength of neck muscles and the relationship between forces and different anatomical positions in the body sagittal and coronal planes. The measurement device comprised two separate but interconnected parts that allows isometric torque to be measured at the C7-T1 vertebrae. A four-point restraint and torso strap restrained test subjects' shoulders and torso during measurements.

Strength values measured on 17 healthy males (age range, 24–38 years) demonstrated that extensor muscles yielded the greatest torque and that flexor muscles provided the least torque. Linear regression analyses showed strong association of isometric strength with anatomical positions in the two body planes. Maximum values of isometric neck muscles strength were found for extensor muscles with the head inclined (extension) at an angle of 20° in the body sagittal plane (52.04 Nm) and for left lateral flexor with a 15° left lateral bending of the head in the body coronal plane (31.19 Nm).

In [13] a study that aims to measure human isokinetic neck strength profile is presented; in this case the population considered was composed by senior elite rugby players 24 years old. The experimental setup was similar to those described above: torque production was measured during flexion and extension in the sagittal plane and lateral flexion in the frontal plane. Alignment of the dynamometer's input axis corresponded to the cervical spine's vertebral prominence (C7). They found that the measure of mean peak torque was 44.04 Nm for flexion and 65.50 Nm for extension. For lateral flexion the mean values of peak torque was 69.42 Nm.

An interesting result for our application was achieved in [14]. In this work the isometric force and isometric torque of neck extensor muscles are measured and compared at different levels of thoracic support (i.e support that restrains torso). This is an important consideration because in all studies in which the strength of the neck extensor muscles has been measured, the level of thoracic support has been adjusted differently so that direct comparison of the results is not possible. In [14] the maximum isometric force of the neck extensor muscles was measured on a population of twenty healthy women. The acquisitions were done with the thoracic support located at five different levels. The highest level was set at the level of the spine of the scapula (level I) and the other levels were located 2.5 cm lower than the previous one, with the lowest level set 10 cm below the highest level. The maximum isometric torque for each level was calculated by multiplying the isometric force by the length of the lever arm measured from the upper tip of the

thoracic support to the centre point of the cell load. In our scenario (i.e neurosurgery intervention) the patient's torso is not well restrained and the thoracic support is located near the level V considered in [14].

The maximum isometric force and maximum isometric torque of the neck extensor muscles were increased step by step from 130.5 N to 155.4 N and from 33.7 Nm to 52.7 Nm, respectively.

Analyzing their results it's possible to state that maximum isometric force and maximum isometric torque measurements of the neck extensor muscles vary with the length of the lever arm and only by setting the level of thoracic support at a specific level we can compare the strength of the neck extensor muscles in different studies.

Others parameters that we aimed to measure during the neurosurgical intervention were the head's velocity and acceleration. We did not find any references in literature about this topic. We have to consider that the head movement is constrained by the clamp and the values that we obtained are directly influenced by the stiffness of the clamp itself.

1.2.3. Six-components force sensors based on strain gauges

SGs can be used to measure forces and moments along three orthogonal directions of the space. The design of six-components force sensors based on strain gauges is currently a fairly developed area of research in different fields (e.g. robotics, vehicle mechanics and biomechanical applications).

In [15] a shoe-shape structure that combines two six-axis force sensors placed in the front part and rear part is presented. Those two force sensors are of Maltese cross shape made of aluminum alloy (2024-T8). The four spokes are attached to the rigid rim on one side, and to the square hub at the center.

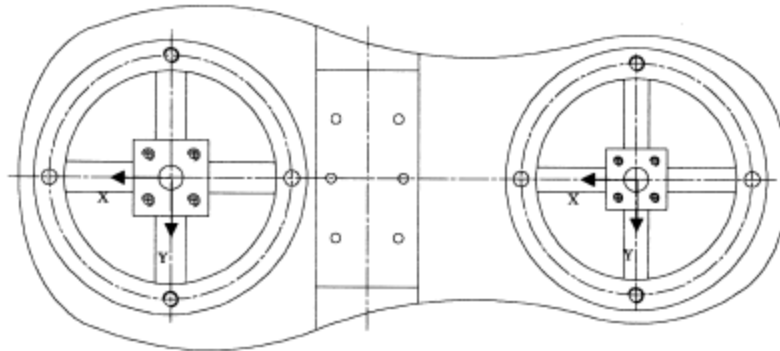


Fig. 4: Shoe-shape structure with two force sensors of Maltese cross shape.

A set of 32 strain-gages combined in a six Wheatstone bridges arrangement, are mounted on the sensor body. In this way the reaction loading of a foot is directly measured and registered during a gait cycle motion. This force sensor system and its measuring process can be applied not only in clinical gait analysis and diagnosis of the osteopathy, but also in the study of biped walking robots and the development of new shoe types for manufacturing.

The aim of the work described in [16] was the development of an humanoid robot foot. In order to walk on uneven terrain safely, the foot should perceive the applied forces and moments to itself, and must control itself using the measured values. The applied forces and moments are measured using 6-axis force/moment sensor attached to the foot. Each sensor should get the different rated load, because the applied forces and moments to foot in walking are different. The structure of the sensor was newly modeled, and the sensing elements (plate-beams) of the sensor were designed by using FEM. Then the 6-axis

force/moment sensor was fabricated by attaching strain-gages on the sensing elements (also in this case a Wheatstone configuration was used).

In [17] the design of a sensor that measures forces and moments acting at the hub of a farm tractor is showed. They chose to use a three-cantilever-spoke structure that carries 12 strain gauges. The bending moments acting at a cantilever-spoke produce high strains at the areas where the strain gauges were intentionally located (SG location was found with a FEM analysis).

In [18] a novel six-component force sensor with its force-sensing member in the form of four identical T-shaped bars is presented. The force-sensing member was subjected to a FEM analysis in conjunction with a design optimization for high measurement sensitivities.

Also a strain compliance matrix (cfr §2.2) analysis was carried out in order to evaluate the measurement isotropy of the developed sensor. They found that their sensor (represented in *Fig. 5*) has a rather good measurement isotropy, as compared to a Maltese crossbar sensor under similar conditions. In addition, only 20 strain gauges are required in the design, which is less than that used in a Maltese crossbar type sensor.

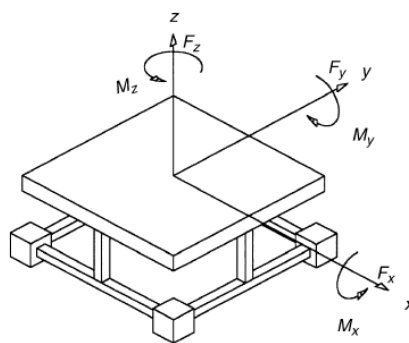


Fig. 5: representation of the novel force-sensing member [18].

In [19] the development of a six-component force/moment sensor is described together with a method for calibration and evaluation of its uncertainty. This quantitative evaluation considers possible sources of errors like the interference between the three components of force and moment, the resolution of the indicator, the non-zero status without a load before and after calibration and hysteresis.

1.3. Aim of the work and description of contents

In the Active scenario a skull clamp like the one showed in (*Fig. 8*) will be used in order to fix the cranium to the AH. The AH will replace the positioning system that connects the skull clamp to the operating table. Our experimental results were used to provide quantitative requirements for the AH design and implementation (bandwidth, amplitude, frequency of occurrence of large loads on the clamp, velocity and acceleration of the head). The main goal of our work was the estimation through on-field measurements of forces and moments applied on a pinion head-holder (the Mayfield[®] skull clamp (cfr§2.1)) by patient's head during an awake intracranial intervention.

We choose to use strain gauge (SG) sensors to measure the strain of the skull clamp during the intervention and then calculate forces and moments applied through a calibration procedure. Head's displacements were measured using an optical tracking system.

In Chapter 2 we introduce the object considered in our study (i.e. Mayfield[®] positioning system) and we explain the force/stress analytical model, the CAD model of the structure and the FEM analysis that was performed to determine the sensors' position.

We describe also the experimental setup used for on-field measurements and the calibration procedure used to calculate forces and moments; we explain also how we acquired data about head's displacements, velocity and acceleration and the data processing.

In Chapter 3 we illustrate the results we obtained in simulation and on-field both in time and frequency domain. In the last chapter we discuss the results and we draw our conclusions; future developments are also discussed.

Chapter 2

2. Materials and methods

In this chapter we introduce the object considered in our study and we explain the force/stress analytical model, the CAD model of the structure and FEM analysis that was performed to determine the sensors' position.

We describe also the experimental setup used for on-field measurements and the calibration procedure used to calculate forces and moments. We also explain how we acquired data about head's displacements and how we calculated velocity and acceleration. Also SG's signals processing and analytical consideration on strain compliance matrix are discussed.

2.1. Mayfield® skull clamp

Most intracranial neurosurgical procedures are performed with the patient in the supine, three-quarter prone (lateral oblique or park-bench), or fully prone position, with the surgeon sitting or standing at the head of the table. The supine position (A, B, E in *Fig. 6*), with appropriate turning of the patient's head and neck and possibly elevation of one shoulder to rotate the upper torso, is selected for procedures in the frontal, temporal, and anterior parietal areas and for many cranial base approaches. The three-quarter prone position (C and D in *Fig. 6*), with the table tilted to elevate the head, is used for exposure of the posterior parietal, occipital, and sub-occipital areas [20].

Precise maintenance of the firmly fixed cranium in the optimal position greatly facilitates the operative exposure.

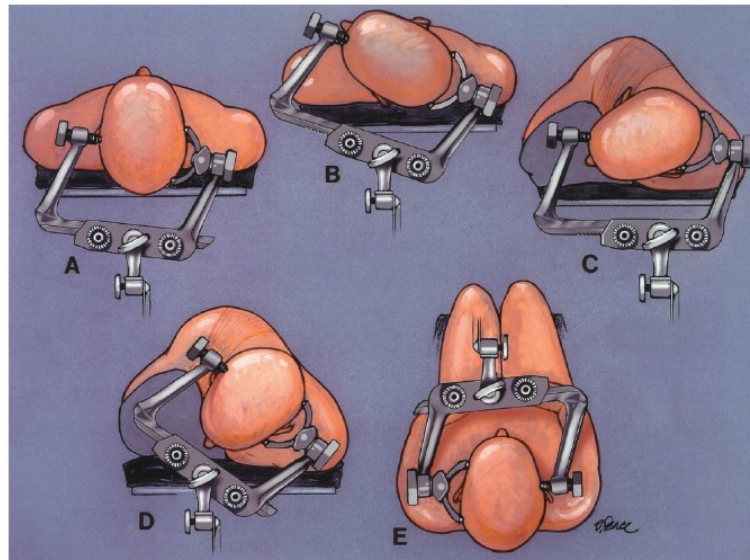


Fig. 6: positioning of a pinion head-holder for a craniotomy [20]. Three pins penetrate the scalp and are firmly fixed to the outer table of the cranium. A, position of the headholder for a unilateral or bilateral frontal approach. B, position for a pterional or frontotemporal craniotomy. C, position for a retrosigmoid approach to the cerebellopontine angle. D, position for a midline suboccipital approach. E, position for a midline suboccipital approach with the patient in the semi-sitting position.

During neurosurgery interventions the head's immobilization is obtained by using a clamp directly fixed in the patient's cranium and connected to the surgical table through an headholder (Mayfield[®] Ultra 360 Patient Positioning System (Integra LifeScience[®], USA) showed in *Fig. 7*.



Fig. 7: Mayfield® Ultra 360 Patient Positioning System.

This positioning system is used to support patients during diagnostic examination or surgical procedures where a rigid support between the surgical table and the Mayfield® skull clamp (*Fig. 8A*) is necessary and positional degrees of freedom are required. The Ultra 360 model is designed for patient positioning in the prone, supine, lateral or sitting position. It connects directly the surgical table (by inserting the two cylinders highlighted in red in *Fig. 7* in a support under the table) to the skull clamp (by means of a bolt, highlighted in black in *Fig. 7*).

The Mayfield® Triad™ Skull Clamp (*Fig. 8A*) is used to give rigid skeletal fixation by inserting the three highlighted pins in the patient's cranium. The two arms can slide over each other to fit different skull dimensions. The skull clamp is connected to the Ultra 360 Positioning System by the bolt highlighted in black in *Fig. 8*, resulting in the configuration of *Fig. 8B*.



Fig. 8: A. Mayfield® Triad™ Skull Clamp. Skull pins and connection point with the positioning system are highlighted. B. Example of Mayfield Clamp and Mayfield® patient positioning system locked together.

After the clamp has been secured on the head, the final positioning is completed and the headholder is fixed to the operating table. This type of immobilization allows intra-operative repositioning of the head.

2.2. Forces and moments measurements

In this paragraph we explain the force/stress analytical model, the CAD model of the structure and the FEM analysis that was performed to determine the sensors' position. We describe also the experimental setup used for on-field measurements and the calibration procedure used to calculate forces and moments

2.2.1. Force/stress analytical model

The aim of the work is the estimation of forces and moments exerted by patient's head on the Mayfield® skull clamp in order to provide quantitative requirements for the AH sizing and design.

We used a system of six double SGs arranged in six half bridge circuit configurations (cfr §2.2.2). Given their voltage output, the magnitudes and directions of three forces ($\vec{F}_x, \vec{F}_y, \vec{F}_z$) and three moments ($\vec{M}_x, \vec{M}_y, \vec{M}_z$) can be calculated as described below.

The entity of the loads applied on the structure (0÷55N for forces and 0÷5.5Nm for moments) allows us to consider only the linear elastic behavior of the clamp, made of an aluminum alloy (yield point for aluminum alloys between 50 MPa and 500 MPa).

Under this hypothesis, we can consider the Mayfield[®] patient positioning system loaded at a particular point (“point of application” in *Fig. 11*), situated on the segment where the C-clamp is attached, by an unknown force vector $\vec{F} = (F_x, F_y, F_z, M_x, M_y, M_z)$ in its linear range. We have to consider also the moments because the force is not directly applied in the point of application, but on the skull pins (*Fig. 8A*).

The force vector produces stress on the surface of the structure that we can measure using SGs: in particular we obtain six output signals [V/V] that compose the vector $\vec{S} = (S_1, S_2, S_3, S_4, S_5, S_6)$, in the six SG’s positions (see *Fig. 13*).

Using the superimposition principle of linear elasticity we can write the following linear relationship (1):

$$\begin{bmatrix} S_1 \\ S_2 \\ S_3 \\ S_4 \\ S_5 \\ S_6 \end{bmatrix} = \begin{bmatrix} c_{11} & c_{12} & c_{13} & c_{14} & c_{15} & c_{16} \\ c_{21} & c_{22} & c_{23} & c_{24} & c_{25} & c_{26} \\ c_{31} & c_{32} & c_{33} & c_{34} & c_{35} & c_{36} \\ c_{41} & c_{42} & c_{43} & c_{44} & c_{45} & c_{46} \\ c_{51} & c_{52} & c_{53} & c_{54} & c_{55} & c_{56} \\ c_{61} & c_{62} & c_{63} & c_{64} & c_{65} & c_{66} \end{bmatrix} \cdot \begin{bmatrix} F_x \\ F_y \\ F_z \\ M_x \\ M_y \\ M_z \end{bmatrix} = [C] \cdot \vec{F} \quad (1)$$

where $[C]$ is a 6x6 matrix called *strain Compliance matrix*.

Each element c_{ij} of the compliance matrix is the ratio between the i_{th} strain signal (in the i_{th} strain measurement location) and the magnitude of the j_{th} force component.

The solution for the force vector can be directly obtained by the matrix inversion operation:

$$\vec{F} = [C]^{-1} \cdot \vec{S} \quad (2)$$

We define $[CM] = [C]^{-1}$ the *Calibration Matrix*, which directly multiplies the strain signal vector to obtain the to-be-measured force vector [18].

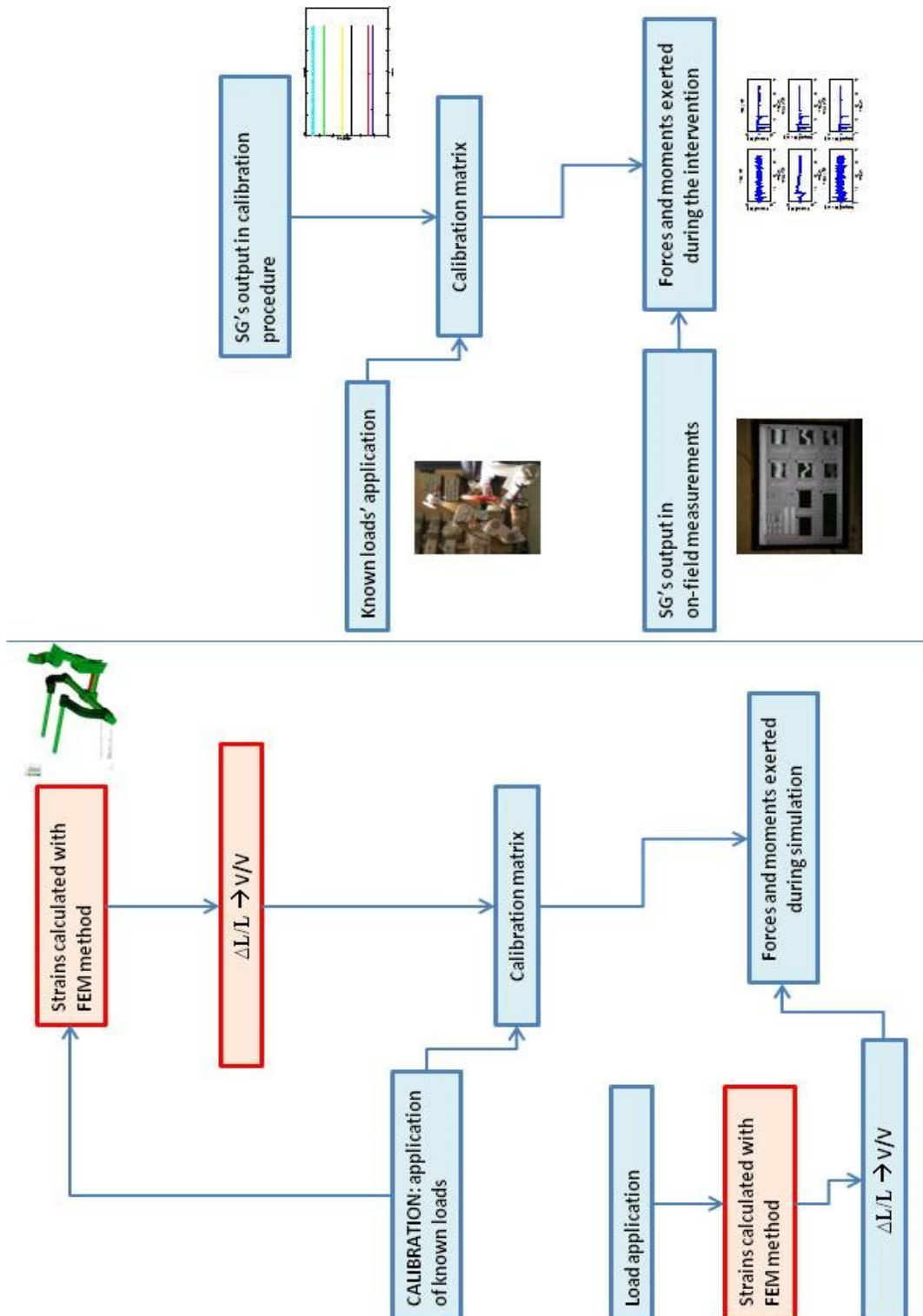


Fig. 9: representation of force's measurements starting from SG's output, through the calibration procedure. On the left the case of simulation analyses and on the right the procedure for on-field measurements.

A sensor that aims at measuring the vector \vec{F} should be designed to be equally sensitive to the all six components. This performance requirement could be controlled defining the *condition number* C_0 of the strain compliance matrix:

$$C_0 = \frac{\sigma_1(C)}{\sigma_6(C)} \quad (3)$$

where σ_1 e σ_6 are the largest and the smallest singular values of matrix $[C]$, respectively.

If the system has perfect structural isotropy and a uniform sensor response for every force component the condition number is unity, i.e. $\sigma_1 = \sigma_6$. For most cases the optimum condition is not obtainable and the condition number is generally greater than unity [21].

If the calibration matrix is diagonal our measurement system is decoupled: it means that the output of a particular strain signal corresponding to a specific force component is not affected by the application of any of the other force components. If this is the case, then:

$$F_i = a_{ii} S_i, \quad i = 1,6, \quad a_{ij} = 0, \quad i \neq j \quad (4)$$

Since our structure is monolithic, a completely diagonal calibration matrix is not obtainable in practice, and therefore various cross sensitivities exist. The cross sensitivities may be defined by the cross sensitivities $(CS)_{ij}$ coefficients (5) [18]:

$$(CS)_{ij} = \frac{c_{ij}}{\sum_{j=1}^6 |c_{ij}|} \quad (5)$$

where c_{ij} are the elements of the strain compliance matrix.

For an ideal decoupled system:

$$(C_{ij}) = 0, \quad i \neq j \quad (C_{ij}) = 1, \quad i = j \quad (6)$$

since the strain compliance matrix is diagonal.

2.2.2. Simulation analyses

We measured the Mayfield[®] patient positioning system using a caliper in order to build the virtual 3D models. The CAD model of the Mayfield[®] patient positioning system (*Fig. 10*) was realized using the 3D CAD design software *Solidworks[®] Premium 2009* (Dassault Systèmes, Vélizy, France).

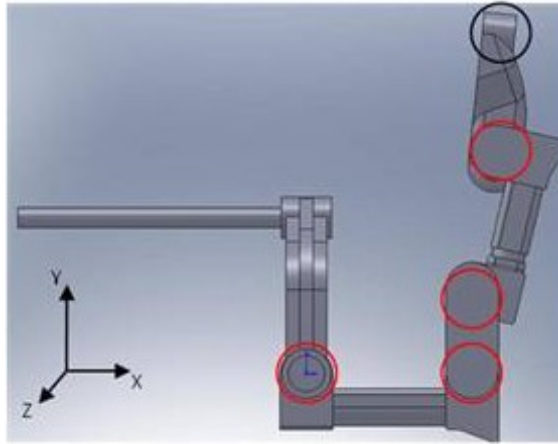


Fig. 10: Mayfield CAD model. Joints which allow one degree of freedom of rotation are highlighted in red. The skull clamp can be attached to the bolt (black circle).

Red circles in *Fig. 10* identify the joints that allow rotations around the z axis, while the black one highlights the point where the skull clamp is attached. In the CAD model it's possible to modify the configuration of the articulated arm by setting the relative angle between the segments.

The meshing procedure and the simulation tests were realized using the finite element analysis software *Abaqus[®] 6.9* (DassaultSystèmes, Vélizy, France). We used the configuration shown in *Fig. 10*, used in most of the surgical interventions.

The object's mesh was realized using both tetragonal and hexahedral elements. Tetragonal elements were used to construct the mesh of geometrically irregular segments of the structure (highlighted in orange in *Fig. 11*), while hexahedral elements were used for the remaining parts.

The dimension of the elements was selected according to the geometric features of different parts trying to avoid an excessive distortion of the elements themselves.

To evaluate the results of our meshing procedure two different metrics were used:

- *Aspect ratio*: ratio between the longest and shortest edge of an element.
- *Geometric deviation factor*: measure of element edge deviation from the original geometry. This value is calculated by dividing the maximum gap between an element edge and its parent geometric face or edge by the length of the element edge.

For both tetragonal and hexahedral elements, we report the number (and the percentage value on the total number of elements) of mesh elements with an aspect ratio value greater than 10 and the average aspect ratio. We show also the number of elements with geometric deviation factor greater than 0.2, the average and the worst geometric deviation factors.

We obtained the following results:

- ✓ Tetragonal elements: Aspect ratio > 10: 41 (0.00599993% of tetragonal elements)
Average aspect ratio: 1.58
- ✓ Hexahedral elements: Aspect ratio > 10: 0 (0%)
Average aspect ratio: 1.55
- ✓ Tetragonal and hexahedral elements:
Geometric deviation factor > 0.2: 193 (0.0275% of elements)
Average geometric deviation factor: 0.00417
Worst geometric deviation factor: 0.207

Simulation tests were performed assuming the two cylindrical segments shown in *Fig. 11* constrained to the surgical bed and vector \vec{F} applied on a single point (connection point between the skull clamp and the positioning system). We assumed the cranium and the skull clamp as a unique rigid body that exerts forces and moments on the positioning system.

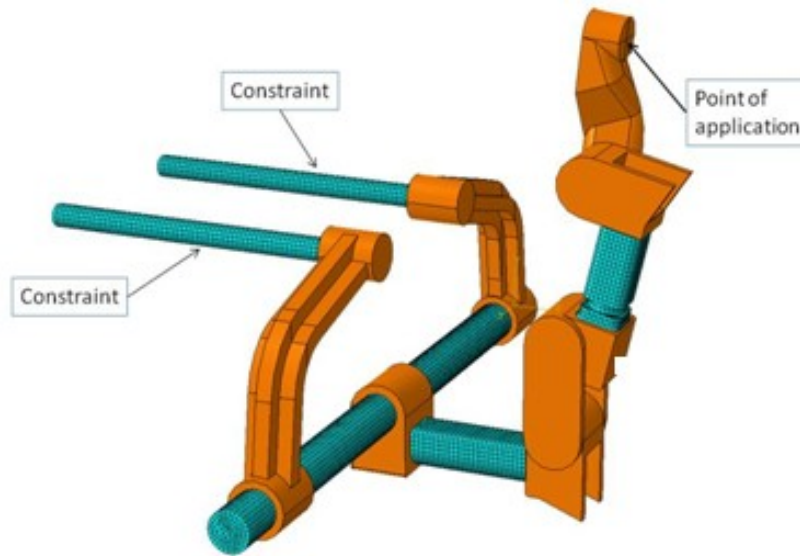


Fig. 11: Constrains and point of application of forces and moments on the pinion of the positioning system (in orange the parts where mesh was realized using tetragonal elements).

Simulation analyses were performed in order to find the parts of the structure with maximum strains. Considering the SG's configuration described in §2.2.3, we observe that SG's output is directly proportional to $(\varepsilon_1 - \varepsilon_2)$ and it is possible to determine the strain gauge positions so that $(\varepsilon_1 - \varepsilon_2)$ is maximized.

We found the optimal strain gauge positions applying forces (50N max) and moments (15Nm max) along x, y and z axis (*Fig. 10*).

After that, with the help of color maps like the one shown in *Fig. 12*, we manually searched pairs of adjacent elements where the differences between strains along two perpendicular directions were significant (difference greater than $3 \times 10^{-2} \mu\varepsilon$).

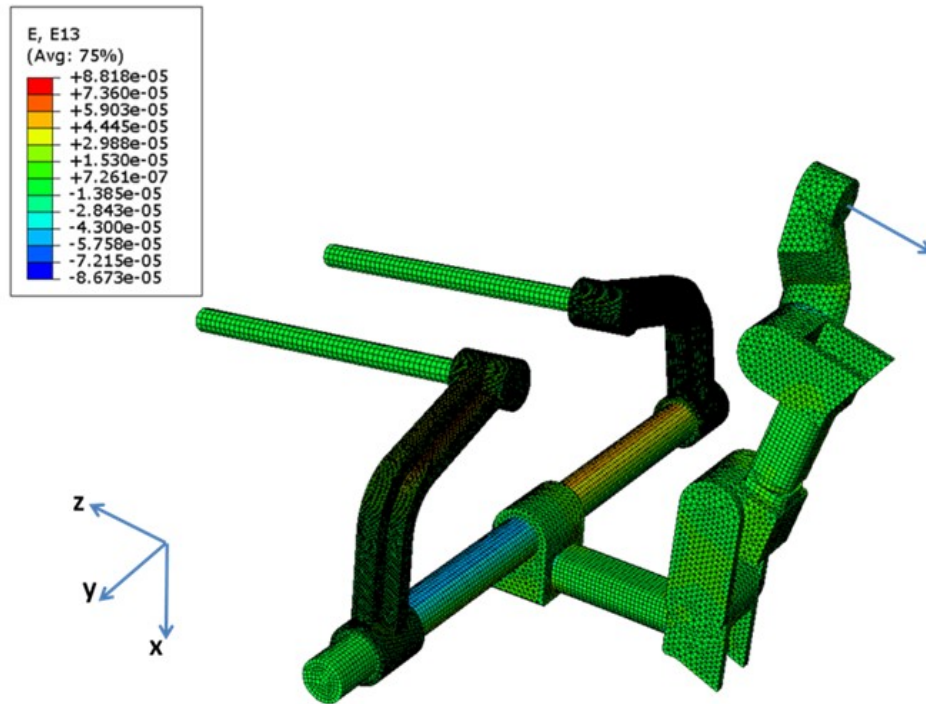


Fig. 12: color map that represents strains along y direction of faces whose normal is along x direction in the case of application of a force along z direction (blue arrow).

The measurements locations where we bounded the SGs are shown on *Fig. 13*, where F denote 90° tee SG rosettes for flexion measurements, while T indicates 90° tee SG rosettes for torque measurements (cfr §2.2.3).

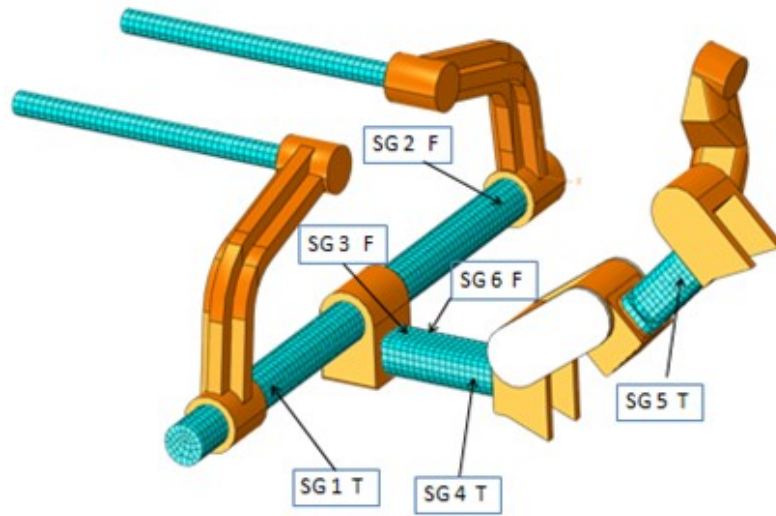


Fig. 13: SG positions on the Mayfield® patient positioning system.

Our choice in SGs positioning was also influenced by the need to not create disturbance for the medical staff and to not limit the relative movements between each arm of the structure. For this reason we could not attach a greater number of sensors and we could not consider all the parts of the structure as possible SG's locations.

We computed the coefficients c_{ij} of the strain compliance matrix (virtual calibration procedure) by applying forces and moments of different magnitudes (the same applied in experimental calibration shown in *Tab. 3*) along the x, y and z axis and computing the SG output. As specified above subscript i indicates the strain gauge signal, while subscript j indicates the element of the vector \vec{F} . For instance, the element c_{46} was calculated by applying moments of different magnitudes around z axis and by measuring the voltage output of strain gauge 4.

During the simulation tests we found a linear relationship between forces or moments applied and SG voltage output (see §3.1.1); we calculated the coefficients of the strain compliance matrix as the slope of the line representing the trend of SG's outputs with respect to the correspondent loads. We calculated also the condition number and the matrix of cross sensitivities coefficients (cfr§2.2.2).

To validate the consistency of the obtained compliance matrix [C], we calculated the residual calibration errors for each applied load. We applied a known vector \vec{F} on the model (using the appropriate module on Abaqus[®] 6.9), we obtained the simulated strain outputs and using Eq.(2) we calculated the vector $\hat{\vec{F}}$.

In this way we could compute the absolute error between the vector \vec{F} applied on the model and $\hat{\vec{F}}$ and the percentage error as shown below:

$$\%Error = \left(\frac{\vec{F} - \hat{\vec{F}}}{\vec{F}} \right) \cdot 100 \quad (7)$$

To evaluate the accuracy of our measurement system, during the simulation analyses we applied on the model a force vector \vec{F} with known components (but different from those applied during the virtual calibration procedure) and we computed the resulting errors (results are shown in §3.1.1).

2.2.3. Experimental setup

For intra-operatory measurements we went to the neurosurgery department of “Istituto Clinico Humanitas” (Rozzano, MI, Italy); the neurosurgical intervention was performed by Professor Lorenzo Bello. The SGs were bounded on the positioning system the day before the intervention, while the experimental calibration has been carried out after the surgical operation. The experimental setup and technical specifications of the instrumentation we used were described in a protocol that was approved by the scientific and ethical commission of the clinical institute before the intra-operatory measurement; the risk analysis was also carried out.

Data about forces and moments acting on the Mayfield and about head's position, velocity and acceleration were acquired during a surgical removal of a left frontal lobe ganglioglioma (type III) on a patient of 41 years that weights 84 kg. The intervention lasted ~6 hours. In order to correlate the events occurred during the intervention with our force's and moment's signals we noted the phases and the events that characterized the surgical procedure (see Appendix I) choosing as time reference the operating room's clock.

We used two element 90° tee rosettes strain gauges for flexion and torque measurements (Vishay[®] Precision Group) (*Fig. 14*).

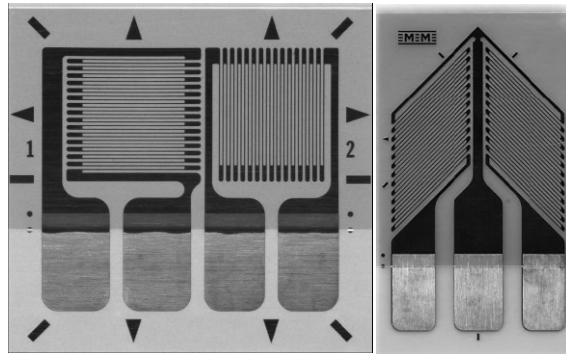


Fig. 14: two element 90° tee rosettes for flexion (on the left) and torque (on the right) measurements.

The elements of the SG are connected through an half bridge circuit (*Fig. 15*), where each resistance is sensible to strain along directions perpendicular to each other.

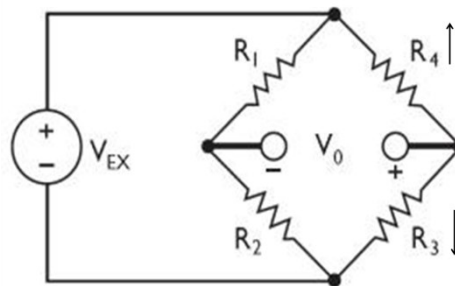


Fig. 15: Wheatstone bridge configuration: R_3 and R_4 are the resistances composing our double SGs. R_1 and R_2 are not sensible to the strains.

We can consider the following relationship:

$$\frac{\Delta V_0}{V_{ex}} = \frac{G}{4}(\varepsilon_1 - \varepsilon_2) \quad (8)$$

where V_0 is the output voltage, V_{ex} the excitation voltage, G is the Gauge factor, ε_1 and ε_2 are the strains along perpendicular directions.

Using this configuration thermal effects are theoretically compensated; also remote sense wires were connected directly to the bridge resistors in order to allow our acquisition system to sense the actual bridge voltage and eliminate the gain errors caused by the resistance of the excitation leads.

Technical specifications of SGs are shown in *Tab. 1*:

Tab. 1: technical specifications of SGs.

Resistance	Strain range	Temperature range	Exposed solder tab area	Grid dimensions
350 $\Omega \pm 0.4\%$	$\pm 5\%$	-100° to +350°F [-75° to +175°C]	3.3x2.0 mm (T) 2.6x1.8 mm (F)	4.75x3.81 mm (T) 3.18x4.19 mm (F)

Signal were acquired using NI Compact DAQ and NI 9237 Bridge Module (National Instruments®) shown in *Fig. 16*.

Technical specifications are shown in *Tab. 2* :

Tab. 2: technical specifications of NI Compact DAQ and NI 9237 Bridge Module.

Resolution	Maximum sampling rate	Internal excitation	Connection	Power supply
24 bits	50 kS/s	up to 10 V	USB connection	12 V battery



Fig. 16: NI 9237 Bridge Module (on the left) and NI Compact DAQ (on the right).

The final experimental setup is represented in *Fig. 17*. The bridge module was connected to a notebook (used for graphical interface and data storage) with an USB interface. The system-user interface (*Fig. 18*) was created using the software Labview[®] 2011 (National Instruments[®]). The DAQ module and the notebook were battery powered (12 V) for electrical security reasons.

During our measures we set the excitation voltage to 5V and the sampling rate to 1613 Hz (minimum sample frequency for NI 9237 Bridge Module).

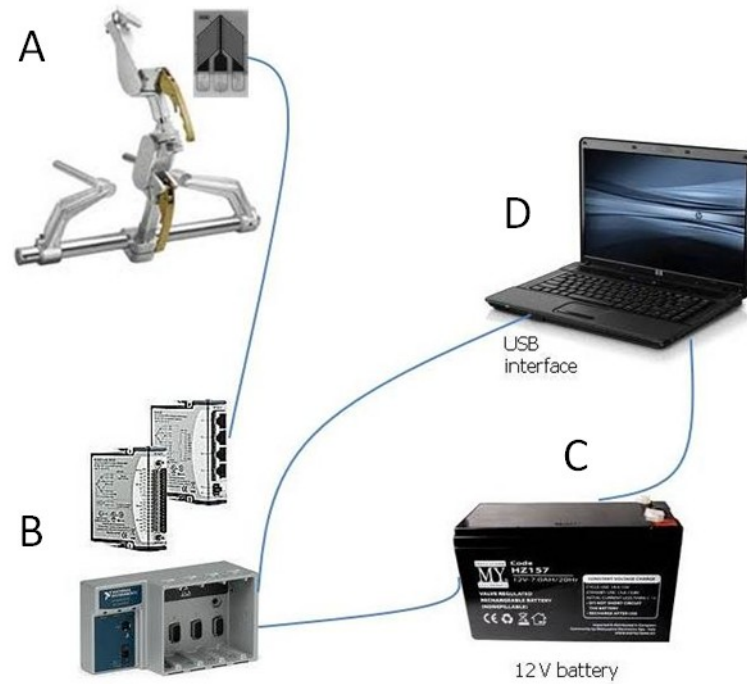


Fig. 17: representation of experimental setup for signal acquisition (strain gauges (A), Bridge Modules (B), battery (C) and notebook (D)).

The final operating room situation is represented in *Fig. 18* where the wires (yellow circle) that connect the SGs (red circles) with the Bridge Modules are shown. We can see the Mayfield positioning system connected to the surgical bed and the SGs attached in the positions represented in *Fig. 13*.

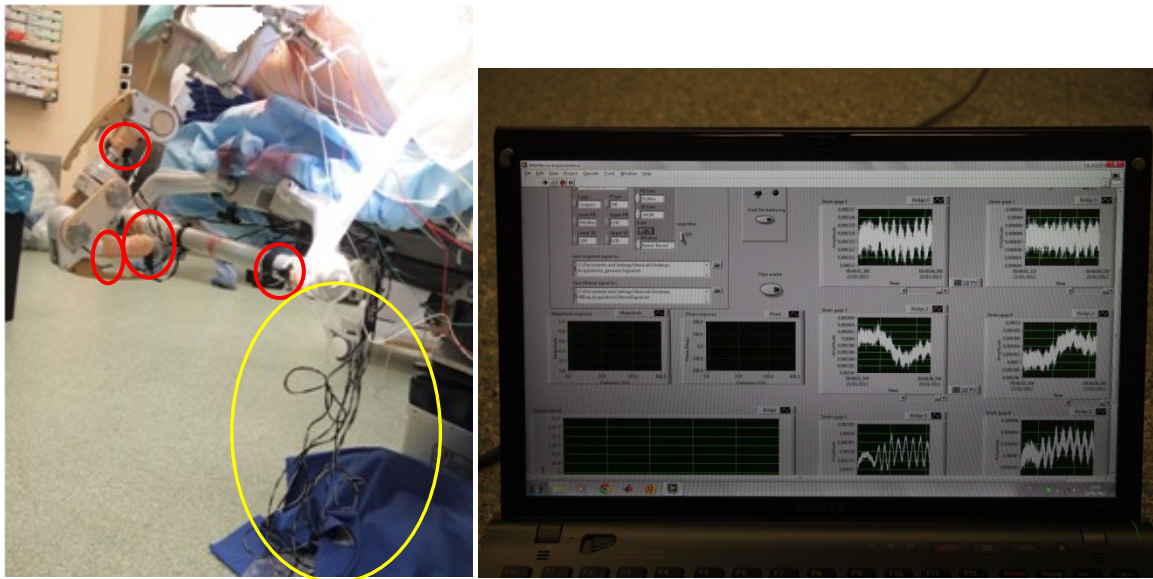


Fig. 18: On the left Mayfield clamp, SG (red circle) and wires that connect SG and DAQ (yellow circle). On the right an image of the user interface during the signal acquisition.

In *Fig. 19* we show the patient's head attached to skull clamp and we can observe the relative position between the positioning system and the head-neck segment.



Fig. 19: patient's head attached to the skull clamp immediately before the intervention.

2.2.4. Experimental calibration procedure

The calibration was done after the intervention, with the clamp already attached to the bed and without modifying the configuration of the arms. The SG signals' offset was acquired for about 5 minutes without any load applied on the structure. Forces and moments were applied using a system of weights and pulleys and an arm attached to the pin on the terminal part of the clamp.

During the experimental calibration procedure each applied load in each direction was applied twice; between each load application an offset signal without weights applied on the structure was acquired.

The second weight application was done in order to be able to compare the results obtained with two measures and in order to have backup data in case of errors in load's application; also an eventual hysteresis in the mechanical behavior of the structure could be detected.

Each application of loads along each direction was characterized by the following steps:

- Offset signal acquisition
- Application of load (first weight's application)
- SGs output acquisition
- Offset signal acquisition
- Application of the same load (second weight's application)
- SGs output acquisition

The same applies for all loads in all directions; in order to calculate the coefficients of the strain compliance matrix, we subtracted the offset (the one acquired immediately before the load's application) to the SGs' outputs. In this way we avoided errors due to possible drifts of the sensors' offsets during the calibration and we subtracted the force along the gravity direction due to the weight of the arm used for moments' application.

The loads applied for force and moments along each direction can be found in *Tab. 3* (only in the case of force along x direction we applied 5 loads):

Tab. 3: loads applied during experimental calibration

COMPONENTS	LOADS APPLIED				
Force x [N]	5	15	25	45	55
Force y [N]	5	15	20	35	
Force z [N]	5	15	20	35	
Moment x [Nm]	0.8	2.5	3	5.5	
Moment y [Nm]	0.8	2.5	3	5.5	
Moment z [Nm]	-0.8	-2.25	-3	-5	

REFERENCE FRAME DETERMINATION

Fig. 20 shows the reference frame that we chose to represent forces and moments: x axis is the gravity force direction.

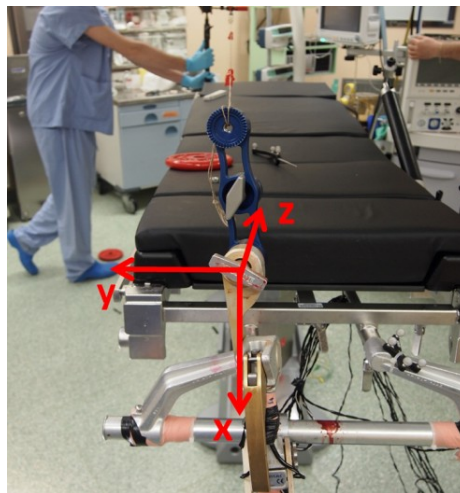


Fig. 20: reference frame representation.

The perpendicularity between the z and the x direction was ensured through the use of a bubble level (red circle in *Fig. 22*); the same applies for the perpendicularity between y and x axes. To ensure a square angle between y and z direction we used a set square.

APPLICATION OF FORCES

The force along x direction was applied by connecting directly weights to the pinion as shown in *Fig. 21*.



Fig. 21: application of force along x direction.

Forces along z and y directions were applied through a pulley in the way shown in *Fig. 22*.

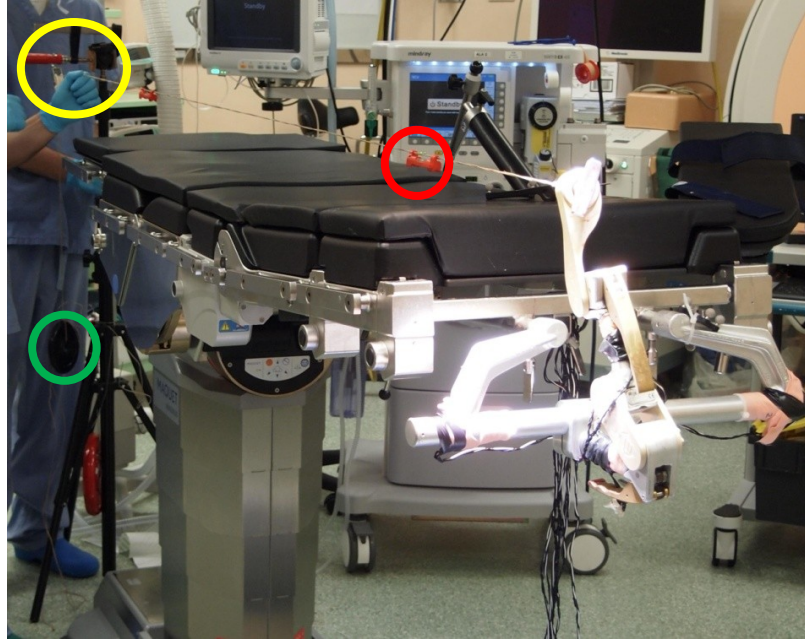


Fig. 22: example of application of a force along z direction. The red circle highlights a bubble level, the yellow one the pulley, while the green circle highlights the weight applied.

APPLICATION OF MOMENTS

The moments were applied using an arm attached to the pinion of the positioning system. For the moment around y direction we attached the arm vertically and then we applied a force along z direction (*Fig. 23*). The perpendicularity to x direction was assured by a bubble level. Similarly, for the moment around x direction we attached the arm horizontally and we apply a force along z axis. To apply the moment around z direction we maintained the arm horizontal and we applied weights (along gravity force direction) on its terminal part.

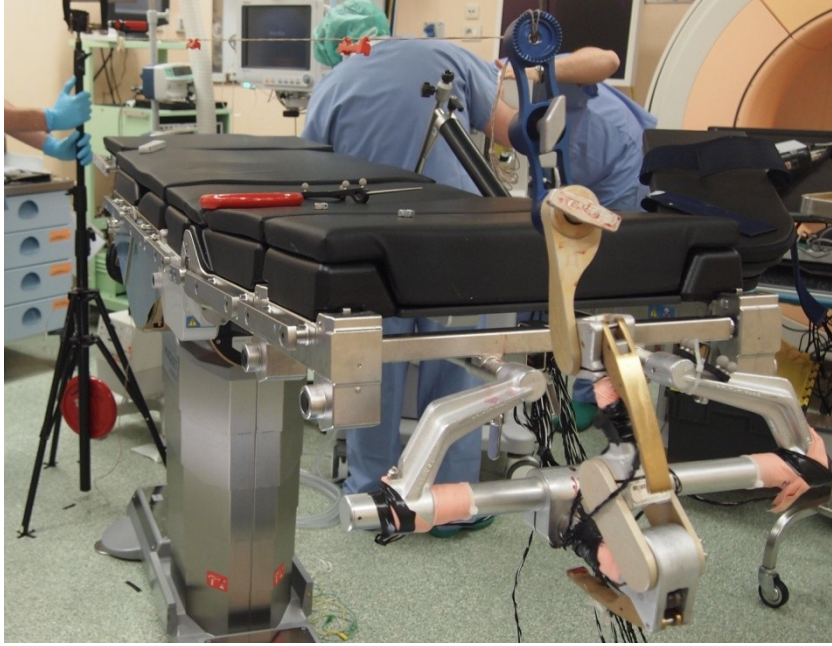


Fig. 23: Application of the moment around y direction: we can see the blue arm attached to the terminal pin of the clamp.

The applied moment is computed knowing the measure of the arm and the applied weight as:

$$\vec{M} = \vec{F} \times \vec{b} = |\vec{F}| \cdot |\vec{b}| \cdot \sin \alpha \quad (9)$$

where \vec{F} is the force vector, \vec{b} is the position vector of the point of application of force relative to the terminal pin of the positioning system and α is the angle between \vec{F} and \vec{b} directions (see *Fig. 24*).

We measured α using the optical system described in 2.2.3. In particular we acquired the position of the point of application of force and the position of the terminal pin, thus reconstructing the vector \vec{b} . We acquired also the position of 300 points of vector \vec{F} and we reconstructed it through a linear regression. The angle α was calculated as the angle between the two vectors in the plane identified by \vec{F} and \vec{b} .

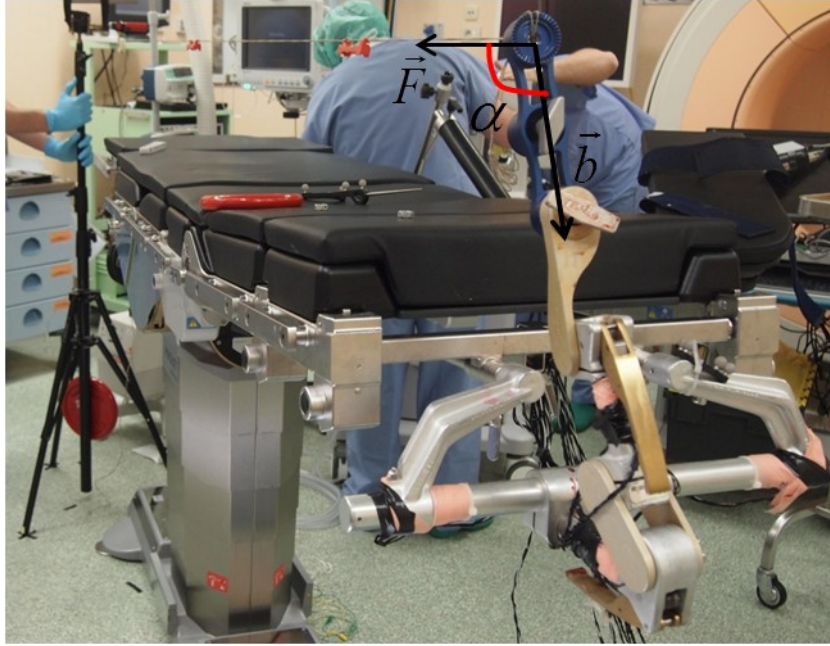


Fig. 24: representation of vectors \vec{F} , \vec{b} and angle α .

Since we were not applying a couple of forces, the resultant moment was not pure. In order to solve this problem, we considered a force (with magnitude and direction equal to that used for the moment application) exerted on the pinion of the positioning system (point of application of forces) by subtracting its contribute to the SG's voltage output.

STRAINS COMPLIANCE MATRIX COMPUTATION

The strain compliance matrix coefficients were calculated as angular coefficients of the regression line that fits our set of data (see §3.1.2).

In order to test the consistency of our linear fitting we calculated the coefficient of determination R^2 of the linear model as specified in (10) and results are reported in *Tab. 6*.

$$R^2 = \frac{\sum_{i=1}^n (\hat{y}_i - \bar{y})^2}{\sum_{i=1}^n (y_i - \bar{y})^2} \quad (10)$$

\hat{y}_i represent the SG's outputs predicted by our linear model, while y_i are the observed values; \bar{y} is the mean value of SG's output.

We computed the residual calibration error for both the strain compliance matrices calculated using data from the first weight's application and using data from the second weight's application (the results obtained in the case of first weight's application are reported in *Tab. 7*).

2.2.5. Signal processing

The acquired data were processed and visualized using the MATLAB[®] (Mathworks[®], *Nantick, MA*, USA) software.

Since the useful frequency content of our signal was all in the range 0÷10 Hz, in order to reduce our amount of data we performed a decimation operation.

In order to avoid aliasing, data were filtered with an 8th order Chebyshev Type I low-pass filter with cutoff frequency 20.2 Hz, before resampling. We resampled our signal with a sample frequency of 50.4 Hz. The input sequence was filtered in both the forward and reverse directions to remove all phase distortion, effectively doubling the filter order.

In order to further remove the signals' noise we filtered the decimated signal with a 29th order FIR equiripple filter characterized by the following parameters:

- Cut-off frequency: 12 Hz
- Pass-band ripple: 0.001 dB
- Stop-band attenuation: 80dB

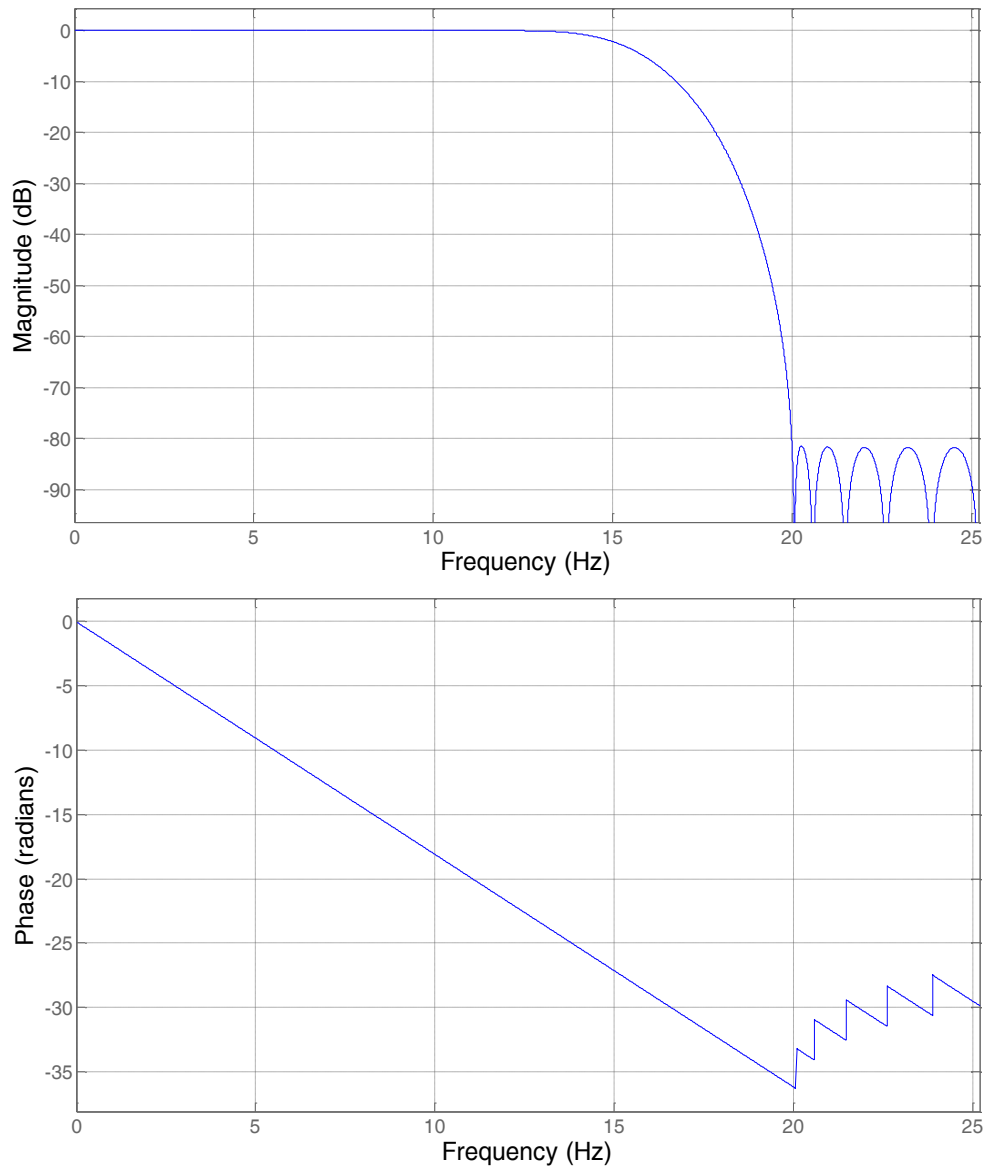


Fig. 25: magnitude and phase response of the equiripple filter that we used.

The SG's output signals ('filtered signals') were characterized by a slow trend (219 N/h) (in particular during the first part of the intervention) (*Fig. 26*).

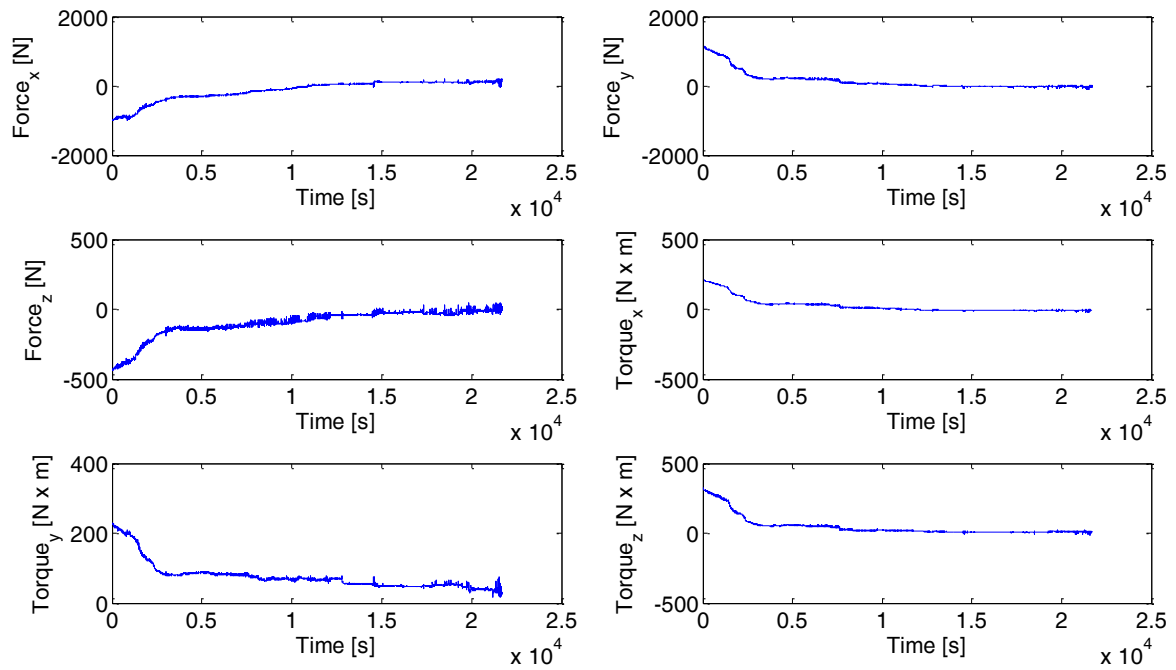


Fig. 26: Forces and moments signals during the entire intervention (results obtained without the detrending procedure)

Since we were interested in measuring the value of forces and moments without considering this trend (cfr §4.2) we chose to remove it.

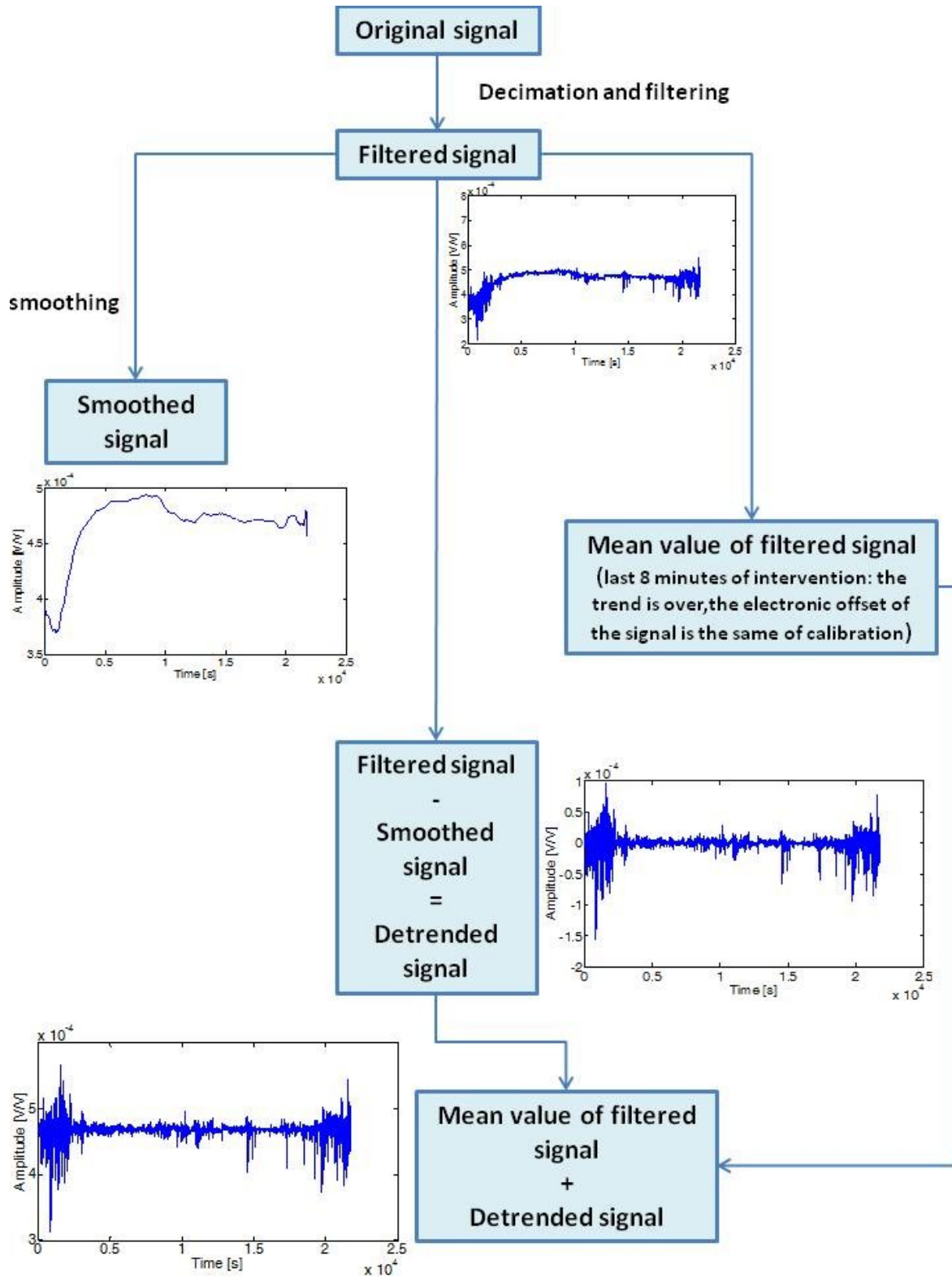


Fig. 27: schematization of the detrending procedure

We used the Matlab function ‘*smooth*’ that computes a moving average of the input signal on 40000 samples and we obtained the ‘smoothed signal’ (Fig. 33). Then, we subtracted in each temporal instant the value of the smoothed signal to the filtered one obtaining the ‘detrended signal’ (Fig. 34).

Finally, we calculated the mean values of the filtered signals in the last part of the intervention (that did not show the trend) and we add this value to the ‘detrended signals’ in each temporal instant. We did it in order to have the final signal’s base line around the same values of the filtered signal’s base line in the last temporal window of the surgical operation (Fig. 35).

2.2.6. Moment and forces measurements

In order to have a value of strain gauge output equal to zero when no loads are applied on the clamp, we subtracted to all the output signals of SGs their offset value. The values of forces and moments during each temporal instant of the intervention were calculated as explained in (2): results are shown in *Tab. 17* (Appendix I). During these analyses we were not interested in considering the total load applied on the clamp, but only the contribution due to forces exerted by the patient or by the medical staff. In fact we subtracted in each temporal instant of the intervention the static loads’ values determined by the weight of the head of the patient (usually around 8% of body weight), by a part of the weight of his shoulders and neck and by the weight of the c-clamp (1.350 kg).

The value of this static load contribution was calculated using SG’s output signal acquired during the first temporal segment of the intervention: in that moment the head was fixed to clamp, the patient was asleep and nobody was touching him (results are shown in *Tab. 9*).

2.2.7. Frequency domain analyses

In order to observe the frequency content of our load's signals we calculated the **Discrete Fourier Transform (DFT)** for each component of force and moment in each segment of the surgical intervention. Plotting the single-sided amplitude spectrum, we could qualitatively observe the range of frequency content distinguishable from the noise and the possible presence of peaks.

Finally, we analyzed how the frequency content varies over time by calculating the **Short Time Fourier Transform (STFT)** of signals. Using STFT analysis and plotting the spectrogram of the signals (*Fig. 54*) we associated the study of the signal in the time domain (loads applied during particular phase of the intervention) and its behavior in frequency domain.

In the case of 3D graphs reported in *Fig. 54* the signal segment has 1765 samples and the STFT was computed by dividing the signal in segments of 300 samples (using an Hamming window), with an overlap between the segments of 150 samples; the DFT was calculated in 300 sampling points. The result of analyses in frequency domain are shown in §3.1.6

2.3. Head's velocity and accelerations measurements

In this paragraph we show the experimental setup used for head's displacements, velocity and acceleration measurements; we describe also the computation of velocity and acceleration starting from tool's position data.

2.3.1. Experimental setup

We measured position, velocity and acceleration of the head during the surgical intervention, using the optical tracking system Polaris Vicra[®] (Northern Digital Inc., Canada) (red arrow in *Fig. 20*). It is an optical sensor that detects and measures the 3D position of passive markers (i.e. retro-reflective markers that reflect infrared light, emitted by illuminators on the position sensor). Using this information the sensor is able to determine the location and orientation of the application-specific tool where the markers are attached.

The accuracy of the system is 0.25 mm and the frequency of acquisition is 20 Hz.

In *Fig. 28* is represented the measurement volume that is the space region in which markers can be tracked.

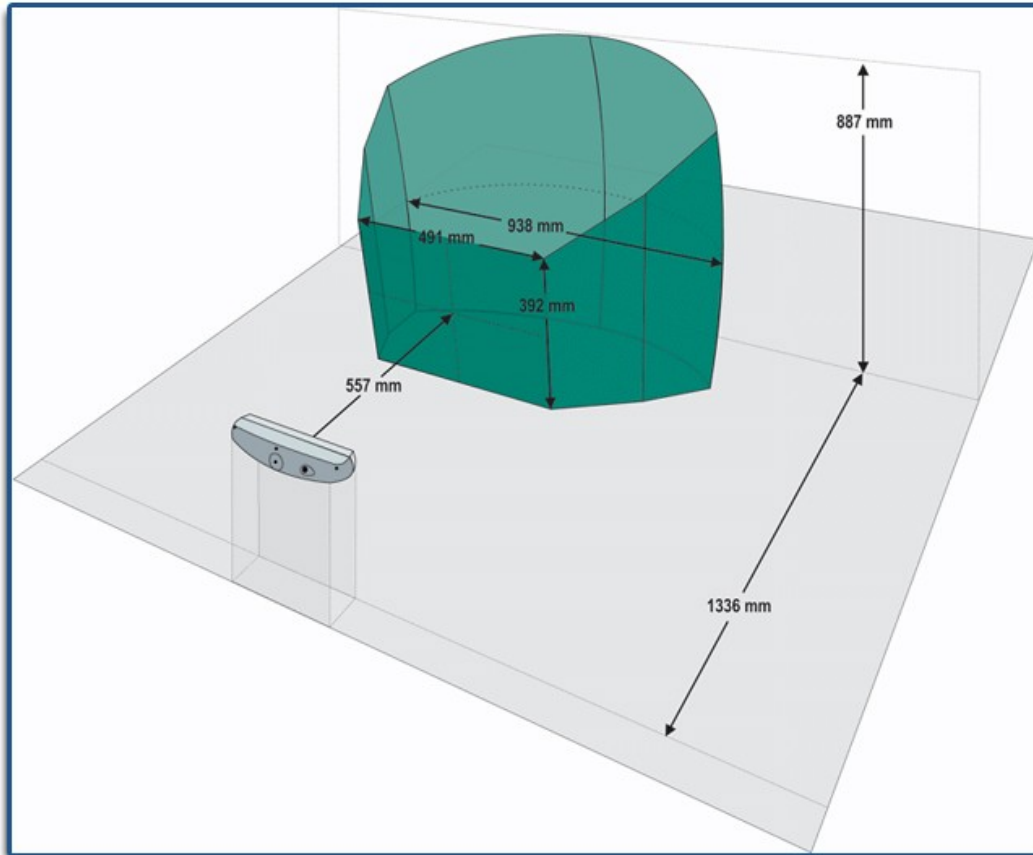


Fig. 28: Polaris Vicra[®] measurement volume.

To measure head's position and to calculate its velocity and acceleration during the surgical intervention we tracked the position of a tool (blue circle in *Fig. 29*) attached to the skull clamp. The experimental set-up is represented in *Fig. 29*.

Knowing the position of the tool in each temporal instant, we computed velocities and accelerations (assuming the head solidal with the skull clamp).

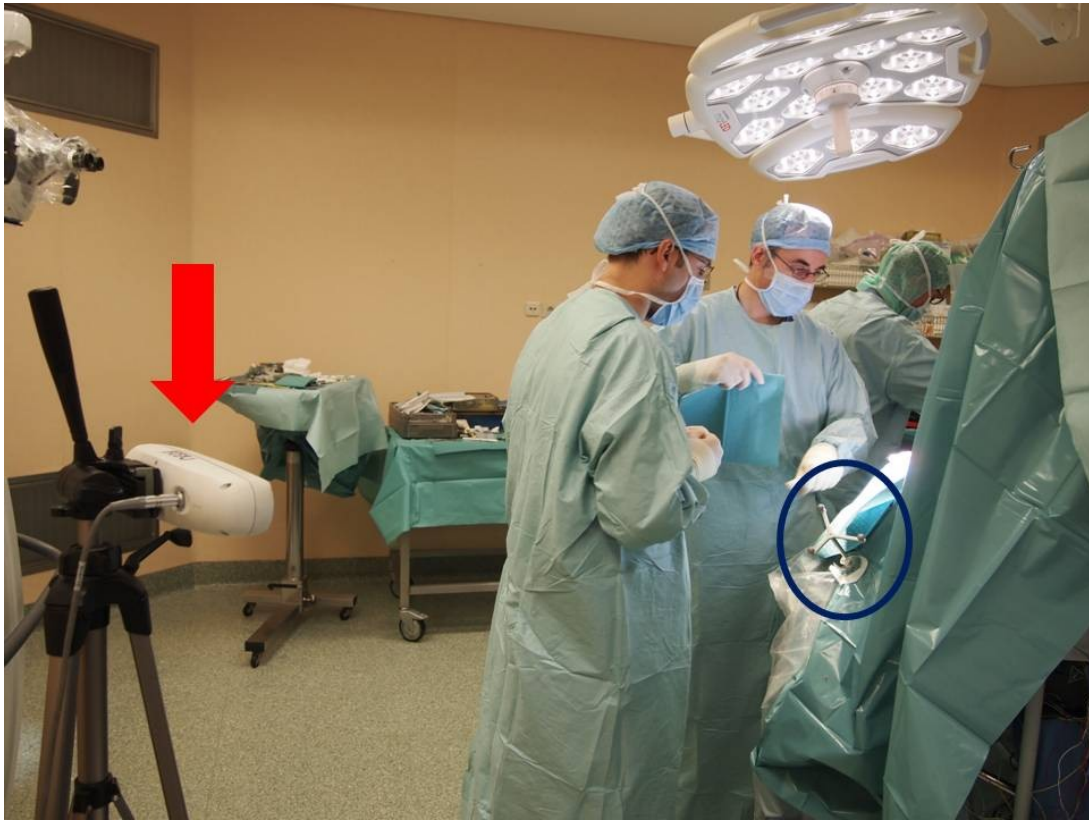


Fig. 29: Representation of the experimental setup: the red arrow indicates the Polaris Vicra[®], while the blue circle highlights the tool attached to the C-clamp.

2.3.2. Tool's definition

Since the tool used to track the head's position was not provided by Northern Digital Inc., before the intervention we had to characterize the application specific tool where the markers were attached.

During the process of characterization a file that describes each feature of the tool is created in order to provide Polaris Vicra[®] with the tool's dimensions and marker placements. We defined a local tool's reference frame determining the position of each marker with respect to this reference frame.

Thanks to the tool characterization the optical system was able to recognize the tool connected to the positioning system (when the passive markers were in its measurement

volume). Using the information about markers' locations on the tool the Polaris Vicra[®] provides the position vector and rotation of the tool's local reference frame with respect to its reference frame.

2.3.3. Signal processing

We calculated the head displacement in each temporal instant as specified in (11) for the example of x direction:

$$\Delta x(t) = \bar{x} - x(t) \quad (11)$$

where $\Delta x(t)$ is the displacement in x direction at the time instant t , \bar{x} is the mean value of the x component of the tool's position vector with respect to the optical system reference frame during the event we considered and $x(t)$ is the value of the x component of the tool's position vector with respect to the optical reference frame at the time instant t .

The module of the displacement in each temporal instant $d(t)$ is calculated as the vector sum of the displacements along the three directions of the space (12):

$$d(t) = \sqrt{\Delta x(t)^2 + \Delta y(t)^2 + \Delta z(t)^2} \quad (12)$$

We calculated also the velocity using a centered finite difference method on 2 samples. In this case the example of velocity along x direction is:

$$v_x(t) = \frac{x(t+1) - x(t-1)}{2t_s} \quad (13)$$

In each temporal instant the module of the velocity vector was calculated as shown in (14):

$$|\vec{v}| = \sqrt{v_x^2 + v_y^2 + v_z^2} \quad (14)$$

We calculated also the accelerations using the same formulas and replacing the position vector of the tool with its velocity vector. In (15) the example for x direction:

$$a_x(t) = \frac{v_x(t+1) - v_x(t-1)}{2t_s} \quad (15)$$

In each temporal instant the module of the acceleration vector is (16) :

$$|\vec{a}| = \sqrt{a_x^2 + a_y^2 + a_z^2} \quad (16)$$

As in the cases of forces and moments we divided the events into 4 types and we calculated for each type the maximum value, and quartiles of displacement's, velocity's and acceleration's distributions.

As in the case of forces and moments (cfr §2.2.7) DFT of displacements, velocity and acceleration signals were calculated in order to qualitatively evaluate their frequency content.

Chapter 3

3. Results

3.1. Forces and moments measurements

In the following paragraphs we show the results obtained forces and moments measurements both in simulation and on-field.

3.1.1. Simulation results

We show the results obtained with the configuration similar to that used during the surgical intervention. *Fig. 30* shows the linear relationship between loads applied and SG voltage output during simulation analysis. On the following graph loads applied [N] are represented on abscissa and the voltage outputs [V/V] are on ordinate. The red line is the least square regression line that fits our set of data. We illustrate only the example of the graphs obtained in the case of SG 5 for the three components of force and moment.

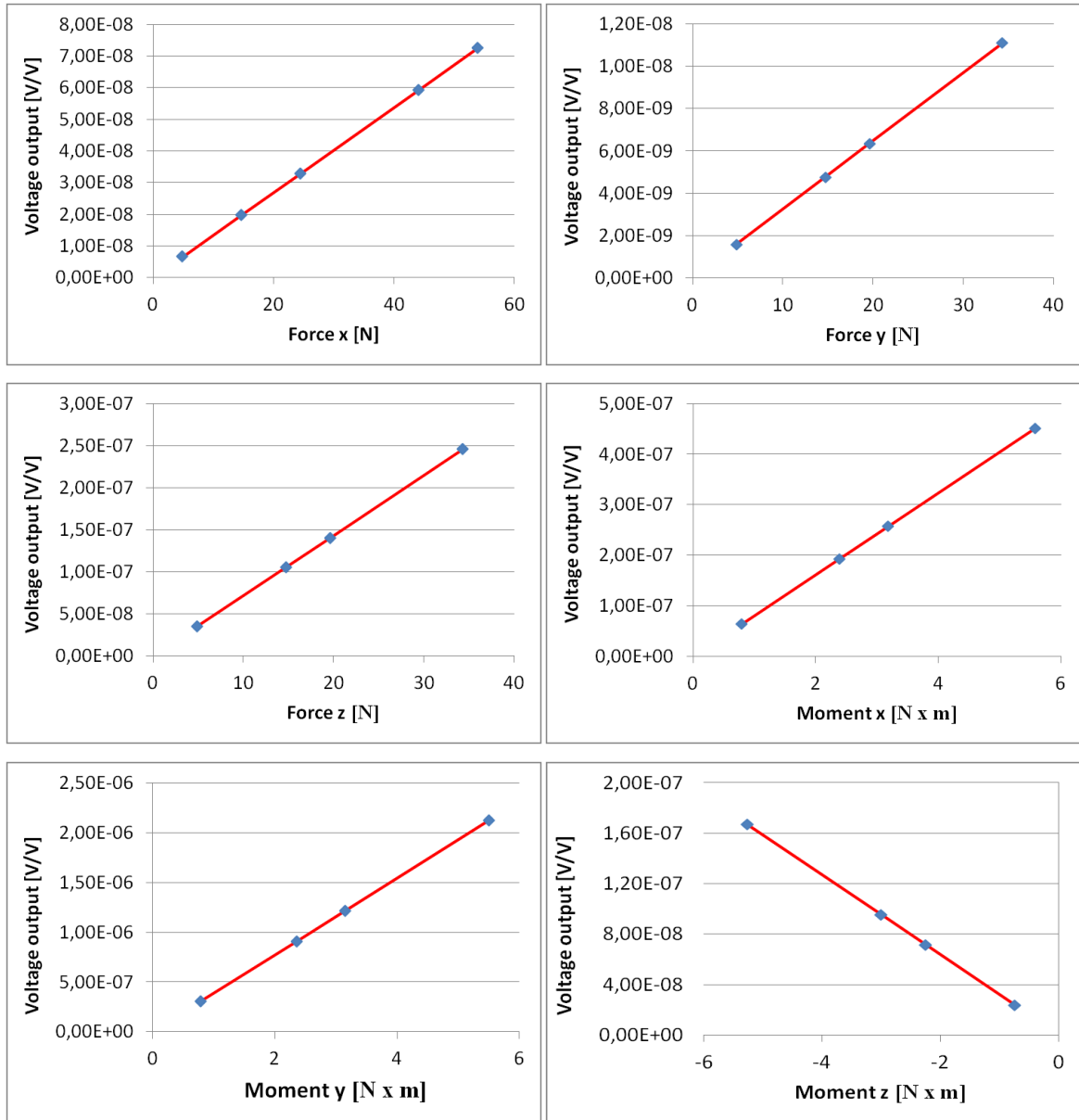


Fig. 30: Relationship between voltage output [V/V] of SG5 and force's and moment's components obtained in simulated calibration.

The coefficients of the strain compliance matrix $[C]$ obtained during simulation tests were calculated as explained in §2.2.2.

This is the strain compliance matrix obtained in simulation analyses:

$$[C] = \begin{bmatrix} 1,19E-07 & -3,7E-09 & -7,2E-08 & -4,3E-07 & -1,5E-07 & -6,99E-07 \\ 3,93E-07 & -2,1E-07 & -2,4E-07 & -7,786E-07 & -5,7E-08 & -1,3E-06 \\ -1,7E-07 & 1,03E-07 & -2,9E-08 & 3,04E-08 & 2,14E-07 & 5,93E-07 \\ 1,34E-09 & 3,24E-10 & 7,17E-09 & 8,07E-08 & 3,852E-07 & -3,17E-08 \\ -1,6E-07 & -1E-07 & -1,9E-08 & 1,91E-08 & -3,8E-07 & -6E-07 \\ 9,76E-09 & -2,9E-10 & -2,3E-05 & 2,74E-07 & 8,37E-08 & -3,9E-08 \end{bmatrix}$$

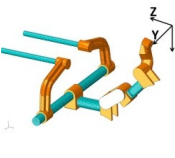
The condition number for this matrix resulted 269.8966.

This is the matrix of the Cross-Sensitivity coefficients [CS] (cfr §2.2) for the strain compliance matrix obtained in simulation:

$$[CS] = \begin{bmatrix} -9,66E-02 & 3,02E-03 & 5,85E-02 & 3,47E-01 & 1,21E-01 & 5,67E-01 \\ -1,77E-01 & 9,64E-02 & 1,06E-01 & 3,50E-01 & 2,57E-02 & 5,99E-01 \\ -2,22E-01 & 1,38E-01 & -3,83E-02 & 4,07E-02 & 2,86E-01 & 7,95E-01 \\ 3,04E-03 & 7,31E-04 & 1,62E-02 & 1,82E-01 & 8,69E-01 & -7,17E-02 \\ 1,28E-01 & 8,20E-02 & 1,50E-02 & -1,54E-02 & 3,08E-01 & 4,83E-01 \\ -4,32E-04 & 1,29E-05 & 1,01E+00 & -1,21E-02 & -3,71E-03 & 1,76E-03 \end{bmatrix}$$

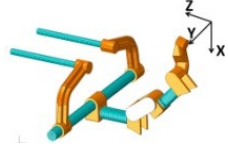
In the table below (*Tab. 4*) we report the calibration residual error (cfr §2.2.2) obtained in simulation analyses. For each load applied the absolute and the percentage error are reported. Greatest errors were found in the case of moments around x direction (1.5×10^{-3} Nm)

Tab. 4: calibration residual error for simulation analyses. From left to right we find respectively the load applied, the percentage error and the absolute error.

	Load [N]	Error %	Absolute error [N]		Load [Nm]	Error %	Absolute error [Nm]
Force x	5	3,30E-07	1,62E-08	Moment x	0,8	5,28E-02	4,21E-04
	15	1,31E-04	1,93E-05		2,5	6,38E-02	-1,52E-03
	25	1,74E-05	4,28E-06		3	4,41E-02	-1,41E-03
	45	7,95E-06	3,51E-06		5,5	1,37E-02	7,64E-04
	55	9,03E-06	-4,87E-06				
Force y	5	3,39E-04	1,66E-05	Moment y	0,8	5,84E-05	4,60E-07
	15	7,30E-05	1,07E-05		2,5	3,42E-05	8,08E-07
	20	5,94E-05	1,17E-05		3	3,74E-05	1,18E-06
	35	5,45E-05	-1,87E-05		5,5	2,09E-04	1,15E-05
Force z	5	1,06E-04	5,20E-06	Moment z	-0,8	2,59E-04	1,95E-06
	15	1,06E-04	1,56E-05		-2.5	2,86E-05	6,45E-07
	20	1,06E-04	2,08E-05		-3	8,04E-06	2,42E-07
	35	2,00E-05	6,88E-06		-5	1,96E-05	1,03E-06

In *Tab. 5* we report the results obtained in two simulation tests, where values of forces and moments, different from those used in calibration and inside the expected range, considering the anthropometric data, were applied (cfr §2.2.2):

Tab. 5: results obtained in simulation test. From left to right we find respectively the applied load, the percentage error and the absolute error. In black the results of the first simulation test and in red those of the second test.

	Load	Error %	Absolute error
Force x [N]	0.03	0.0162	0.000049
	0.04	10	0.0041
Force y [N]	4	0.0047	0.0002
	28	0.0008	0.0002
Force z [N]	-52	0.0005	0.0002
	106	0.0038	0.0041
Moment x [Nxm]	21.2	0.0052	0.0011
	0.12	0.9891	0.0012
Moment y [Nxm]	0.25	0.0163	0.00004
	2.05	0.0073	0.0001
Moment z [Nxm]	-1.01	0.0151	0.0002
	79	0.0142	0.0113

Errors are always less than 1% unless in the case of force along x axis in the second test. The load applied in this case is only 0.04 N.

3.1.2. Experimental results

In *Fig. 31* the relationship between the loads applied (x-axis) during the experimental calibration procedure (cfr §0) and SGs voltage output (y-axis) is shown. The red line is the least square regression line that fits our set of data.

Similar to the simulation case (cfr §3.1.1), we show only the example of results obtained for SG 5.

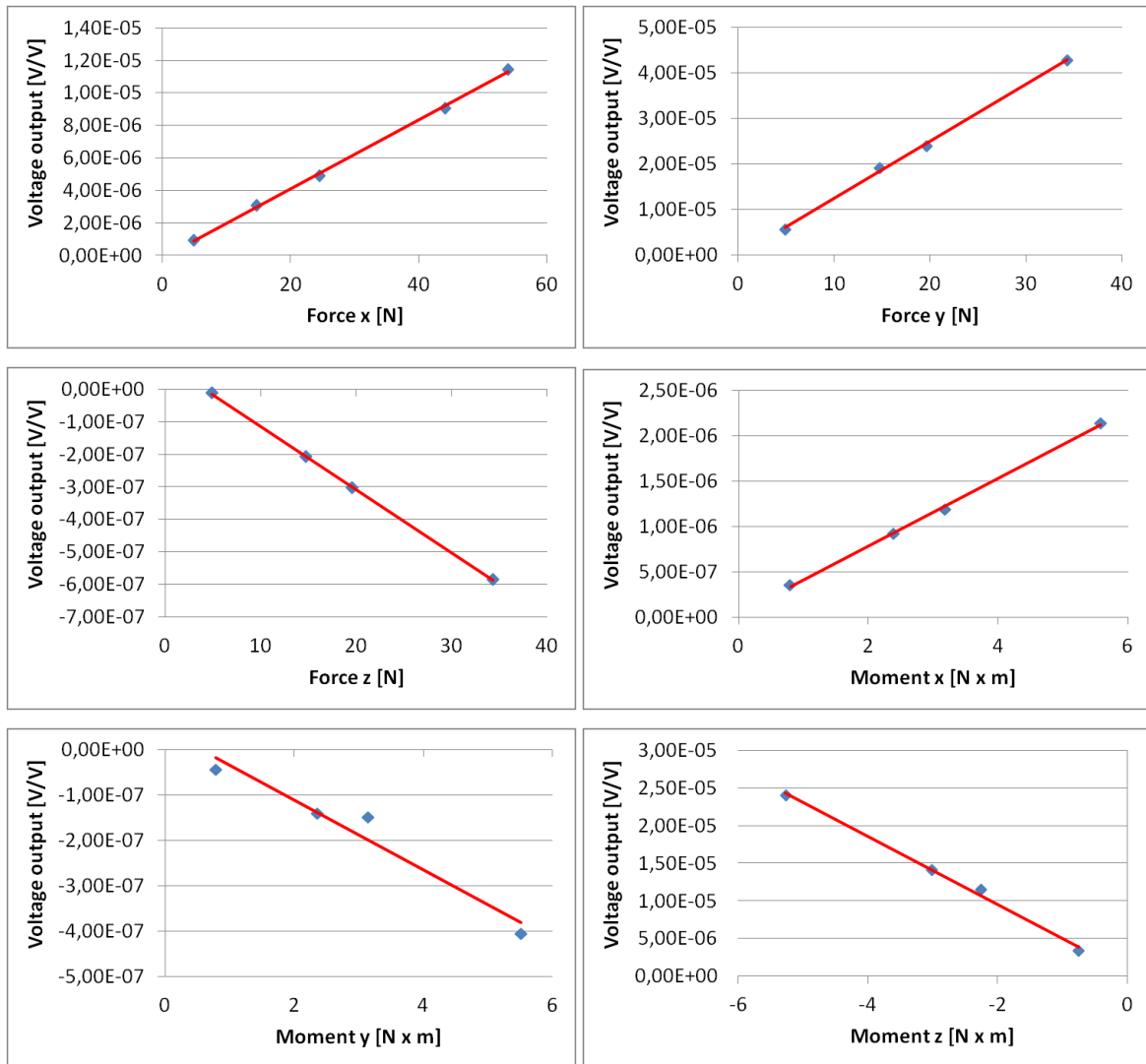


Fig. 31: relationship between voltage output [V/V] of SG5 and force's and moment's components obtained in experimental calibration.

As we can see, in the real case, the relationship between forces (or moments) and SG outputs was almost linear. In *Tab. 6* we illustrate the coefficients of determination of the linear model that correlates SG output and the loads applied on the three force and moment components. The correlation coefficient is calculated as specified in (10).

Tab. 6: coefficients of determination of the linear model that correlates SG outputs and load applied. The critical cases with $R^2 < 0.7$ are highlighted in red.

	SG1	SG2	SG3	SG4	SG5	SG6
Force x	0,9842	0,9812	0,9988	0,9971	0,9989	0,9014
Force y	0,9959	0,9991	0,9988	0,9985	0,9978	0,9990
Force z	0,9972	0,9986	0,9994	0,9946	0,9998	0,9841
Moment x	0,7637	0,6067	0,7369	0,9985	0,9784	0,9962
Moment y	0,5595	0,7603	0,9833	0,9476	0,0367	0,9783
Moment z	0,9953	0,9789	0,9930	0,9949	0,9954	0,4850

There are only three critical cases with $R^2 < 0.7$ (highlighted in red in *Tab. 6*); two of them are in the case of moments applied around y-axis.

The compliance matrix $[C]$ obtained with the experimental calibration:

$$[C] = \begin{bmatrix} -7,5E-07 & 7,11E-07 & 5,2E-06 & 4,26E-06 & 6,96E-06 & -5,6E-06 \\ 5,26E-07 & 4,98E-07 & 1,62E-06 & 2,88E-06 & 1,04E-05 & -6,5E-06 \\ 1,64E-06 & -1,7E-06 & 1,32E-05 & 5,77E-06 & 4,08E-05 & -2,6E-06 \\ 2,07E-06 & 1,23E-05 & -1,9E-07 & 3,67E-06 & -7,5E-07 & -4,4E-05 \\ 9,33E-08 & -1,6E-06 & 6,33E-07 & 2,59E-05 & 2,17E-07 & -1,1E-05 \\ -2,6E-07 & 2,1E-06 & -3,2E-06 & -3,8E-05 & -8,7E-06 & 3,34E-07 \end{bmatrix}$$

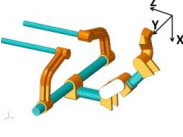
The condition number for this matrix was 86.293.

This is the matrix of the Cross-Sensitivity coefficients [CS] (cfr §2.2) for the strain compliance matrix obtained with the experimental calibration:

$$[CS] = \begin{bmatrix} -6,96E-02 & 6,57E-02 & 4,80E-01 & 3,94E-01 & 6,43E-01 & -5,14E-01 \\ 5,59E-02 & 5,29E-02 & 1,72E-01 & 3,06E-01 & 1,10E+00 & -6,88E-01 \\ 2,87E-02 & -3,03E-02 & 2,32E-01 & 1,01E-01 & 7,14E-01 & -4,52E-02 \\ -7,62E-02 & -4,51E-01 & 7,01E-03 & -1,35E-01 & 2,76E-02 & 1,63E+00 \\ 6,38E-03 & -1,09E-01 & 4,33E-02 & 1,77E+00 & 1,48E-02 & -7,30E-01 \\ 5,53E-03 & -4,38E-02 & 6,69E-02 & 7,97E-01 & 1,82E-01 & -6,98E-03 \end{bmatrix}$$

In *Tab. 7* below we report the calibration residual error (cfr §2.2.2) obtained in the experimental calibration. For each load applied the absolute and the percentage error between the load applied and our estimation (the calculation procedure is specified in §2.2.2) is reported.

Tab. 7: residual error for experimental calibration. From left to right we find respectively the load applied, the percentage error and the absolute error.

	Load [N]	Error %	Absolute error [N]		Load [Nm]	Error %	Absolute error [Nm]
Force x	5	3,48E+01	1,71E+00	Moment x	0,8	3,51E+01	2,79E-01
	15	3,70E+01	5,45E+00		2,5	2,30E+01	5,51E-01
	25	3,80E+01	9,32E+00		3	1,71E+01	5,44E-01
	45	1,46E+01	6,42E+00		5,5	5,77E+00	3,22E-01
	55	3,69E+00	1,99E+00				
Force y	5	8,31E+00	4,07E-01	Moment y	0,8	1,58E+02	1,24E+00
	15	5,69E+00	8,37E-01		2,5	1,82E+02	4,29E+00
	20	1,59E+00	3,12E-01		3	1,59E+02	5,01E+00
	35	3,71E-01	1,28E-01		5,5	3,09E+01	1,70E+00
Force z	5	4,67E+00	2,29E-01	Moment z	-0,8	1,46E+01	1,10E-01
	15	1,15E+01	1,69E+00		-2.5	2,08E+01	4,69E-01
	20	7,52E+00	1,47E+00		-3	1,16E+01	3,50E-01
	35	1,37E+00	4,71E-01		-5	2,74E+00	1,44E-01

Absolute errors are always less than 10 N for forces and 6 Nm for moments. In the case of moment around y-axis we found high percentage errors for lower loads.

3.1.3. Signal processing

In order to show the results of the signal processing procedure described in §2.2.5 we show results for the SG 5 output during the entire intervention. *Fig. 32* represents the signal before the detrending procedure, the smoothed signal (*Fig. 33*), the detrended signal (*Fig. 34*) and the final signal that we obtain after the processing (*Fig. 35*).

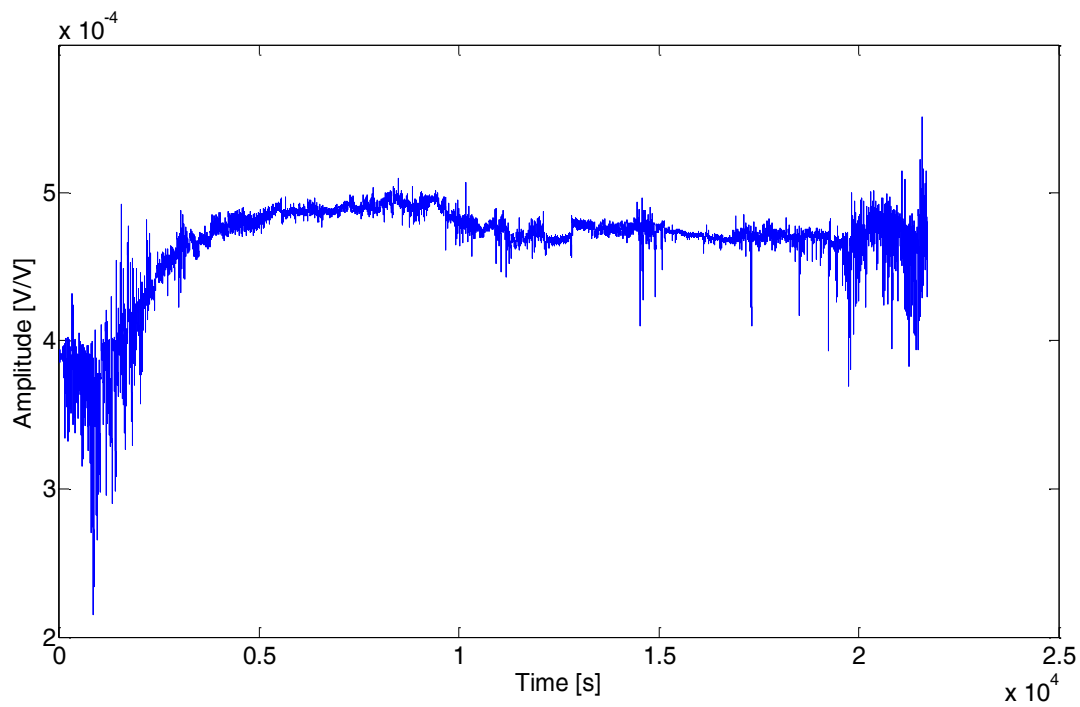


Fig. 32: SG 5 output during the entire intervention before the detrending procedure

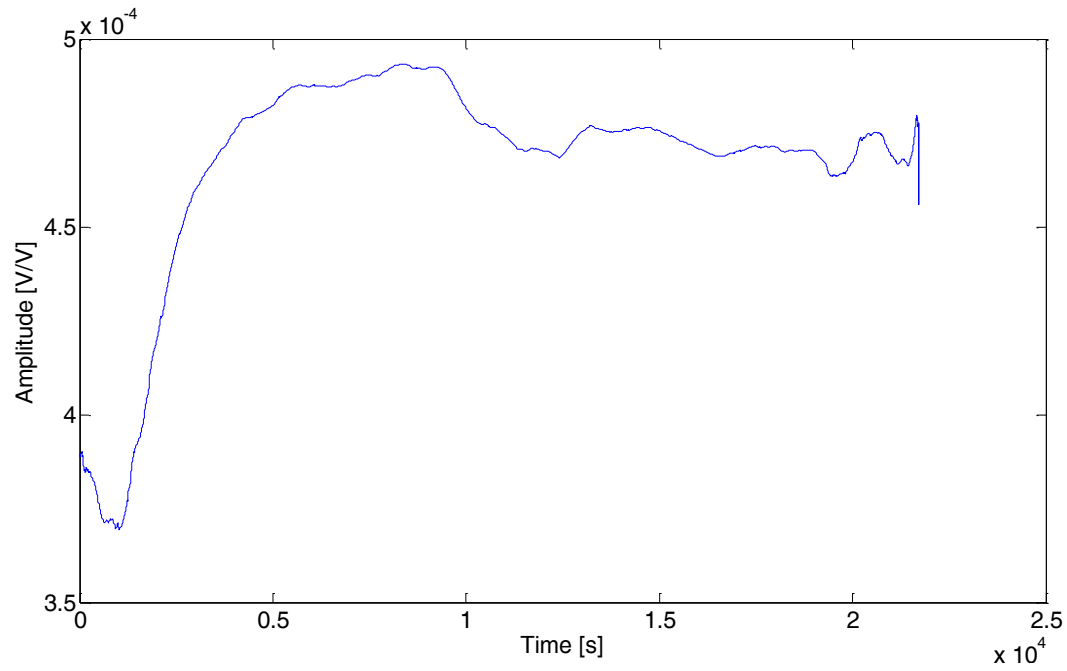


Fig. 33 SG 5 output during the entire intervention (smoothed signal)

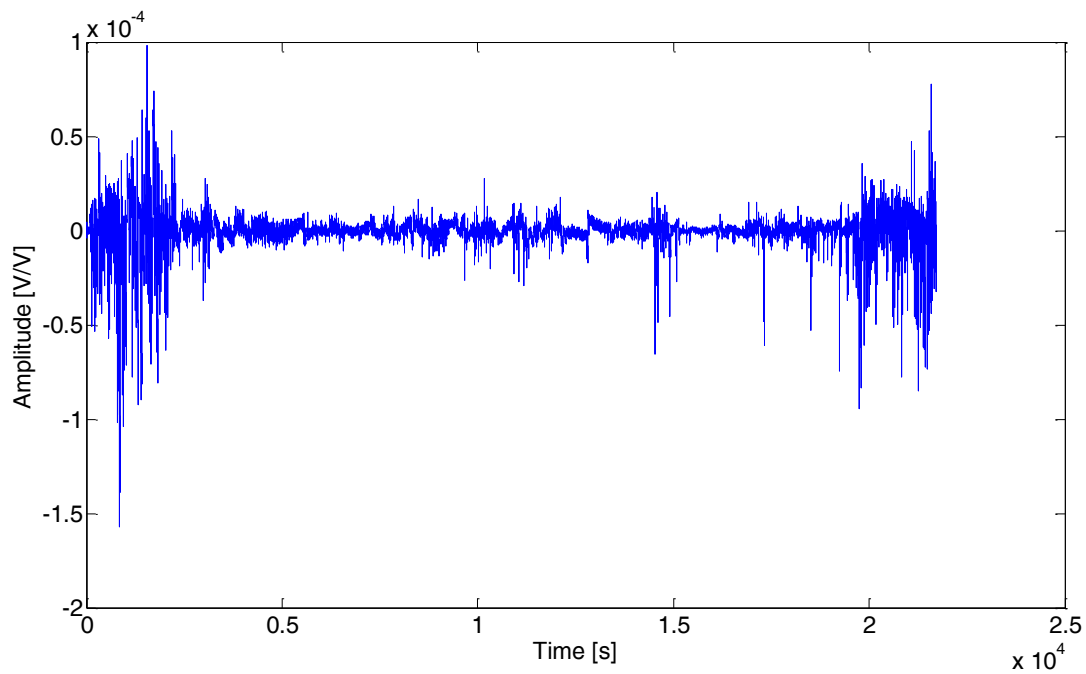


Fig. 34: SG 5 output during the entire intervention (detrended signal)

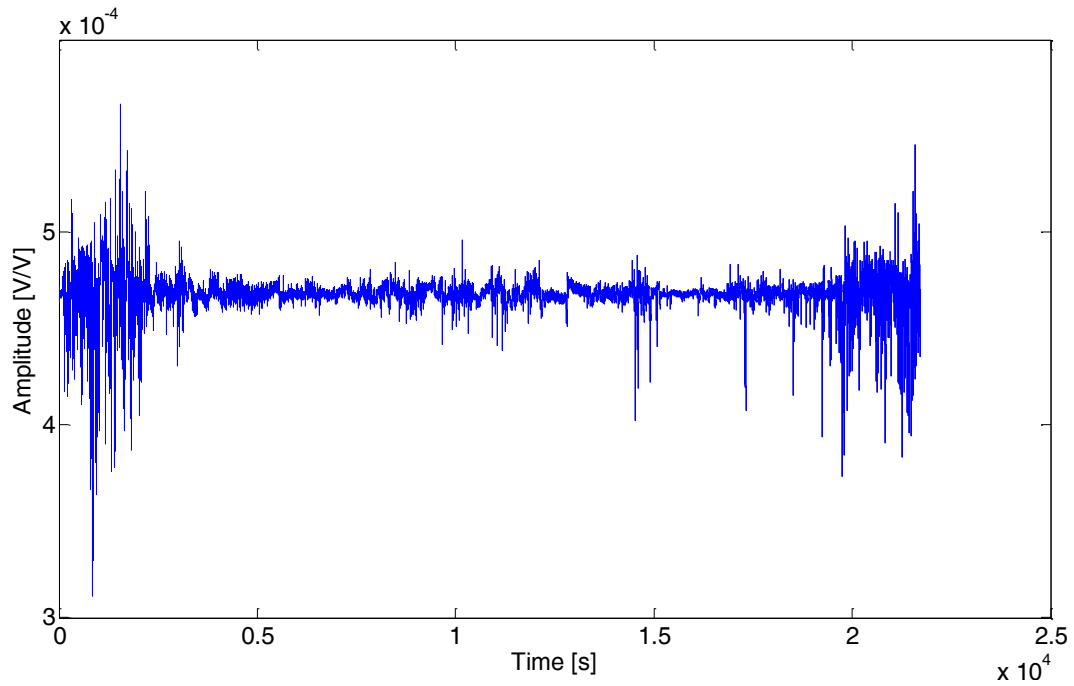


Fig. 35: SG 5 output during the entire intervention (final result after the signal processing)

We found greatest peaks during the first part (skull opening) and the last part (suturing) of the intervention.

3.1.4. Intra-operative measurements of forces and moments

All the events that occurred during the intervention can be classified in four. This classification was done in order to understand if forces' and moments' values depend on who is exerting loads (patient or surgeon) or on the type of patient's movement (unexpected or induced by stimulation). We chose the following classification:

- **Surgeon action:** events caused by the action of the surgeon or by the medical staff.
- **Patient stimulation induced movement:** patient's movements caused by electrical stimulation or requested by the medical staff.
- **Patient movement:** patient's movement (voluntary or involuntary) not requested by the medical staff
- **Accidental movements**

Each distribution of values of loads, displacements, velocities and accelerations was evaluated using Lilliefors test in order to discover if data come from a normally distributed population ($p < 0.05$). In order to compare the values of loads between each type of event, we performed a Kruskal-Wallis test comparing each distribution of forces and moments of each class with the distribution found for the other types' events. The same was done for displacement, velocity and acceleration measurements. The results of this statistical tests are reported in §3.1.5 and §**Errore. L'origine riferimento non è stata trovata.** In *Tab. 8* the maximum values of forces and moments during the entire intervention are summarized:

Tab. 8: maximum values of forces [N] and moments [Nm] during the entire intervention.

Force x [N]	Force y [N]	Force z [N]	Moment x [Nxm]	Moment y [Nxm]	Moment z [Nxm]
243,971	-114,695	65,558	-25,919	76,661	37,546

Values reported in *Tab. 8* include components of static forces and moments given by the head's and c-clamp's (cfr§2.1) weight (1,350Kg). As specified in §2.2.6, we estimated this contribution obtaining the following results (*Tab. 9*):

Tab. 9: contribution of static forces and moments given by the head's and c-clamp's weight.

Force x [N]	Force y [N]	Force z [N]	Moment x [Nxm]	Moment y [Nxm]	Moment z [Nxm]
138,908	-19,610	2,134	-7,003	34,497	11,180

As we expected, the maximum value is along the x direction, that is the gravity force direction.

Knowing the value of static components and by subtracting it to the value of forces and moments measured during each time instant, we can obtain the net contribution of forces and moments applied by the surgeon or by the patient (only with voluntary or involuntary movements).

3.1.5. Measurement analyses for events of different classes

In this section we show the study of distributions of load's values¹ for each type of event (cfr §3.1.4). Also, exemplary event signals are shown.

SURGEON ACTIONS

As an example of surgeon action, we chose the moment of skull opening. In this phase the surgeon was using the surgical drill. We selected a temporal segment 35 seconds long.

The following graphs (*Fig. 36*) show the time course of the corresponding estimated forces [N] and moments [Nm], computed from the SG outputs.

¹ The values of forces and moments that we present do not include the static load due to the weight of c-clamp and patient's head.

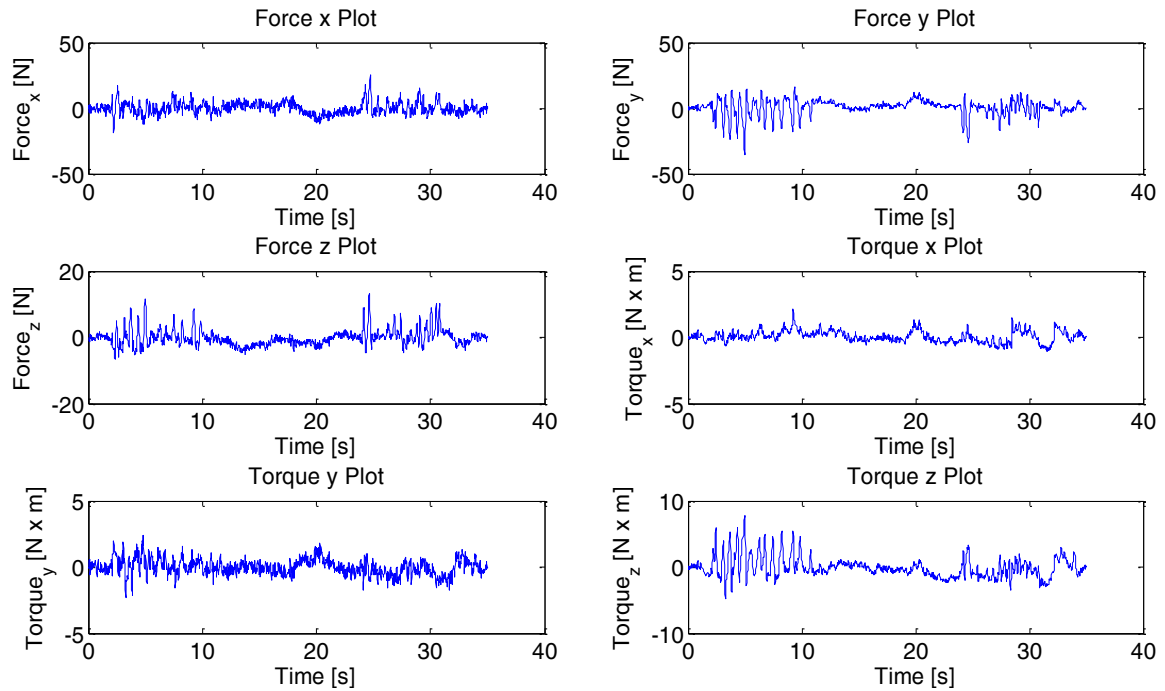


Fig. 36: forces and moments acting on the Mayfield[®] clamp positioning system during the example of surgeon action

It is interesting to observe the presence of peaks (-34N for force along y direction and 8Nm for moment around z direction) when the surgical drill is used (in the first part $[0-10\text{ sec.}]$ and the last part $[25-35\text{ sec.}]$ of the segment). Force along y direction and moment around z direction are the components with greater variations.

Fig. 37 illustrates the histograms of loads values' distribution for all the surgeon actions; the range between the minimum and the maximum is divided into 100 bins with same amplitude.

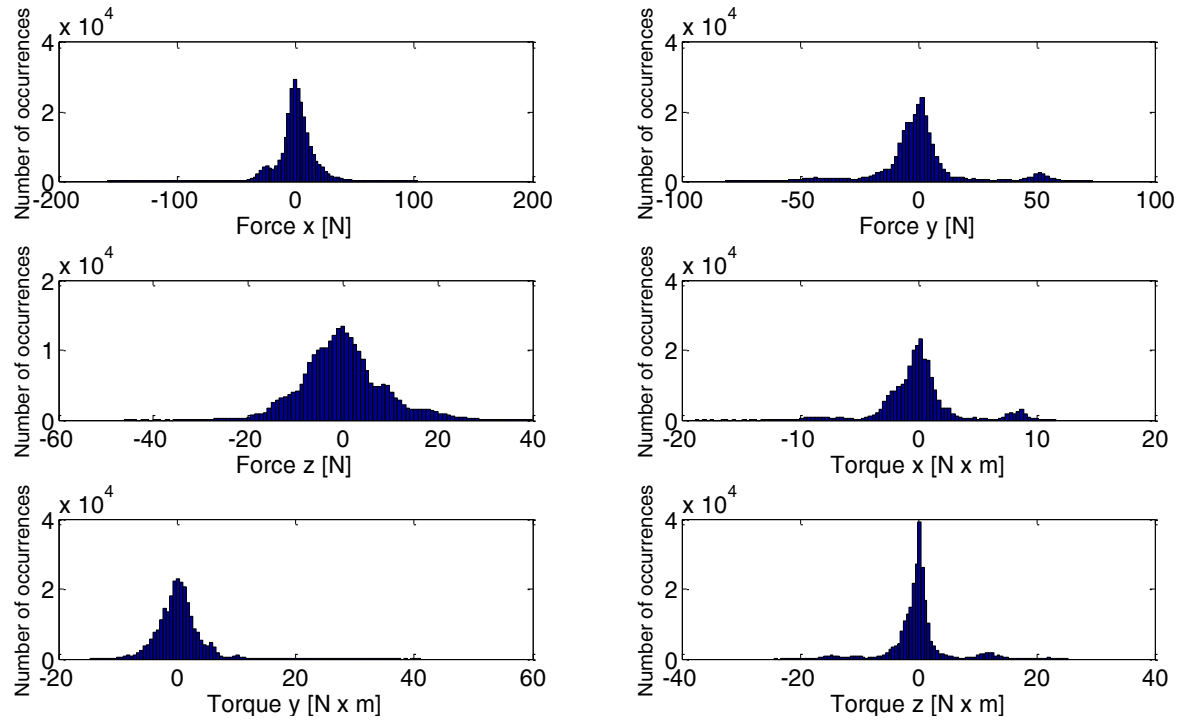


Fig. 37: histograms that represent the number of occurrences of load's values for the surgeon action.

Maximum and quartile values of these distributions are shown in *Tab. 10*. According to Lilliefors test data of the six components do not come from populations normally distributed at 0.05% significance level.

Tab. 10: results of statistical analyses of forces' and moments' values in each temporal instant for the surgeon actions; we report the maximum value², the median and the values of the 1st and 3rd quartile.

	Maximum value	1 st quartile	Median	3 rd quartile
Force x [N]	-158,329	-5,896	0,429	7,497
Force y [N]	-81,534	-6,089	-0,400	4,289
Force z [N]	-46,090	-5,401	-0,495	4,410
Moment x [Nxm]	-18,839	-1,335	-0,066	0,907
Moment y [Nxm]	41,125	-1,915	0,029	1,753
Moment z [Nxm]	25,235	-1,555	-0,046	0,928

² From now on with 'maximum value' we mean the value that has maximum modulus reported with its sign.

PATIENT STIMULATION INDUCED MOVEMENTS

Among stimulation induced movements we chose a temporal window during which the patient was asked to open and close his right hand (the duration time of the segment was 35 seconds). In *Fig. 38* the forces' and moments' signals are illustrated.

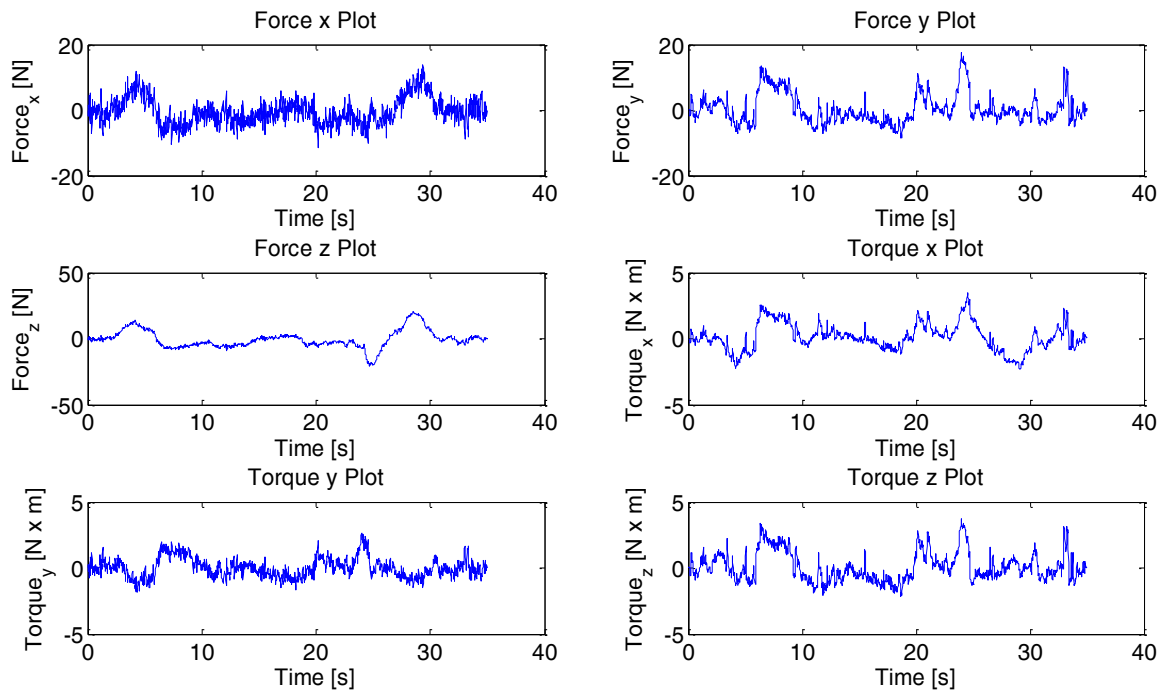


Fig. 38: forces and moments acting on the Mayfield® clamp positioning system during the example of stimulation induced movement.

In this case the range of signal's variation is the same in the three directions of the space (26N for forces and 6Nm for moments).

In *Fig. 39* the histogram that illustrates the load's distribution for stimulation induced movements.

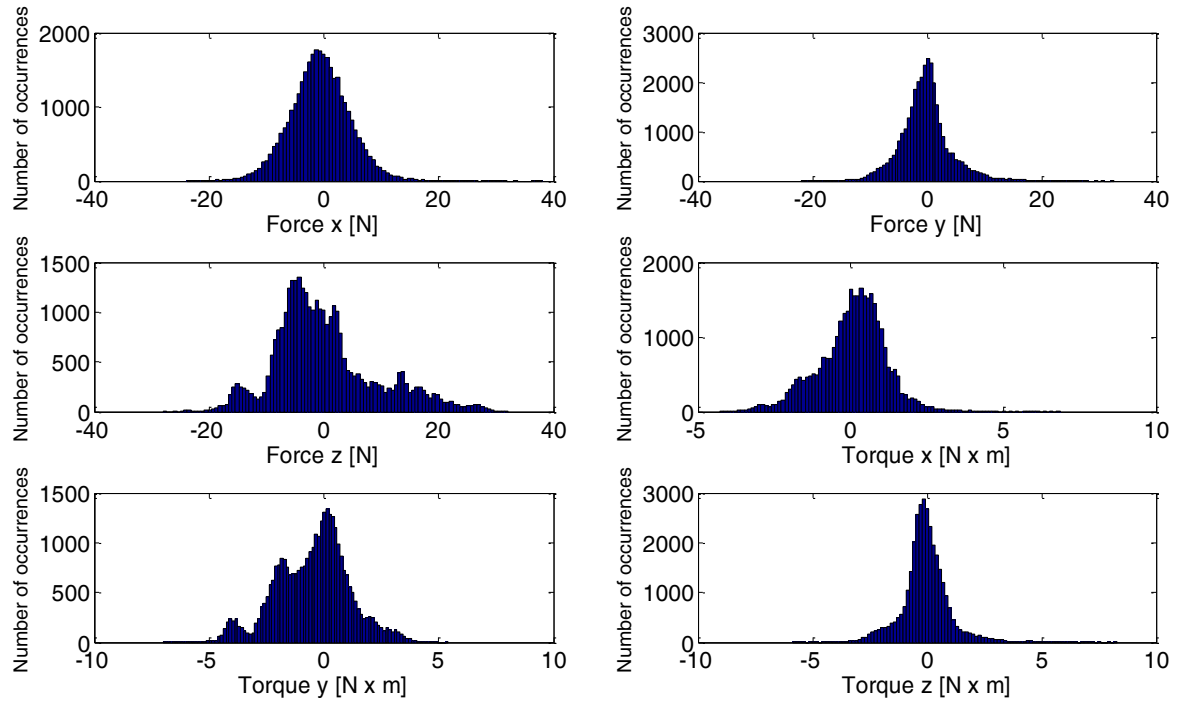


Fig. 39: histograms that represent the number of occurrences of load's values for stimulation induced movement.

In *Tab. 11* maximum and quartiles' values for distribution shown in *Fig. 39* are summarized. According to Lilliefors test data of the six components do not come from populations normally distributed at 0.05% significance level.

Tab. 11: results of statistical analyses of forces' and moments' values for stimulation induced movements.

	Maximum value	1st quartile	Median	3rd quartile
Force x [N]	8,216	-0,169	0,009	0,215
Force y [N]	-23,869	-3,943	-0,738	2,553
Force z [N]	-21,972	-2,667	-0,362	1,671
Moment x [Nxm]	32,104	-5,668	-1,520	3,865
Moment y [Nxm]	6,847	-0,555	0,156	0,750
Moment z [Nxm]	-6,994	-1,606	-0,310	0,531

PATIENT MOVEMENT

As example of patient movements we chose a large movement of the head of the patient (not requested by the medical staff). These are the force's and moment's signal for the time window that we considered.

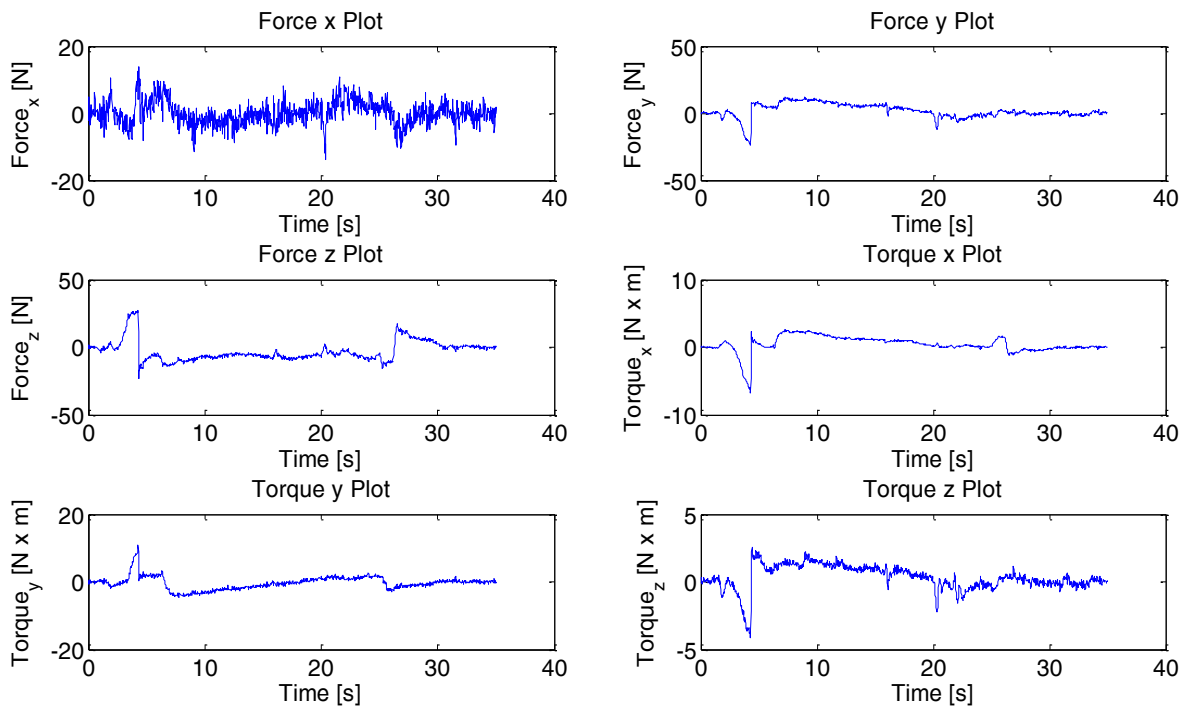


Fig. 40: forces and moments acting on the Mayfield® clamp positioning system during the example of patient movement.

We can observe the presence of a peak (maximum values of 40N for forces and 9Nm for moments) in the first ten seconds of the temporal window: in particular the force along z direction and the moment around y-axis are the major components.

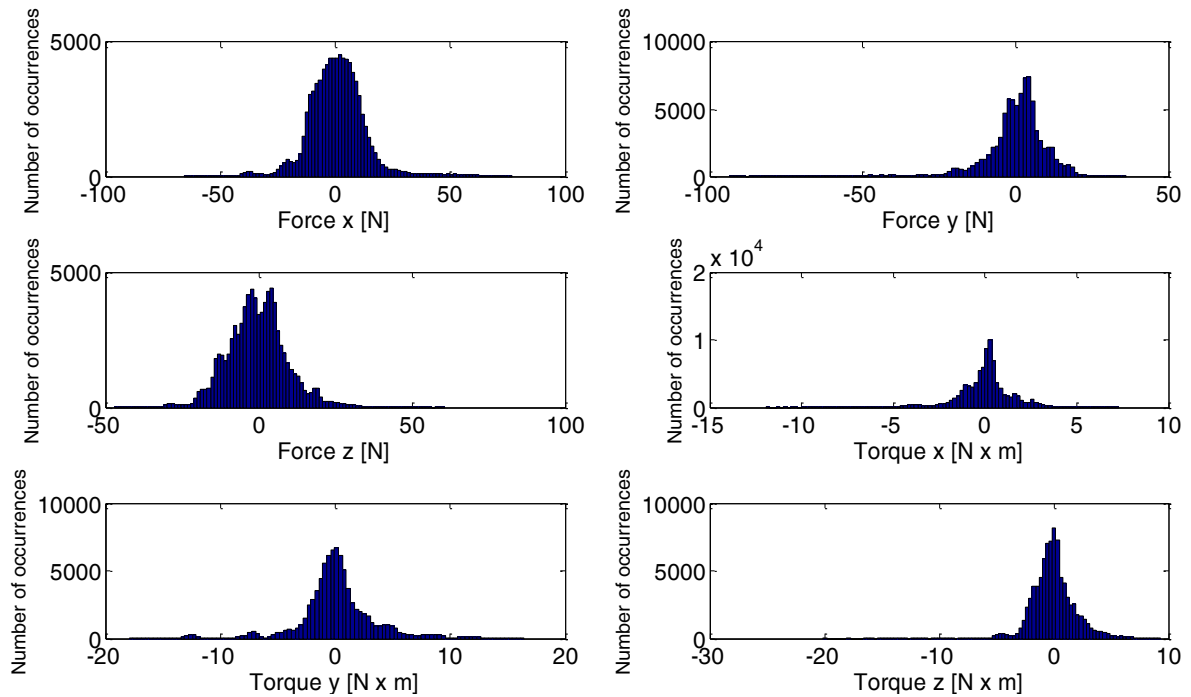


Fig. 41: histograms that represent the number of occurrences of load's values for patient movements.

In (Tab. 12) the results of analyses of loads' values distributions for patient movements. According to Lilliefors test, data of the six components do not come from populations normally distributed at 0.05% significance level.

Tab. 12: results of statistical analyses of forces' and moments' values for patient movements.

	Maximum value	1st quartile	Median	3rd quartile
Force x [N]	76,747	-6,502	0,687	7,576
Force y [N]	36,057	-3,372	1,552	5,409
Force z [N]	-46,968	-6,738	-0,665	5,161
Moment x [Nxm]	7,303	-0,644	0,118	0,607
Moment y [Nxm]	16,437	-1,256	-0,024	1,342
Moment z [Nxm]	9,293	-1,044	-0,104	0,870

ACCIDENTAL MOVEMENTS

As example of accidental movements, we will show the results of a temporal segment in which the right leg of the patient fall out off the surgical bed. As we can see from the graph in Fig. 42 this event is clearly visible in the first ten seconds of the temporal window that we considered.

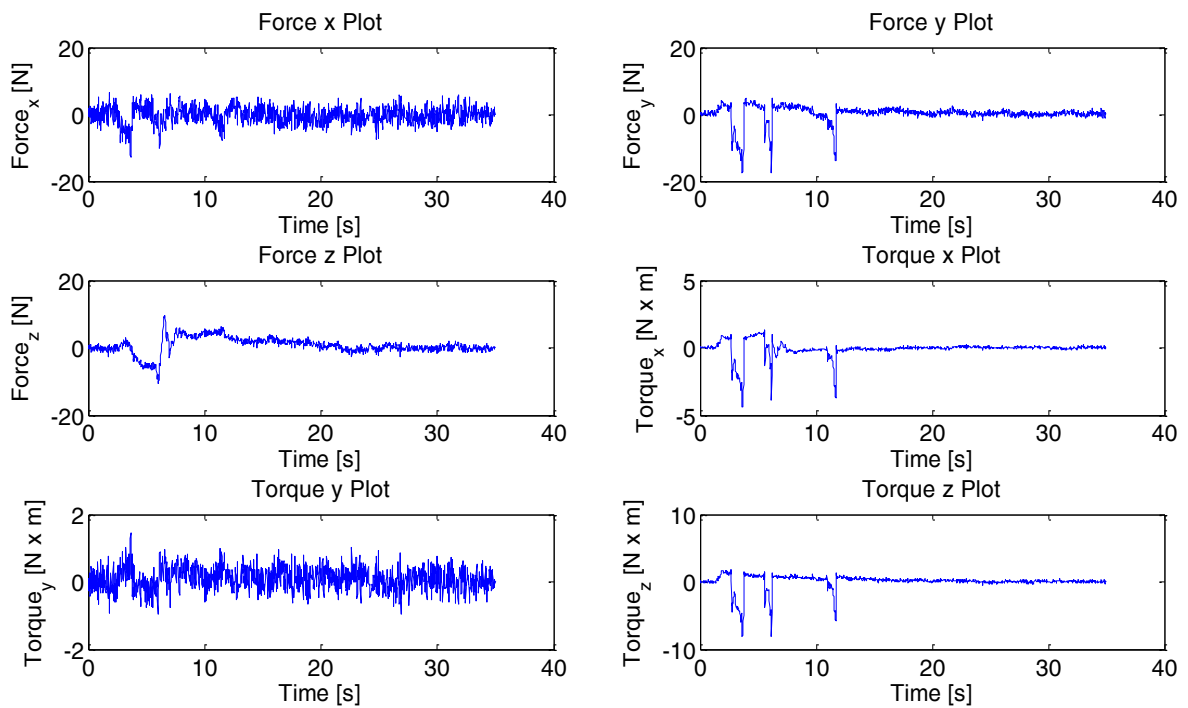


Fig. 42: forces and moments acting on the Mayfield® clamp positioning system during the example of accidental movement.

It's interesting to observe that the shape of the peaks due to the fall of the leg in the case of force x, force y, torque x and torque z is almost the same, but the values of these peaks are different (22N for force x and y, 5Nm for torque x and 9Nm for torque z).

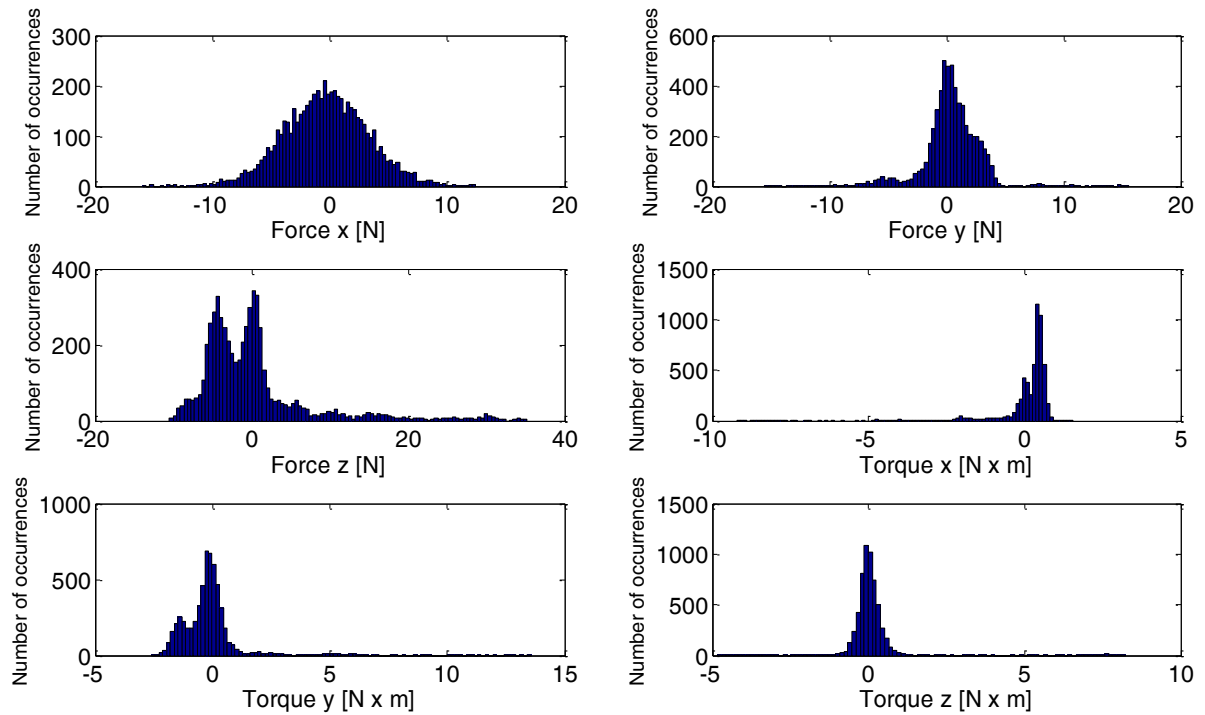


Fig. 43: histograms that represent the number of occurrences of load's values for accidental movements.

Executing Lilliefors test, we found a p-value greater than 0.05 only in the case of force along x direction ($p = 0.0844$).

Tab. 13: results of statistical analyses of forces' and moments' values in each temporal instant for accidental movements.

	Maximum value	1st quartile	Median	3rd quartile
Force x [N]	-15,905	-2,756	-0,323	2,075
Force y [N]	15,535	-0,607	0,382	1,607
Force z [N]	35,233	-4,251	-1,089	1,137
Moment x [Nxm]	1,552	0,017	0,383	0,512
Moment y [Nxm]	-2,600	-0,740	-0,208	0,155
Moment z [Nxm]	8,216	-0,169	0,009	0,215

The following histograms summarize the results obtained for load's measurements for the four type's events. Only absolute values of forces and moments are considered.

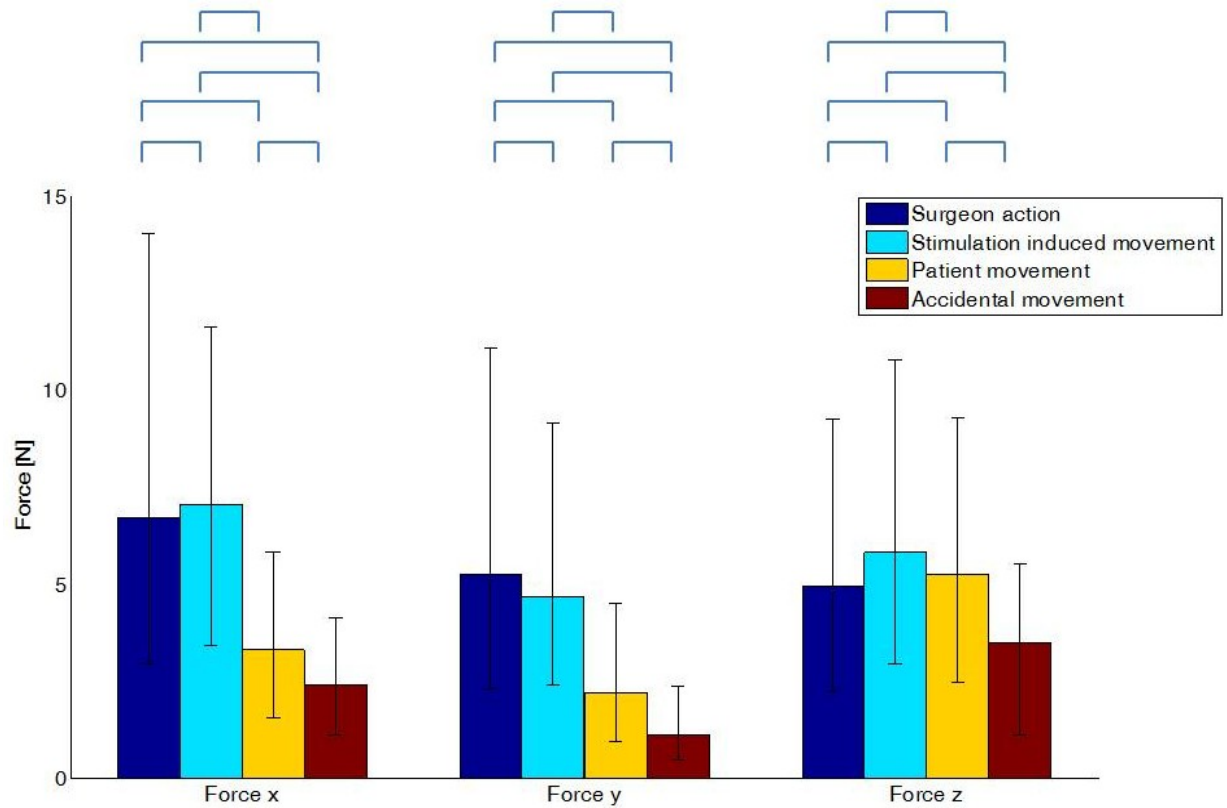


Fig. 44: summary of results obtained for force's measurements. The highness of the colored bars indicates the median value, while the black bars indicate the 1st and 3rd quartiles. Blue brackets shows the statistical differences.

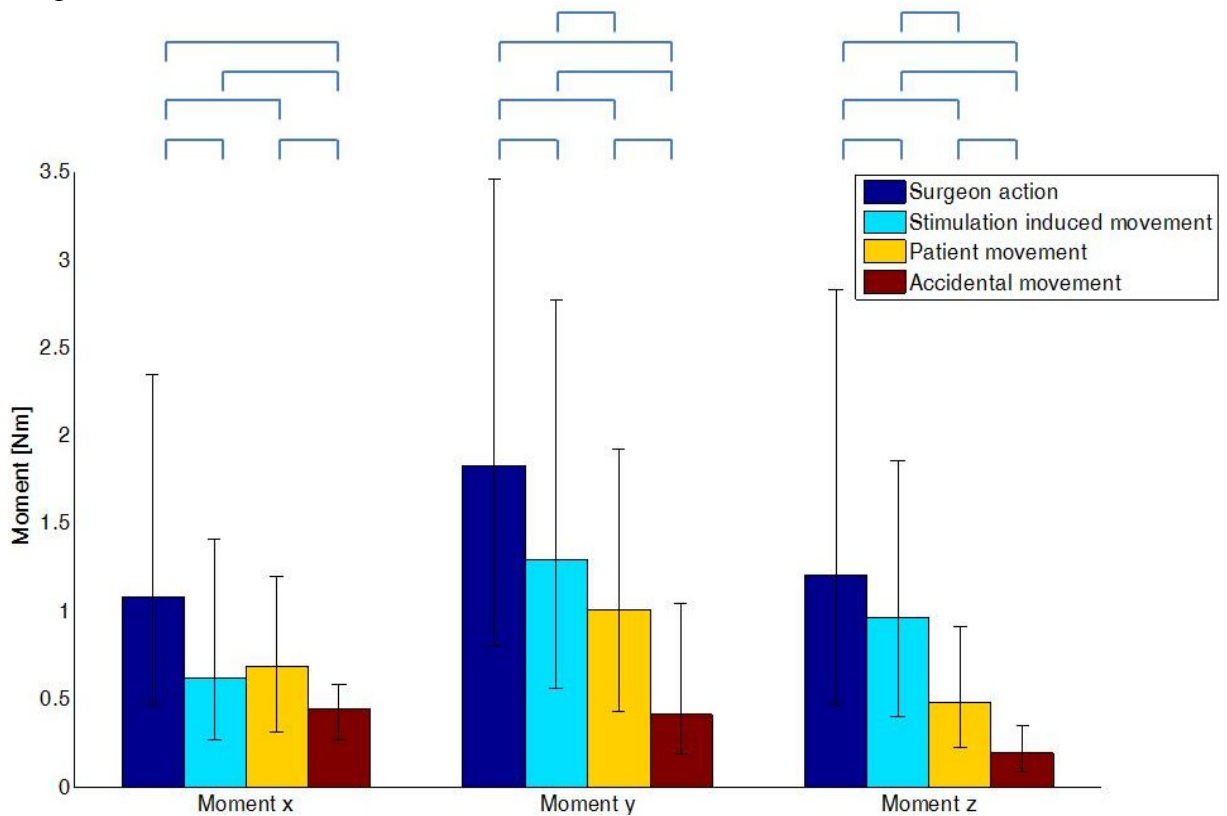


Fig. 45: summary of results obtained for moment's measurements. The highness of the colored bars indicates the median value, while the black bars indicate the 1st and 3rd quartiles. Blue brackets shows the statistical differences

Results of the statistical analyses to compare forces and moments values during different type of events are reported (blue brackets in *Fig. 44* and *Fig. 45*). For almost the tests we performed (cfr §3.1.4), we obtained a p-value less than 0.01. Only in the case of comparison between stimulation induced movements and patient movements (moment around x direction) we obtain a p-value greater than 0.01 ($p = 0.0921$).

3.1.6. Frequency domain results

As described in §2.2.7 we applied FFT to forces' and moments' signals.

In the following figures we illustrate the single-sided amplitude spectrum for the three components of forces and moments for each example showed in the previous paragraph.

SURGEON ACTION

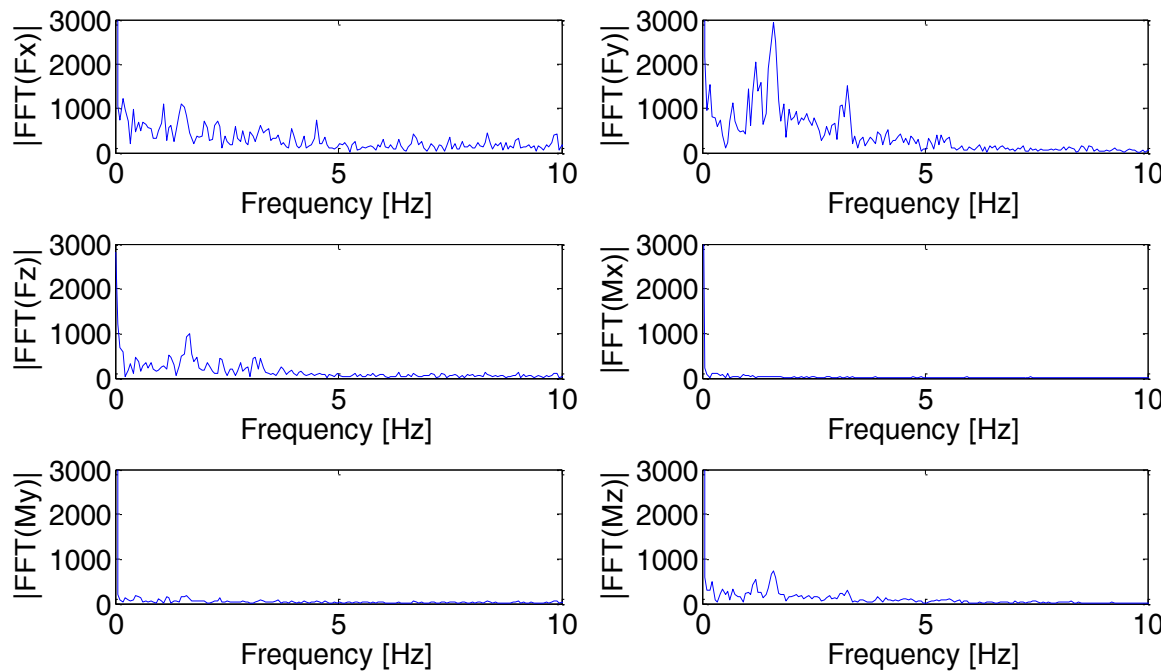


Fig. 46: single-sided amplitude spectrum for the three components of force and moment (example of surgeon actions). Zoom around low frequencies.

Analyzing these graphs and the followers, we have to remind that the force's and moment's signals were filtered using a low pass filter with a cutoff frequency of 12 Hz. We can observe that in case of force along x direction the amplitude spectrum of noise components (for frequencies greater than 5 Hz) is higher than those of the others forces and moments (peaks of 430).

In all the signals (*Fig. 46*) the significant frequency content is all in the range 0÷5 Hz. The greater components are between 0 and 0.05Hz. For all signal we find a peak around 0.2 Hz. In the case of the three forces and M_z we found clearly visible peaks around 1.5 Hz and 3.2 Hz.

PATIENT STIMULATION INDUCED MOVEMENT

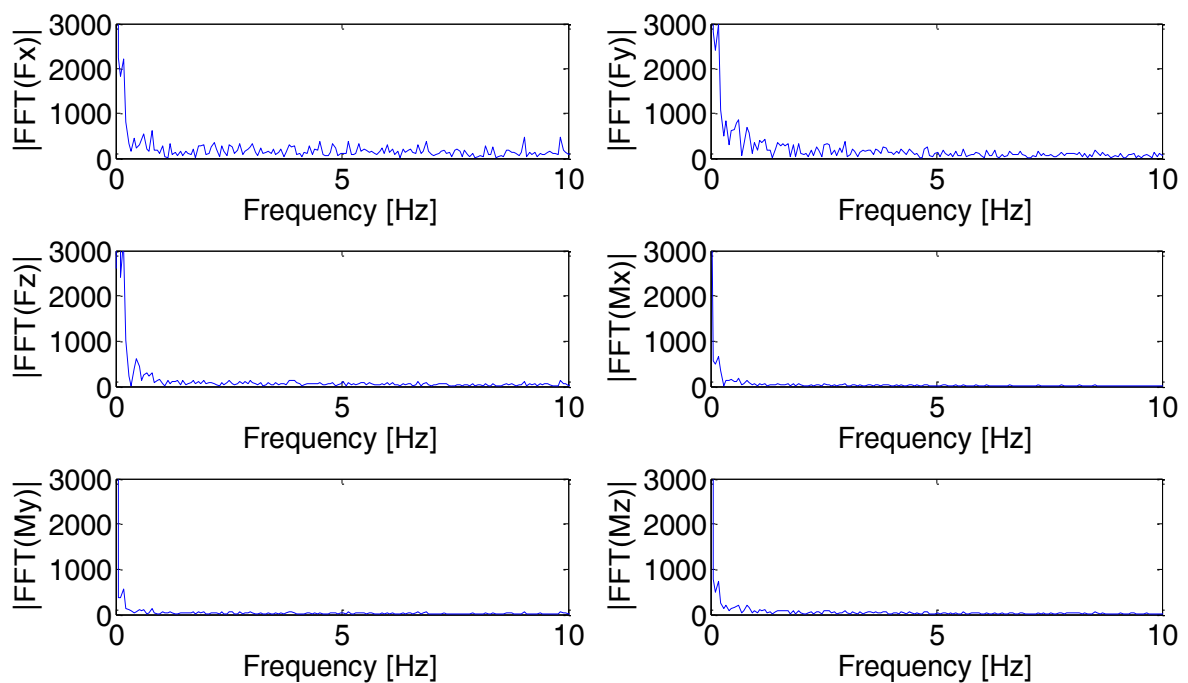


Fig. 47: single-sided amplitude spectrum for the three components of force and moment (example of stimulation induced movements)

We can notice that in this case the significant frequency content is all in the range 0÷3 Hz. In all the six signals a peak around 0.2 Hz is clearly visible.

PATIENT MOVEMENT

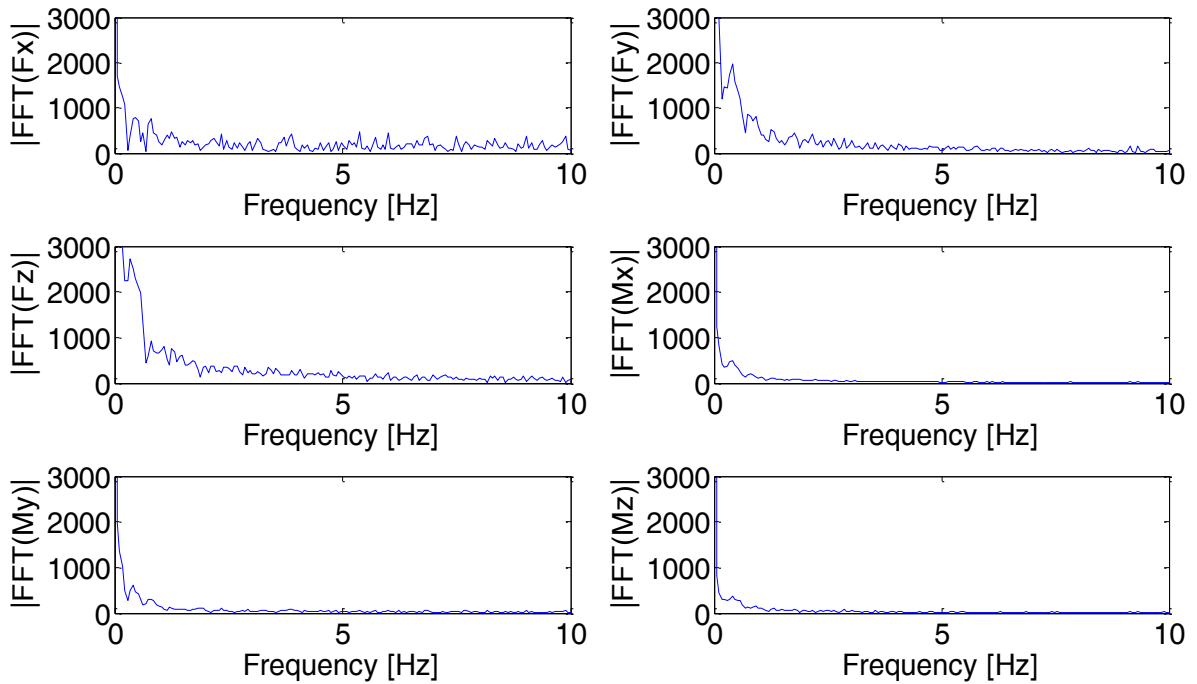


Fig. 48: single-sided amplitude spectrum for the three components of force and moment (example of patient movements).

As in the previous cases, the greater components are between 0 and 0.05 Hz and the significant frequency content is all in the range 0÷5 Hz. We observe a peak around 0.2 and 0.4 Hz in all the six signals.

ACCIDENTAL MOVEMENT

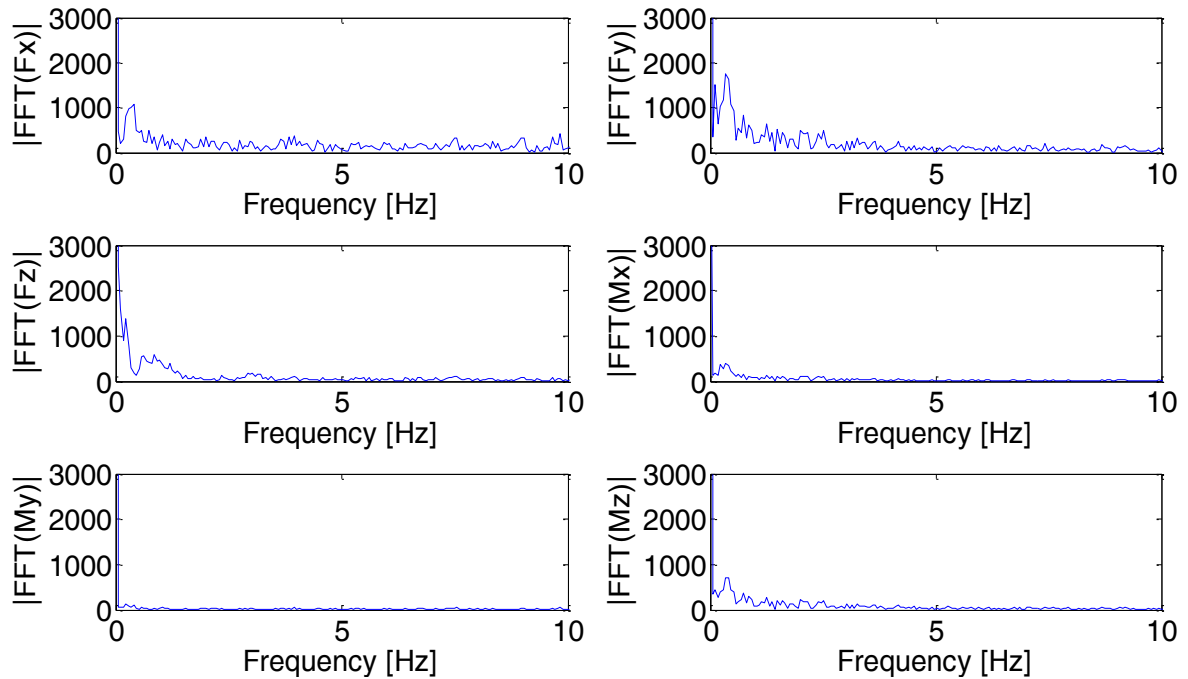


Fig. 49: single-sided amplitude spectrum for the three components of force and moment (example of accidental movements)

The frequency contents are similar to those observed in the case of other types (maximum range [0÷3Hz] was found for force along y direction). We found a peak around 0.2 Hz and 0.6 Hz in the case of force along z direction, and peaks around 0.4 Hz for the other components.

Periodic trends were found analyzing the loads' signals. They are clearly visible in the period in which we acquired the static load values of the head and c-clamp weight (cfr §2.2.6) and in others temporal segment during the intervention. In *Fig. 50* we will show the signal of force along x direction during the offset acquisition: the periodic pattern is easy to observe.

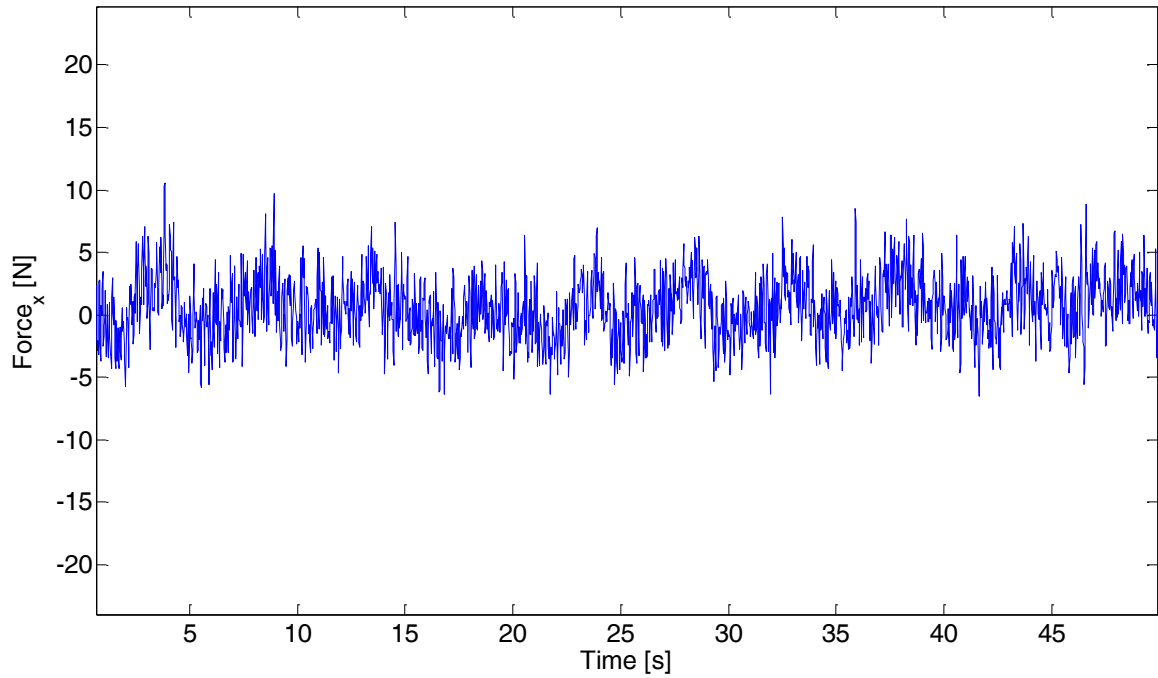


Fig. 50: force along x direction during the offset acquisition

Applying the FFT to the same signal we found a peak around 0.2 Hz (see *Fig. 51*).

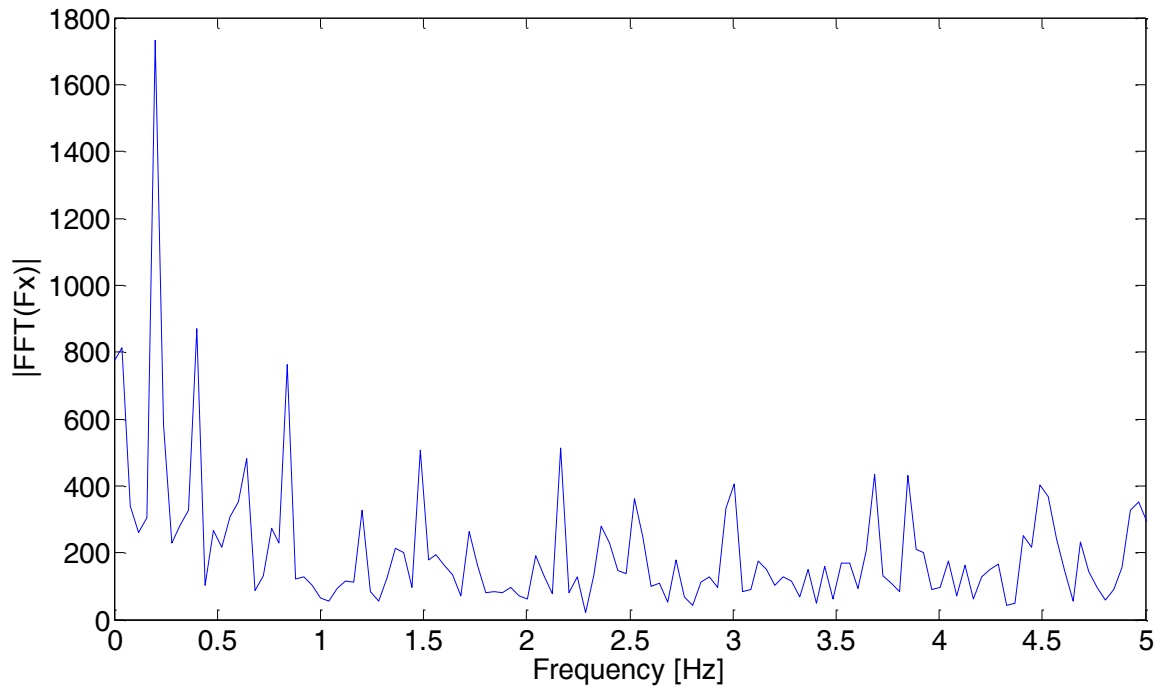


Fig. 51: single-sided amplitude spectrum of force along x direction during the offset acquisition (zoom)

In the following graphs another periodic pattern detected during segment 6 (see *Fig. 52*).

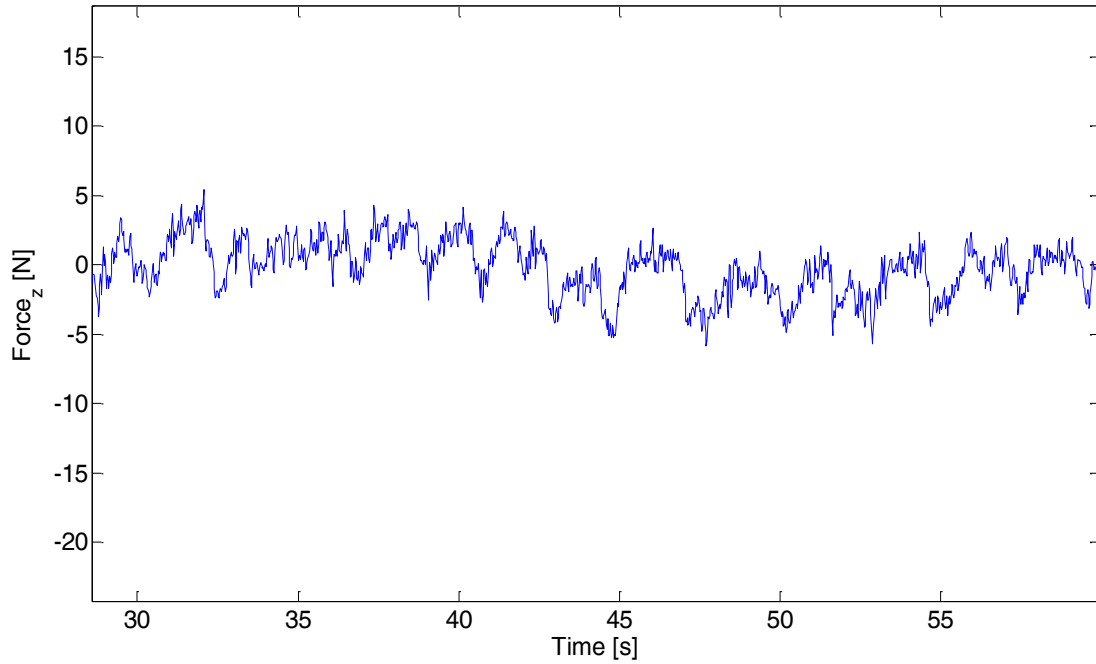


Fig. 52: force along z direction signal during the segment 6 acquisition (temporal window of about 30s)

Even in this case the periodic pattern is clearly visible, but the peak in frequency domain are around 0.5 Hz and 0.7 Hz (*Fig. 53*).

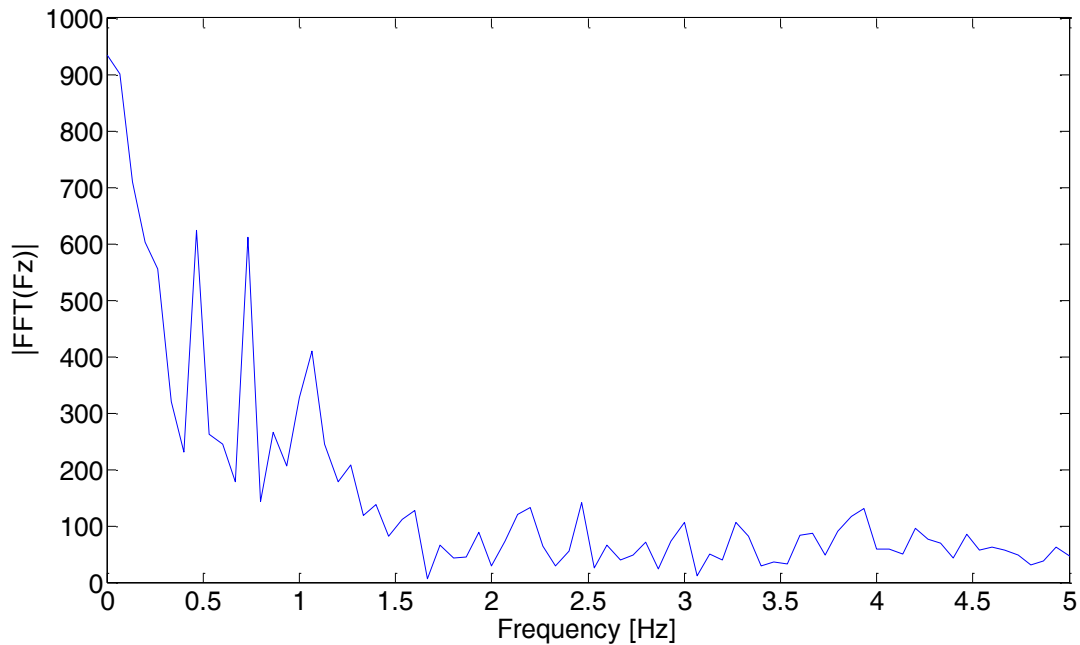


Fig. 53: single-sided amplitude spectrum of force along z direction during the segment 6 acquisition (zoom)

To show the results of STFT analysis (cfr §2.2.7), we chose to report 3-D graphs representing the STFT study of force along x direction in the four events chosen as type examples.

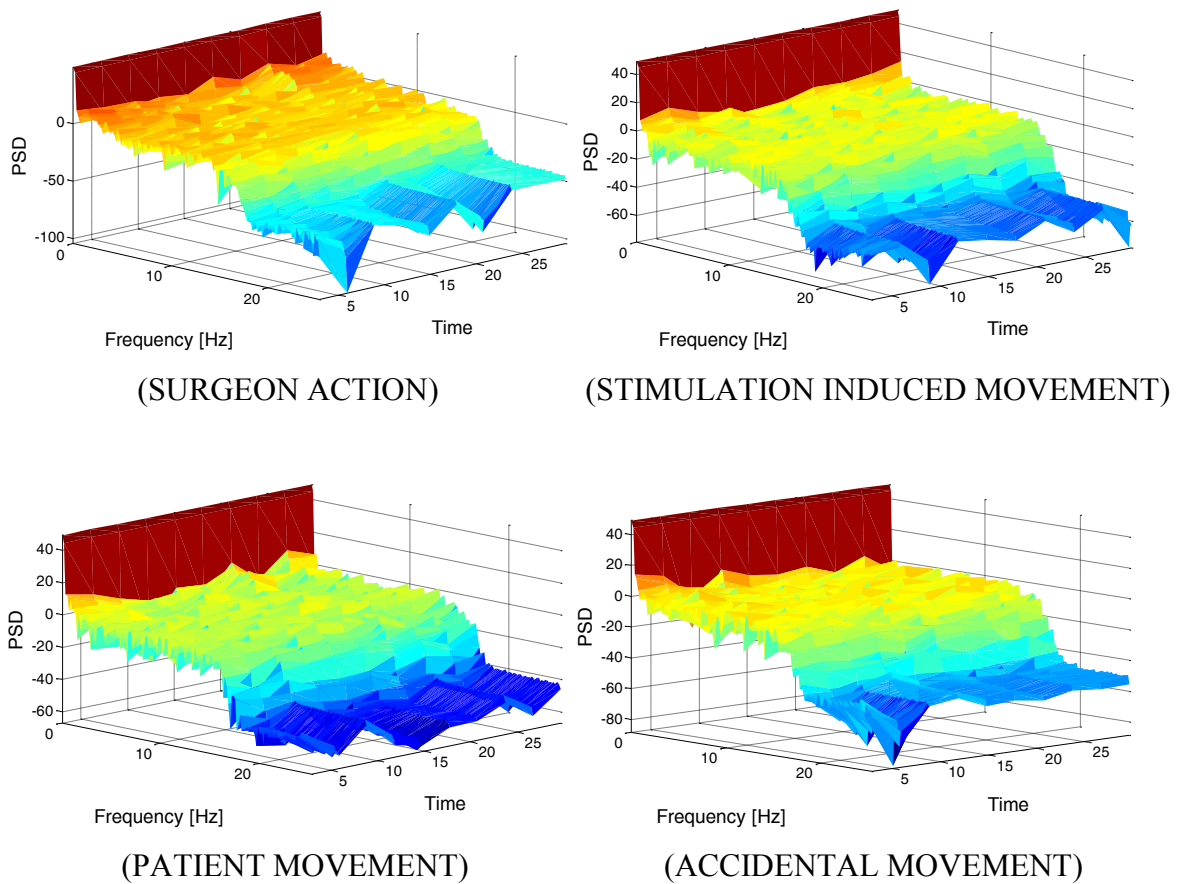


Fig. 54: 3-D graphs representing the spectrograms of the F_x signal are shown: along the three axis, the frequency, the time and PSD are reported. A colour map helps to visualize the values obtained in PSD axis. Each graphs refers to a different type example.

Frequency content of the forces' and moments' signals is in the range 0÷5 Hz. We can observe the effect of the low pass filter with cutoff frequency at 12 Hz. Studying the

frequency variations over time, we can state that the low frequencies contents increase in the same time intervals of signal peaks. Analyzing for example the graph of stimulation induced movements, we see that peaks on low frequencies can be detected around 5 and 30 s: in *Fig. 38* (force along x direction for stimulation induced movements) the signal peaks are in the same time intervals. The same behavior was found also for the others force's and moment's components.

3.2. Head's displacements, velocity and acceleration measurements

Result about of head's displacements, velocity and acceleration are shown for each type of event; we do not have available data for "stimulation induced movements" because the optical tracker tool was not always visible by our acquisition system (due to the presence of members of the medical staff between the tool and the tracking system).

For each type of event we report the maximum value, the median and the values of the 1st and 3rd quartile of displacements, velocity and acceleration (cfr §2.3).

SURGEON ACTION

The table below summarizes the results obtained for displacements', velocities' and accelerations' during surgeon actions.

Tab. 14: results of statistical analyses of displacements', velocities' and accelerations' values in each temporal instant for surgeon actions.

	Maximum value	1st quartile	Median	3rd quartile
Displacements [m]	9,00E-03	3,13E-04	6,29E-04	1,31E-03
Velocity [m/s]	6,12E-02	7,07E-04	1,12E-03	1,81E-03
Acceleration [m/s²]	8,19E-01	1,16E-02	1,82E-02	2,85E-02

In the figure below the histograms of the distribution of displacements, velocities and accelerations for surgeon actions are illustrated. The entire range of values was divided into 100 bins equally spaced.

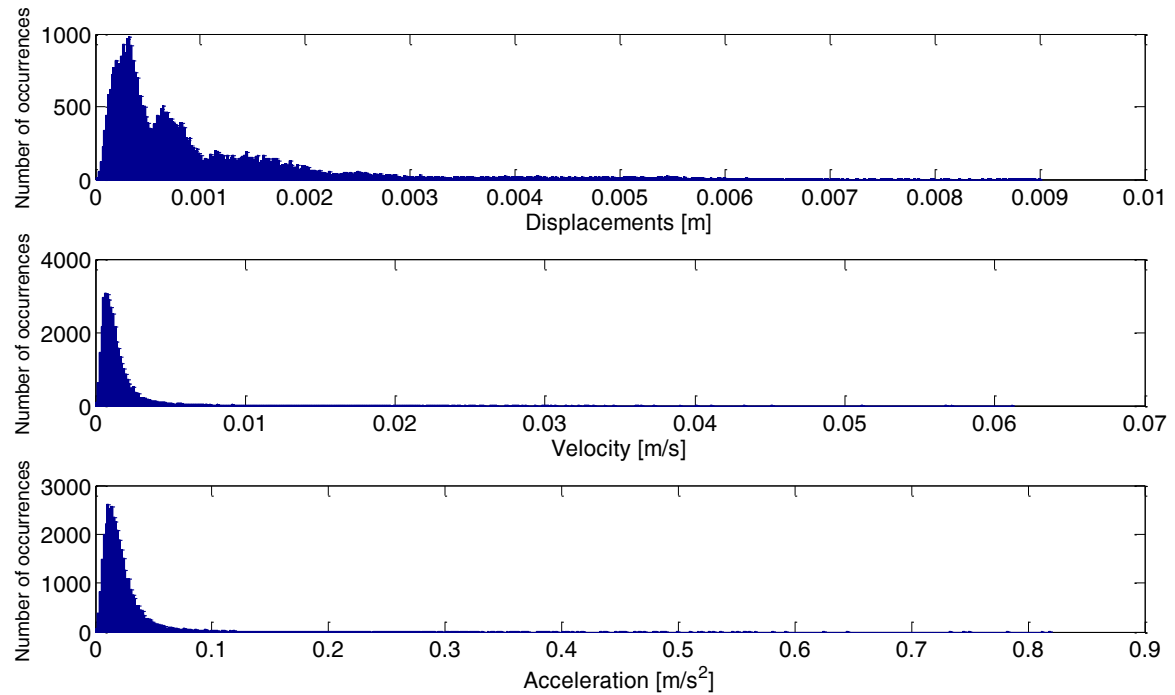


Fig. 55: histograms representing the distributions of displacements, velocities and accelerations values for surgeon actions.

According to Lilliefors test, data represented in *Fig. 55* do not come from populations normally distributed at 0.05% significance level. We can observe that in case of velocity and acceleration data are concentrated around the median value.

In *Fig. 56* the example of displacements', velocities' and acceleration's signals during a surgeon action are shown. In particular we chose a temporal window in which the surgeon was using the surgical drill.

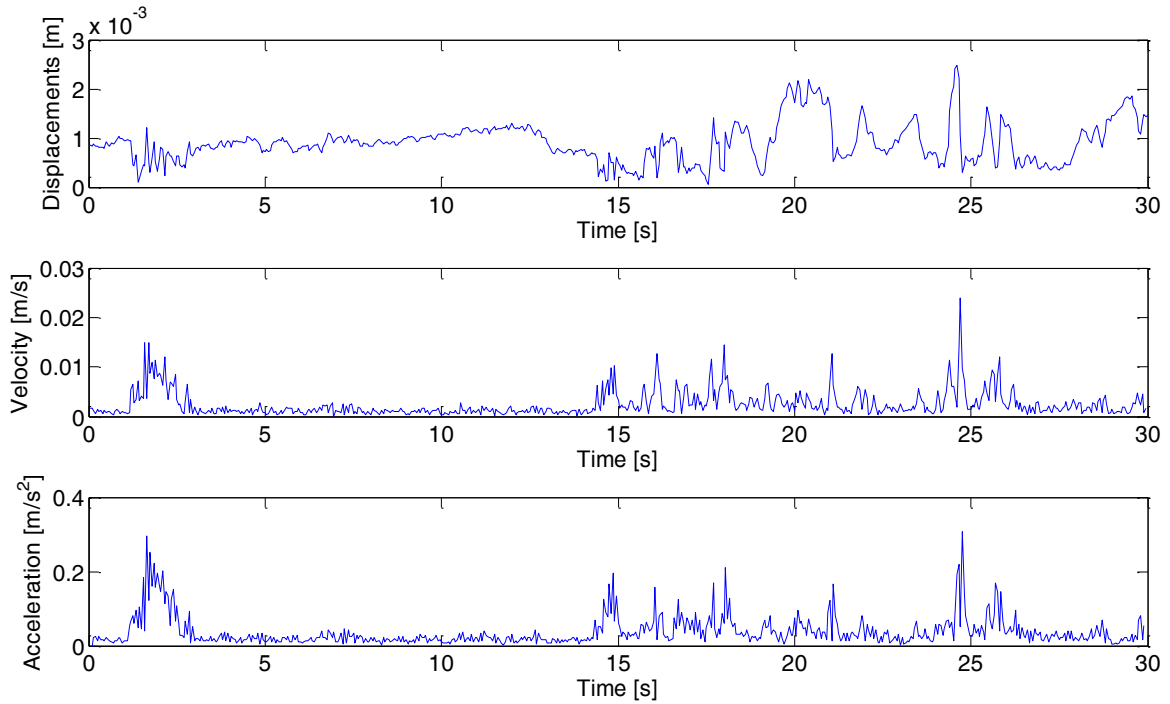


Fig. 56: displacements', velocities' and accelerations' values during the example of surgeon action (skull opening).

These shows grater values of displacements, velocity and acceleration were found during the last 15 seconds of the temporal segment we considered.

PATIENT MOVEMENT

Tab. 15 summarizes the results obtained for displacements', velocities' and accelerations' during patient movements.

Tab. 15: results of statistical analyses of displacements', velocities and accelerations' values in each temporal instant for patient movements.

	Maximum value	1st quartile	Median	3rd quartile
Displacements [m]	6,30E-03	1,65E-04	3,32E-04	5,33E-04
Velocity [m/s]	2,23E-02	6,08E-04	9,27E-04	1,39E-03
Acceleration [m/s²]	1,94E-01	1,00E-02	1,54E-02	2,28E-02

In the figure below the histograms of the distribution of displacements, velocities and accelerations for patient movements are represented.

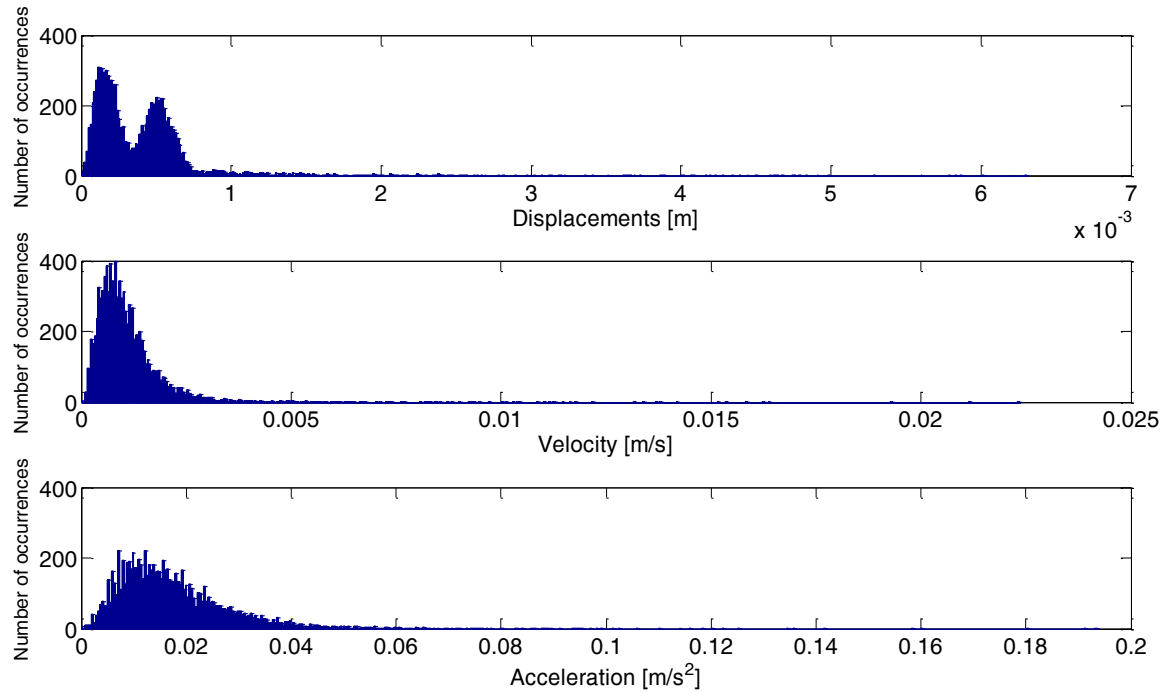


Fig. 57: histograms representing the distributions of displacement, velocity and acceleration values for patient movements.

According to Lilliefors test, data of displacements, velocity and acceleration for patient movements do not come from populations normally distributed at 0.05% significance level. In the case of displacements we found two values that presents peaks in number of occurrences.

In *Fig. 58* the example of displacements', velocities' and accelerations' signals during a patient movement. As an example of patient movement we chose a temporal window in which the patient was moving his right arm.

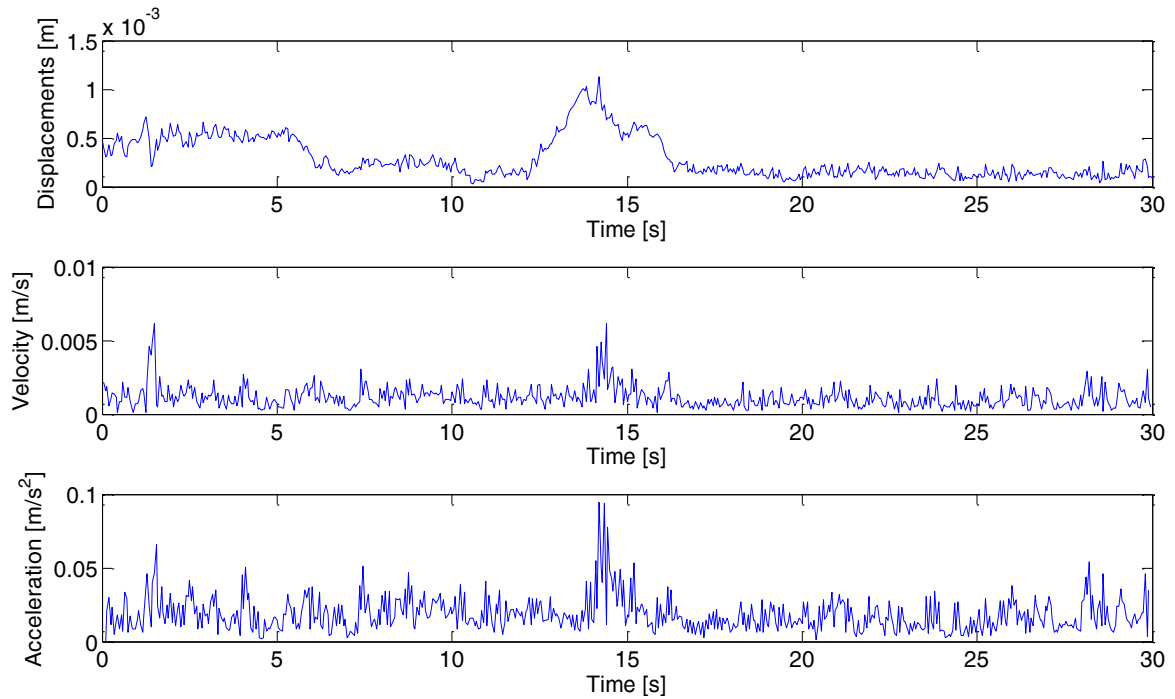


Fig. 58: displacements', velocities' and accelerations' values during the example of patient movement.

We can observe that the three signals present peaks in correspondence of the same temporal instants.

ACCIDENTAL MOVEMENT

Here the results of statistical analyses of displacements', velocities' and accelerations' values during accidental movements.

Tab. 16: results of statistical analyses of displacements', velocities' and accelerations' values in each temporal instant for accidental movements.

	Maximum value	1st quartile	Median	3rd quartile
Displacements [m]	8,88E-04	7,59E-05	1,22E-04	2,74E-04
Velocity [m/s]	5,96E-03	5,10E-04	7,87E-04	1,14E-03
Acceleration [m/s²]	1,03E-01	8,60E-03	1,29E-02	1,90E-02

We can observe that in the case of accidental movements we obtain the lowest median and maximum values for displacements, velocities and the accelerations. Maximum values for velocities and accelerations are obtained during “surgeon action” events.

In *Fig. 59* the histograms of the distribution of displacements, velocities and accelerations for accidental movements.

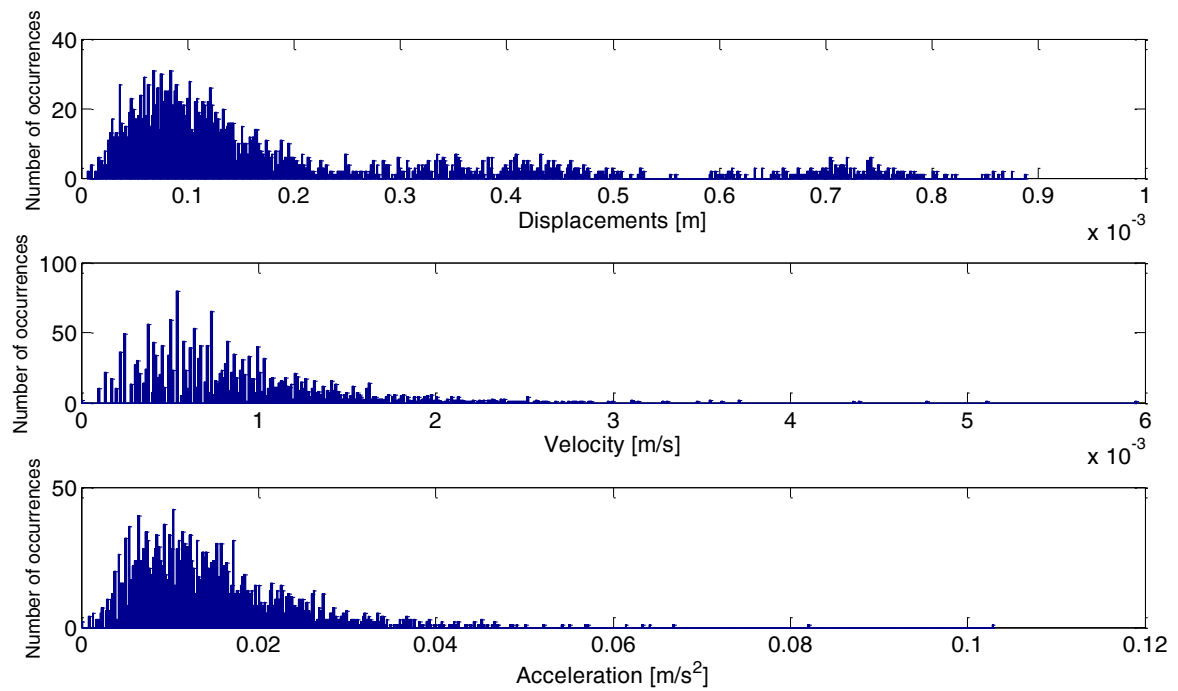


Fig. 59: histograms representing the distributions of displacement's, velocities' and accelerations' values for accidental movements.

We can observe that for accidental movements we found many values with peaks of number of occurrences for displacements, velocity and acceleration. Executing Lilliefors test, we found that data of displacements, velocity and acceleration for accidental movements do not come from populations normally distributed at 0.05% significance level.

In *Fig. 60* the example of displacement's, velocity's and acceleration's signals during an accidental movement. We chose the temporal window in which the right leg of the patient fall out of bed.

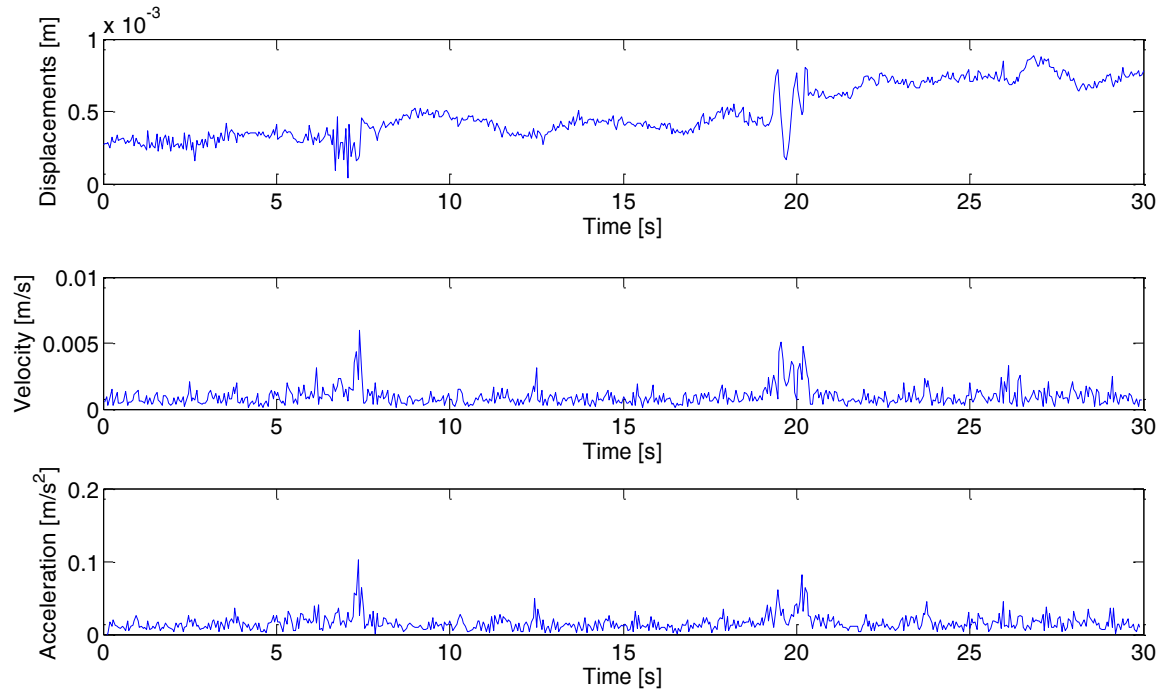


Fig. 60: displacements', velocities' and accelerations' values during the example of accidental movement.

The following histograms summarize the results obtained for displacement's, velocity's and acceleration's measurements for the three type's events.

As we can see in the following figures (blue brackets), we found statistical differences (at 0.01% significance level) between all the types of events for displacements, velocities and accelerations.

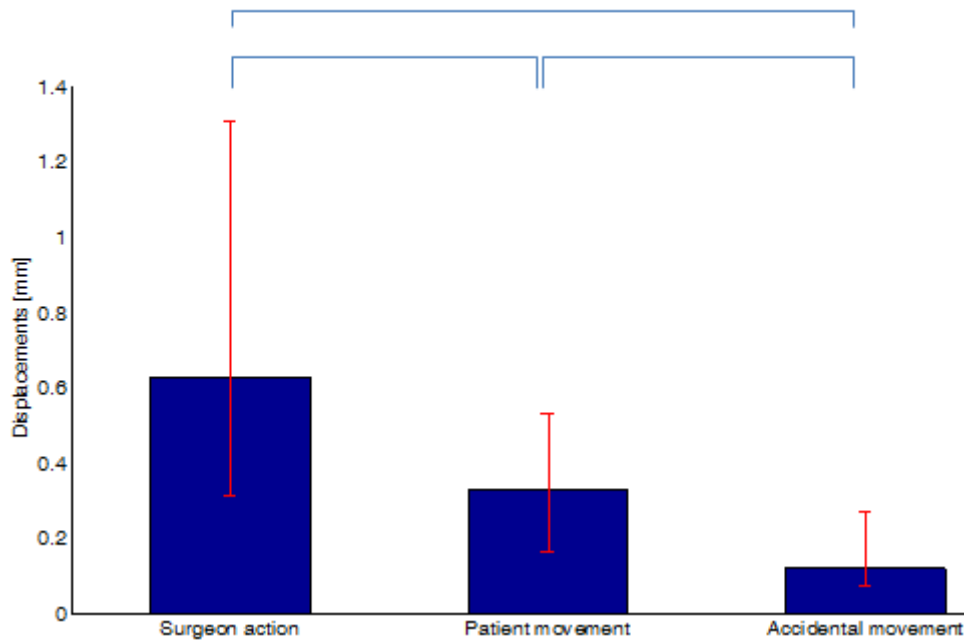


Fig. 61: summary of results obtained for displacement measurements. The highness of the blue bars indicates the median value, while the red bars indicate the 1st and 3rd quartiles. Blue brackets shows the statistical differences between the groups.

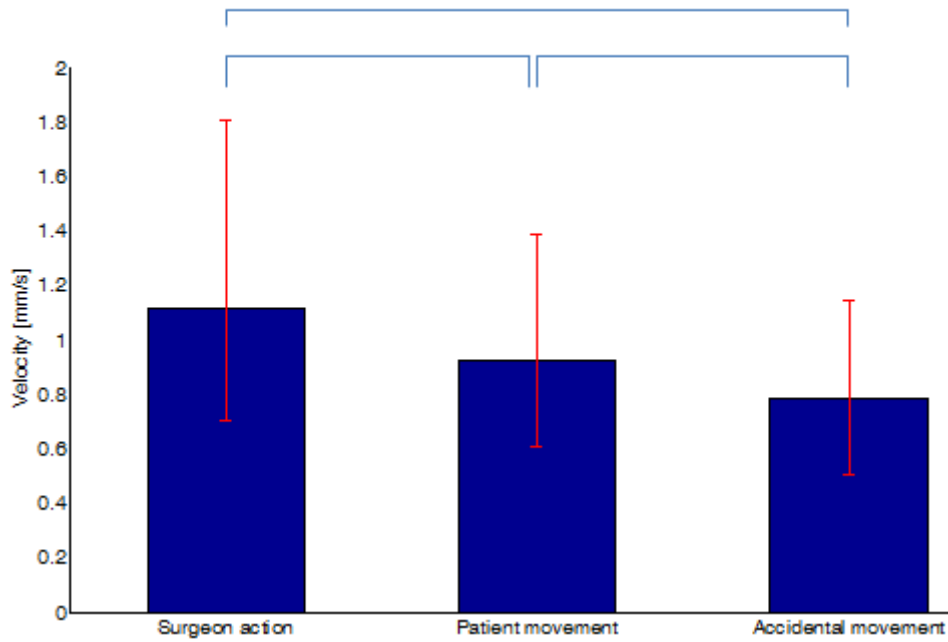


Fig. 62: summary of results obtained for velocity measurements

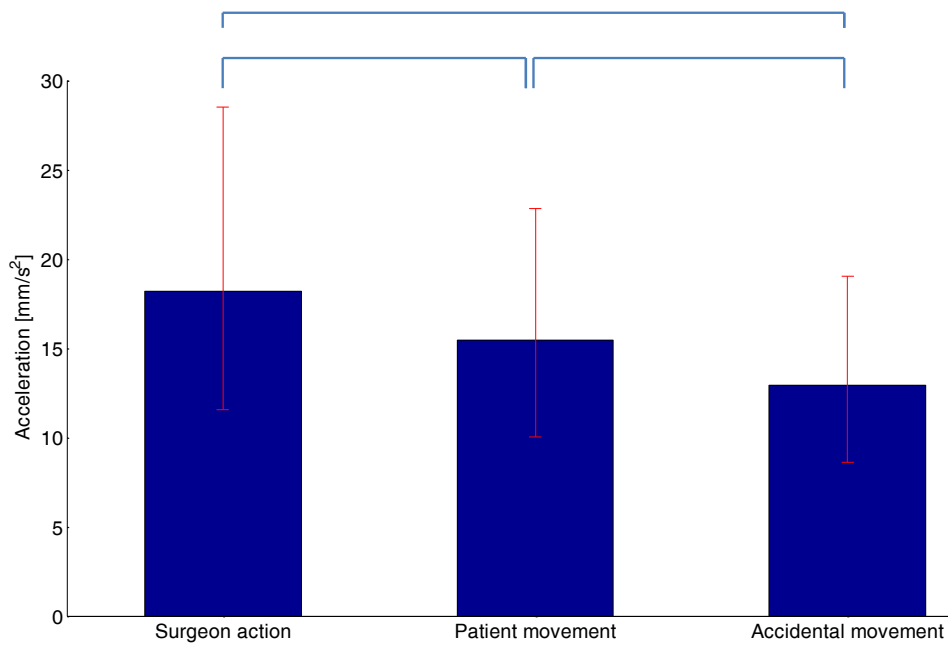


Fig. 63: summary of results obtained for velocity measurements

Chapter 4

4. Conclusions and discussions

On-field measurements of forces and moments excited by the patient's head during awake neurosurgery interventions were carried out. Our results were used to provide quantitative requirements for the AH design and implementation in the context of the European funded project Active (cfr §1.1.2).

We chose to use a system of six double SGs in order to measure the strains on the Mayfield[®] positioning system (cfr §2.2.2) and then calculate forces and moment applied on the structure through a calibration procedure (cfr §2.2).

4.1. Simulation analyses

Simulation analyses based on FEM methods were performed in order to choose the position of SGs. We realized a CAD model of the positioning system and the volumetric mesh used for stress/strain analyses was evaluated using aspect ratio and geometric deviation factor metrics. Mesh evaluation results were satisfying because only less than 0.05% of elements presented a critical value for the metrics we chose and hexagonal elements were used to model the parts of the structure where major strains were probable.

The SG's position was chosen as illustrated in §2.2.2.

The value of the condition number of the strain calibration matrix obtained in simulation shows that our system of measure do not exhibits isotropy and do not provide the same measurements sensitivity for all the six components of the vector \vec{F} . Condition number is also an influencing factor that effects the transmission of the errors from the measured

strains to forces [18]. Generally, in sensor's structure design phase, computer-aided analyses are usually performed in order to bring the condition numbers of the strain calibration matrices as close as possible to unity, through sensor shape's optimization (in literature we usually find values between 1 and 4 for condition numbers [18]). This kind of optimization was not possible in our case because we could not design the shape of the sensor and our structure (i.e. Mayfield positioning system) was not modifiable. Also the choice of SG's position was influenced by contingent factors (e.g. the need to not create disturbance for the medical staff and to not limit the relative movements between each arm of the structure). For this reason we could not attach a greater number of sensors and we could not consider all the parts of the structure as possible SG's locations. As consequence, the choice of SG's positions could not be optimized in order to obtain high measurements sensitivity.

The correlation coefficients of the simulation's strain compliance matrix show that our system is coupled which means that the output of each SG is affected by the application of all the force's and moment's components. Residual calibration errors calculated using simulated data were negligible (maximum values of 5×10^{-6} N in the case of forces and 1×10^{-3} Nm for the moments). Also the errors in the estimation of forces and moments computed in the case of accuracy evaluation were largely lower than expected errors for our application (cfr§3.1.1).

The calibration procedure in simulation was executed as explained in §2.2.2 and we found linear relationship between loads applied and strains. Since there is a linear relationship between strains and SG's output (see (8)) we expected a liner relationship between load's applied and SG's output. This result could be expected because the entity of loads applied (55N max) allows us to consider only the linear elastic behavior of the clamp.

4.2. On-field measurements

The experimental calibration procedure was executed as described in §2.2.4. We found an almost linear relationship between loads applied and measured strains. It was not perfectly linear probably because of inaccuracy introduced using SGs (such as nonlinearity of the sensor characteristic or bad bonding conditions) or to inaccuracy in load's application during the calibration procedure. However, coefficients of determination calculated for our linear regression model are always greater than 0.7 in the case of forces, thus indicating a good global fit. In the case of moment this statement is not true for all the SGs. In particular the moment around the y axis presented the most critical situation (*Tab. 6*). This result is probably due to inaccuracies in the application of load's during the experimental calibration for this component. The result obtained could be explained also by the SG's position because the worse R^2 coefficients were found for SGs that have less sensitivity for the moment around y axis. It is probably for these reasons that the highest percentage calibration residual errors (*Tab. 7*) were found for this component (especially for lower loads).

Absolute residual calibration errors obtained with experimental data has median values lower than median values of loads found during the intervention for all components, except for moment around y direction. Maximum median values for residual calibration error were found for force in x direction (5.5N) and moment around y axis (3Nm).

The strain compliance matrix obtained with experimental calibration shows (as in the situation of simulation analyses) that our system of measure is not isotropic (but the condition number is less than that found in simulation) and is coupled as expected.

On field measurements were carried out during a tumor resection awake neurosurgery intervention.

By measuring the static components of forces given by the head's and the c-clamp's weight we found the results shown in *Tab. 9*. As we expected the maximum value is for

force along the x direction (i.e. gravity force direction). The value of 138.9 N that we found could be explained by considering the head weight (about 7.5% of the total body mass [22] that in our patient's case was 84 kg), the weight of the c-clamp (1.350 kg) and the fact that, considering the patient position showed in *Fig. 19*, part of the weight of neck and shoulders is supported by the positioning system.

As shown in §3.1.3 our signal showed a slow trend during the first hour of intervention: the values of forces obtained without removing it (up to 1000 N in y direction) lead us to consider it as an electronic trend. It could be due to the fact that the part where the sensors were attached has been wet at the beginning of the intervention; another hypothesis is a progressive changing of the operating room's temperature (even if thermal effects are theoretically compensated using half bridge configuration). This trend was removed because we were interested in the net signal's variations with respect to the base line (that represents the value of SG's output when only the static component is applied on the positioning system).

Maximum values of forces and moments found during the intervention are summarized in *Tab. 8*. They were measured during the phase of the surgical operation in which the surgeon uses the surgical drill in order to open the skull and in the last phase of the intervention during suturing. In this phase the medical staff directly applies significant forces on the head of the patient. Analyzing the signals of forces applied during the use of surgical drill, we found the greatest values for force along y direction: this is plausible considering the patient's head position with respect to the defined reference frame (*Fig. 19-Fig. 20*).

As specified in §3.1.4, we decided to divide all the events occurred during the intervention in four different types in order to find possible differences in force's and moment's values. Statistical differences were found at 0.01% significance level between for all the components of force and moment between each type of event (except for moment around x direction). Maximum values found in the case of patient movements are higher than those found for stimulation induced movements and are generally less than those of surgeon actions (except for force along the z axis).

This shows that maximum forces and moments are exerted by the medical staff (surgeon action); it shows also that forces and moments due to unexpected movements of the patient (patient movement) are higher with respect to those induced by stimulation or requested by the surgeon (stimulation induced movements).

Analyzing this result we have to consider that the medical staff never asks to the patient to move the head: stimulation induced movements are always arms' or legs' movements that do not involve loads' application on the positioning system. Moreover, that patient's unexpected movements are often to be considered as unexpected reactions due to pain or uncomfortable position of the body that involve loads' application on the skull clamp. Also in case of accidental movements, we obtain forces' and moments' values less than those obtained for surgeon actions and patient movements.

Observing maximum values of moments and forces exerted by the patient during patient movements (movements not requested by the medical staff) we can conclude that they are significantly lower than those found in [12], [13] and [14]. This is an expected result because in these works the subjects of the study were asked to exert the maximum possible torque with their neck muscle strength, while in our case the patient is sedated and is asked to be relaxed.

Results of analyses in frequency domain (sfr §3.1.6) show that for all the types of events the frequency content of all the force's and moment's components is in the range 0-5 Hz with a great prevalence of components between 0 and 0.5 Hz. This result is plausible since forces are caused by the action of the surgeon that usually execute slow movements or by the patient that is under anesthesia or sedated. Also the STFT analyses confirm this result showing that low frequencies components increases their amplitude in the same temporal instant in which we find peaks in the forces' signals.

In the case where forces along y axis are applied for surgeon actions, there are greater components at higher frequencies than in other cases: this is probably due to the use of the surgical driller that, as described above, excite a force mainly in y direction.

Peaks around 0.5 Hz and 0.2 Hz shown in *Fig. 51* and *Fig. 53* are probably caused by motor evoked potential and patient's breathing, respectively. This was verified comparing

our load's signal with stimulation signals provided by the neurophysiologist: during those temporal segments of the intervention the MEP frequency was 0.5 Hz and the patient was breathing autonomously.

Results found for displacements, velocities and accelerations measurements confirm the results of forces' and moments' analyses since the maximum values were found in the case of surgeon actions (9 mm for displacements, 0.06 m/s for velocity and 0.8 m/s² for acceleration). We found statistical difference at 0.01% significance level between each type of event for displacements, velocities and accelerations. These values are to be considered during the AH and motion compensation design phase. The values of displacements that we found could be reduced (through the modification of AH compliance) during the phases of the intervention in which high accuracy and target's immobility are desirable (e.g. presence of surgical tools in contact with brain tissue). During other phases the AH compliance could be increased (through the use of a system of active dampers) in order to prevent possible skull damages due to skull clamp's pins.

We have to remind that these results depend on the stiffness of the positioning system and acceleration's data cannot be used to directly estimate the force exerted by the head. Only an evaluation of the positioning system in terms of maximum displacements of the head and constrained force exerted on the skull can be carried out.

4.3. Future developments

Since there are no references in literature about the topic of forces and moments measures exerted by the head during awake neurosurgery procedures, this work could represent a starting point for this type of intra-operative measurements.

One acquisition was carried out and data we obtained has to be validated with others on-field measurements. In particular, it could be interesting to test if the values obtained in

forces and moments measurements change in relation to sex, age or anthropometric data of the patient. However, this comparison is not easy to carry out because values of forces and moments change in relation to the head's position with respect to the positioning system; also the body position on the bed can significantly modify the measured values.

Another interesting analysis that could be done with new acquisitions is about the repeatability of force's and moment's values measured during standard surgeon's action (such as scalp opening, use of surgical drillers or suturing).

An improvement in data interpretation could be expected by integrating the evaluation of the load's signals with analysis of vital parameters monitoring signals (ECG, EEG or blood pressure), EMG or electrical stimulation signals (e.g. MEP). In particular relationship between the frequency content of the signal mentioned above could be found.

This forces' measurement could be used also to directly monitor forces exchanged between the patient's cranium and the skull pins used for skeletal fixation; in the future a security system that warns the surgeon when a force threshold is exceeded in order to prevent damages to the patient (e.g. intracranial hematoma or depressed skull fractures in pediatric patients) could be developed. Data about displacements and velocity could represent a good evaluation metric for the positioning system in terms of stiffness.

Finally, force's and moment's measurements during the occurrence of epileptic seizures could be useful to understand the entity of forces exerted by the patient and their range of frequency during this particular event.

Appendix I

In *Tab. 17* we report the mean (first row) and maximum values (second row) of the six components of vector \vec{F} during each temporal segment of the surgical intervention. On the left we reported also the time duration of the segment and a brief summary of the events that characterized each segment.

As specified in §3.1.4, we chose to divide all the events that occurred during the intervention in four types that group events of the same nature (or that share the same causes). We chose the following classes:

- **Surgeon action:** events caused by the action of the surgeon or by the medical staff [C].
- **Patient stimulation induced movement:** patient's movements caused by electrical stimulation or requested by the medical staff [S].
- **Patient movement:** patient's movement (voluntary or involuntary) not requested by the medical staff [P].
- **Accidental movements** [W]

The red letter between brackets represents the type for each event.

It should be noticed that the maximum values for the six components in *Tab. 17* do not refer to the same time instant. Thus, it is not possible to compute the vector sum from each singular maximum force component (F_x , F_y , F_z) in order to compute the module of the force vector (the same applies for the moment vector).

Tab. 17: results summary of the intervention. In the third column there are the main events occurred during the intervention. In the following columns mean (first row) and maximum (second row) value for forces [N] and moment [Nm] during each temporal segment of the intervention are reported.

Segment number	Duration [min]	Events	F _x mean and max [N]	F _y mean and max [N]	F _z mean and max [N]	M _x mean and max [Nm]	M _y mean and max [Nm]	M _z mean and max [Nm]
1	5	Start of acquisition	140,375	-20,925	2,740	-7,292	34,261	10,873
		Offset acquisition (only the weight of the head is measured)						
		Surgical setup preparation [C]	194,538	-46,997	17,056	-10,358	39,675	17,977
		Surgical sheet fixing [C]						
2	10	Scalp opening and use of the electro-surgical cutting device [C]	143,359	-19,729	2,551	-6,995	33,905	11,035
		Raney scalp clips application [C]	194,723	-64,402	24,083	-10,263	42,268	23,557
3	22	Skull surface cleaning using a surgical instrument [C]	140,039	-20,142	2,622	-7,077	34,368	11,075
		Use of the optical localizer pointer						
		Starting of skull opening with surgical drill (30 seconds) [C]						
		Use of bipolar forceps (40 Hz) and surgical aspirator [C]						
		Alternate use of surgical drill and aspirator [C]						
Scalp clip removal using forceps [C]	242,645	-91,797	33,421	-18,040	47,966	37,546		
Removal of a calvaria part [C]								
Starting of awake phase, light anesthesia (the patient is not awake yet)								

4	29	Displacement of gauze [C]	141,771	-25,641	3,713	-8,109	33,528	9,493
		Use of aspirator, bipolar forceps (40 Hz) and water. [C]						
		Starting of muscles activity [P]						
		The nurse touch the patient's face trying to wake him [C]						
		The patient open the mouth and the breathing tube is removed [C]-						
		The patient is awake and starts speaking [S]						
		Microphone positioning for awake neurosurgery and foot movement [C]						
		Preparation of monopolar and bipolar stimulator [C]						
		The patient is asked to count [S]						
		Use of stimulator (2, 2.5 and 3.5 Hz) [S]	177,625	-69,173	-31,783	-16,296	42,619	21,147
		The patient begins to visualize and recognize images[S]						
		Use of monopolar stimulator (2Hz) and MEP research [C]						
		Use of the optical localizer pointer [C]						
5	32	Use of US probe [C]	138,195	-18,605	1,496	-6,751	34,707	11,433
		The patient moves his right hand[S]						
		The surgeon begins to use the electron microscope [C]						
		The patient starts speaking [S]						
		Use of electro-surgical cutting device [C]						
		The surgeon begins to operate on the cerebral tissue [C]						
		Arm muscle contraction [P]						
		The patient is speaking [S]						
		Leg and foot movement [P]	161,864	-39,593	27,147	-10,724	39,876	19,591
		The patient visualizes and recognizes images [S]						
		Drainage gauze positioning [C]						

6	21	The patient is recognizing the images [S]	138,646	-19,146	1,566	-6,841	34,562	11,311
		Use of electro-surgical cutting device [C]						
		MEP amplitude variation						
		MEP reduction						
		Use of surgical aspirator [C]						
		The patient is asked to open and close his hand [S]						
		Hand and arm movement [P]						
		Use of spatula [C]						
		Right foot movement [P]						
		The nurse is moving the patient's foot and leg [C]						
		The surgeon is operating immediately above the insular cortex [C]	163,701	-34,149	25,292	-10,360	40,214	21,561
		Leg, foot and head movement [P]						
		Use of electro-surgical cutting device [C]						
		MEP reduction						
		The patient is asked to move his hand [S]						
		Use of spatula [C]						
7	10	The patient is asked to open and close his hand [S]	138,797	-20,026	2,142	-7,107	34,434	10,994
		Tumour mass removal using electro-surgical cutting device [C]	155,728	-40,890	19,868	-10,983	42,347	26,427
		The patient is asked to recognize images. [S]						
		Leg movement [P]						
		Use of electro-surgical cutting device and tumour mass removal [C]						
		Image recognition [S]						
		Foot movement [P]						
		Right leg and arm movement [P]						

		Use of the optical localizer pointer [C] Use of electro-surgical cutting device[C] Leg movement [P] Use of surgical aspirator [C] Leg movement [P] Use of the optical localizer pointer [C]	174,421	-48,703	35,990	-11,371	41,373	20,075
9	28	Use of electro-surgical cutting device [C] Face muscles mapping: train of 5 stimuli (10 mA) in 20 ms . [S] Left arm movement [P] Leg movement [P] Use of Ojemann stimulator [C] Foot movement [P] MEP control [C] The patient is moving [P] Recognition of images [S] Use of monopolar stimulator: train of 5 stimuli (10 mA) [C] Research of facial muscle response[S] The surgeon is stimulating in the motor region [S] 15 mA stimuli (using 10 mA stimuli the response is not found) [S] The patient hand is moved [S] Motor cortex mapping [S]	138,646	-19,192	2,345	-6,955	34,562	11,332
			190,267	-42,919	45,909	-12,688	42,151	21,297
10	21	Leg movement [P] Use of surgical aspirator [C] Image recognition [S] Left leg movement [P]	139,395	-19,563	2,274	-6,971	34,574	11,349

Appendix I

		Use of electro-surgical cutting device [C]						
		Use of monopolar stimulator [C]	179,468	-46,496	37,914	-14,841	46,313	15,082
		Legs and arms movement [P]						
		The nurses moves the legs of the patient [C]						
11	24	Images recognition [S]						
		Use of aspirator [C]	139,219	-19,961	2,215	-7,107	34,703	11,088
		Leg and foot movement [P]						
		Use of the optical localizer pointer [C]						
		Use of electro-surgical cutting device [C]	160,864	-51,945	-26,327	-15,736	49,667	14,032
		Large movement of the head [P]						
		Use of bipolar coagulator [C]						
12	31	Use of aspirator [C]						
		Leg and arm movement [P]	139,028	-19,474	2,079	-6,967	34,481	11,226
		The patient is awake						
		Nurses are moving patient's leg and arm [C]						
		Right arm movement [P]	176,543	-84,346	35,914	-16,005	58,091	19,405
		The surgeon move the skull clamp to see our strain gauge signals [W]						
13	32	Use of bipolar coagulator [C]						
		Left leg movement [P]	138,773	-19,614	2,488	-7,006	34,430	11,187
		Right arm movement [P]						
		Suturing [C]	190,598	-68,849	56,555	-12,868	39,774	14,807
		The neurophysiologist is moving the patients legs to remove the electrodes [C]						
14	32	Suturing [C]	139,129	-19,672	1,728	-6,993	34,550	11,122
		Leg movement [P]						
		The right leg fall out of bed [W]						
		Use of aspirator [C]	243,971	-114,695	65,558	-17,082	50,816	16,259
		Arm movements [P]						

15	32	Right leg movement [P]	139,423	-19,158	1,733	-6,956	34,468	11,216
		Skull bone repositioning [C]						
		Arm movement [P]						
		Positioning of surgical staples [C]						
		The patient is awake and he's moving [P]						
		Skin positioning [C]						
		The patient is moving because he feels pain [P]						
		The surgeon is pulling the sutures [C]						
		Suturing of the skin [C]	219,175	-100,331	57,827	-18,947	52,060	19,908
		Use of bipolar forceps [C]						
		The patient is moving a lot						
16	8	Cleaning using gauze and removal of optical localizer tool. [C]	141,535	-20,631	0,996	-7,023	34,984	11,107
		Removal of surgical drapes and head cleaning [C]	211,867	-103,793	45,339	-25,919	76,661	18,239

References

- [1] N. Tzourio-Mazoyer, «Interindividual variability in the hemispheric organization for speech,» *Neuroimage*, vol. 21, pp. 422-35, 2004.
- [2] H. Duffau, «Lessons from brain mapping in surgery for low-grade glioma: insights into associations between tumour and brain plasticity.,» *The Lancet Neurology*, vol. 4, n. 8, pp. 476-486, August 2005.
- [3] w. Lanier, «Brain tumor resection in awake patients,» *Mayo Clinic Proceedings*, vol. 76, n. 7, July 2001.
- [4] A. Szelényi, L. Bello e H. Duffau, «Intraoperative electrical stimulation in awake craniotomy: methodological aspects of current practice,» *Neurosurgical Focus*, vol. 28, n. 2, 2010.
- [5] J. J. Van Gompel, G. A. Worrell e M. L. Bell, «Intracranial electroencephalography with subdural grid electrodes: techniques, complications and outcomes,» *Neurosurgery*, vol. 63, n. 3, pp. 498-506, September 2008.
- [6] J. Dreier, B. Williams, D. Mangar e E. Camporesi, «Patients selection in awake neurosurgery,» *HSR proceedings in intensive care & cardiovascular anesthesia*, vol. 3, n. 4, 2009.
- [7] «FP7-ACTIVE- Annex I:"Description of Work",» 2010.
- [8] C. Richards, J. Rosen, B. Hannaford, C. Pellegrini e M. Sinanan, «Skills evaluation in minimally invasive surgery using force/torque signatures,» *Surgical endoscopy*, vol. 14, n. 9, pp. 791-8, 2000.

-
- [9] T. Mutoh, T. Ishikawa, H. Nishimura e N. Yasui, «Application of the FlexiForce Contact Surface Force Sensor to Continuous Extraocular Compression Monitoring During Craniotomy for Cerebral Aneurysms,» *Journal of Neurosurgical Anesthesiology*, vol. 22, n. 1, pp. 67-72, January 2010.
- [10] T. Hoell, M. Nagel, G. Huschak, A. Beier e H. J. Meisel, «Electromyographic investigation on handling forces of mechanically counterbalanced and sensor-servomotor-supported surgical microscopes,» *Surgical Neurology*, vol. 63, n. 5, pp. 434-441, 2005.
- [11] A. N. Vasavada, S. Li e S. L. Delp, «Three-Dimensional Isometric Strength of Neck,» *SPINE*, vol. 17, n. 26, pp. 1904-1909, 2001.
- [12] S. Kok-Yong, L. P. Vee-Sin e L. Pin-Min, «Neck muscle strength across the sagittal and coronal planes:an isometric study.,» *Clinical Biomechanics*, vol. 17, pp. 545-547, 2002.
- [13] P. E. Olivier e D. E. Du Toit, «Isokinetic neck strength profile of senior elite rugby union players,» *Journal of Science and Medicine in sport*, vol. 11, pp. 96-105, 2008.
- [14] A. Rezasoltani, J. Ylinen, A.-H. Bakhtiary, M. Norozi e M. Montazeri, «Cervical muscle strength measurement is dependent on the location of thoracic support,» *British Journal of Sports Medicine*, vol. 42, n. 5, pp. 379-382, 2007.
- [15] C. Lu-Ping e Y. Ching-Yan, «The six-component force sensor for measuring the loading of the feet in locomotion,» *Materials & Design*, vol. 20, pp. 237-244, 1999.
- [16] K. Gab-Soon, S. Hi-Jun e Y. Jungwon, «Development of 6-axis force/moment sensor for a humanoid robot's intelligent foot,» *Sensors and Actuators*, vol. 141, pp. 276-281, 2008.
- [17] M. Gobbi e al, «Measurement of the forces and moments acting on farm tractor pneumatic tyres,» *Vehicles System dynamics*, vol. 43, 2005.
- [18] A. Sheng e L. Hung, «A novel six-component force sensor of good measurement isotropies and sensitivities,» *Sensor and actuators*, pp. 223-230, 2002.

- [19] K. Gab-Soon, «The design of a six-component force/moment sensor and evaluation of its uncertainty,» *Measurement Science and Technology*, vol. 12, n. 1445-1455, 2001.
- [20] A. L. Rhoton, «Operative techniques and instrumentation for neurosurgery,» *Neurosurgery*, vol. 53, n. 4, pp. 907-934, 2003.
- [21] C. Lu-Ping e C. Kuen-Tzong, «Shape optimal design and force sensitivity evaluation of six-axis force sensor,» *Sensors and actuators*, pp. 105-112, 1997.
- [22] N. Yoganandan, F. A. Frank, A. Pintar, J. Zhang e J. L. Baisden, «Physical properties of the human head: Mass, center of gravity and moment of inertia,» *Journal of Biomechanics*, vol. 42, pp. 1177-1192, 2009.
- [23] M. Blokker, P. Rutten e S. De Hert, «Occupational exposure to sevoflurane during cardiopulmonary bypass,» *Perfusion*, vol. 26, n. 5, pp. 383-389, September 2011.